OIE'25

The Fifteenth Japan-Finland Joint Symposium on Optics in Engineering

UNIVERSITY OF EASTERN FINLAND

January 6 – 9, 2025
Sokos Hotel Levi
Levi, Lapland, Finland

Lappeenranta 1995, Tsukuba 1997, Kajaani 1999, Suita 2001, Saariselkä 2003, Sapporo 2005, Tampere 2007, Tokyo 2009, Turku 2011, Utsunomiya 2013, Joensuu 2015, Sado 2017, Espoo/Tallinn 2019, Hamamatsu 2023, Levi 2025

# OIE'25 PROCEEDINGS

January 6 – 9, 2025, Levi, Finland

Editor:
Jarkko J. Saarinen

Organizer:
University of Eastern Finland
Department of Chemistry and Sustainable Technology
Joensuu, Finland

# ORGANIZERS

### General Chair

Jarkko J. Saarinen (University of Eastern Finland)

### Co-chairs

Jyrki Saarinen (University of Eastern Finland)
Yoshio Hayasaki (Utsunomiya University)

### International Organizing Committee

Tapio Fabritius (University of Oulu)
Pekka Hänninen (University of Turku)
Erkki Ikonen (Aalto University)
Katsuhiro Ishii (GPI)
Yusuke Ogura (Osaka Unversity)
Kai-Erik Peiponen (University of Eastern Finland)
Shin-ichi Satake (Tokyo University of Science)
Takamasa Suzuki (Niigata University)
Shuji Taue (Kochi Institute of Technology)
Haruyoshi Toyoda (Hamamatsu Photonics)
Erik Vartiainen (Lappeenranta University of Technology)

### Organizing Committee

Jarkko J. Saarinen (University of Eastern Finland)
Jyrki Saarinen (University of Eastern Finland)

### Organizer

University of Eastern Finland (https://www.uef.fi/en)
Department of Chemistry and Sustainable Technology
P.O. Box 111
FI-80101 Joensuu
Finland
https://www.uef.fi/en/unit/department-of-chemistry

# FOREWORD

It is my pleasure to wish you all a warm welcome to Levi, Lapland.

This is the fifteenth event in the symposium series since the inaugural symposium held in Lappeenranta in 1995. The symposium series have continued biannually in Tsukuba (1997), Kajaani (1999), Suita (2001), Saariselkä (2003), Sapporo (2005), Tampere (2007), Tokyo (2009), Turku (2011), Utsunomiya (2013), Joensuu (2015), Sado (2017), Espoo / Tallinn (2019), and Hamamatsu (2023).

The symposium series brings together researchers and specialists from industry, research institutes, and academia to discuss recent advances in various aspects of optics and photonics in engineering. The series of symposia have strengthened the connections between our two countries in field of optics and photonics.

Welcome to Levi, Lapland. I hope you will also have a chance to visit the surroundings of the Levi resort and experience the Lapland in winter. I hope your visit to the OIE’25 symposium is rewarding and enjoyable.

Jarkko J Saarinen
OIE’25 General Chair

# CONTENTS

### *Session 4: Optical Measurements*

**Wednesday Jan 8, 2025**

8:30-8:50 Aleksandr Danilenko: Application of a bandwidth correction method to thin-film reflectance measurements
8:50-9:10 Koyo Watanabe: Precision measurement of chromatic dispersion using a femtosecond-resolution pulse shaper and autocorrelator
9:10-9:30 Yusuke Ogura: Spatial photonic Ising machine using a digital micromirror device
9:30-9:50 Takamasa Suzuki: Down-sampling vibration-measurement technique based on a laser diode interferometry
9:50-10:10 Ryohei Hanayama: Development of body surface vibration meter using speckle shearing interferometer

### *Session 5: Photonics fundamentals*

**Wednesday Jan 8, 2025**

10:40-11:00 Takeshi Yasui: Photonic 6G wireless communication
11:00-11:20 Ari T. Friberg: Self-evolving vector Bessel beams
11:20-11:40 Kuroo Nami: Parameter exploration in the framework of volumetric beam shaping
11:40-12:00 Kazuki Yamanouchi: Three-dimensional imaging through scattering media by constructing a digital twin based on Gaussian Splatting
12:00-12:20 Yoshio Hayasaki: Spatial and temporal stabilization in holographic beam shaping for industrial use

### *Sesion 6: Photonics Applications*

**Wednesday Jan 8, 2025**

13:40-14:00 Yukitoshi Otani: Seasonal sunlight interaction using angularly selective microstructured surfaces
14:00-14:20 Kenji Harada: Phenomenon of coloration of bubbles under thin ice observed in Lake Kusshаro during severe winter
14:20-14:40 Shuji Taue: AC Magnetic field imaging with optically pumped magnetometer and digital micromirror device
14:40-15:00 Closing of the OIE'25 symposium

### *Poster presentations*

Ilpo Niskanen: Complex refractive index shift from liquid to solid in the drying process
Kai-Erik Peiponen: Ultra-high-definition imaging in the detection of microplastics in water flow
Soma Tobinaga: Computational considerations of adaptive single-pixel imaging for magnetic particle imaging with optically pumped magnetomet

## *Session 1: Biophotonics and applications*

## Tuesday Jan 7, 2025

8:30-8:50 Esa Hannila: Simulation-assisted designing process of optical disinfectant system for food safety

8:50-9:10 Matti Huotari: The PPG and ECG comparison at difference body postures according to the Poincaré plots and variance inflation factor

9:10-9:30 Hirofumi Kadono: Advanced biospeckle based microbioassay for rapid detection of water toxicity using bacteria

9:30-9:50 Hirofumi Kadono: Biospekle optical coherence tomography (bOCT) reveals the size and dose-dependent impact of micro and nano copper oxide particles on lentil seed's internal activity

9:50-10:10 Uma Rajagopalan: Laser biospeckles as a speedy tool to investigate the effects of environment in plant science

# Simulation-assisted Designing Process of Optical Disinfectant System for Food Safety

Esa Hannila[1], Jouni Karhu[2], Anna-Liisa Välimaa[2], Sanna Hietala[2], Harri Määttä[3] and Tapio Fabritius[1]

[1] *Optoelectronics and Measurement Techniques Research Unit, University of Oulu, Oulu*
[2] *Natural Resources, Natural Resources Institute Finland, Oulu*
[3] *Centre for Research and Innovation, Oulu University of Applied Science, Oulu*

*Corresponding author: esa.hannila@oulu.fi*

This work is financially supported by the European Regional Development Fund's Printed Intelligence – enabler for safety in food chain (grant no. A76695). A special thanks goes to all participants of the project who provided special expertise, materials, and manufacturing services.

**Keywords:** food safety, photocatalytic disinfection, printed intelligence, simulation, violet-blue light

Efficient and well-functioning food chain is one of the fundamental elements and basic pillars of any human society [1]. It is a diverse ecosystem influencing all and requires process development, emphasizing the importance of the research in the field [2]. Food is very difficult to make perfectly safe and some contaminants are always present. Unhealthy, even dangerous contaminants in food can include material residuals (soil, metal particles or microplastic), pathogens and other micro-organisms (bacteria, viruses, fungi, algal toxins etc.). Toxic material residuals in foods (lead, mercury, arsenic, microplastics, etc.) usually originate from processing and packaging. Industrial processes can also release chemicals, which contaminate the food. [1, 2] Pathogens such as microbes and Algal toxins are also a potential cause for a variety of food-borne acute diseases or chronic sequelae [2, 3]. International and national agencies/governmental officials are tasked to monitor and regulate the food supply chain to ensure food safety and acceptable level of contaminants. [1, 2] In addition to monitoring and testing, methodologies and technologies to maintain acceptable contamination levels in the food chain need to be developed.

Varying methods exist for retaining food safety. One of the simplest techniques is a liquid-based wash to remove food debris and thus, decelerate bacteria proliferation and biofilm growth. [4, 5] Not only does it waste extensive amounts of water resources, but using chemicals can be problematic due to their toxicity. [5, 6] One potential technique to replace liquid wash is the exploitation of violet-blue and ultraviolet (UV) light due to its antimicrobial properties [7, 8]. 405 nm violet-blue light is exceptionally promising. It is safe to use at recommended irradiation levels but still effective against bacteria, fungi, yeast, and spores. [7] In this study optical measurements systems and COMSOL Multiphysics simulation software are used to predict and analyze performance of a LED glass laminate lighting element for disinfection purposes on different surfaces. The disinfection system model is verified by the measurements, and it can be used to evaluate the effect of different design variants of the device without material and fabrication expenses.

The two-phased analysis includes computational modelling and experimental testing. For testing purposes, an LED lighting element was fabricated (Fig. 1a). The element consists of an LED-foil including LED components and printed silver wiring, laminated inside standardized safety glass. The irradiance of LED lighting element is optically measured with spectrometer to assess its performance as a disinfection system. The results can also be used to verify the simulation model in COMSOL Multiphysics. Simulation model consists of the same elements as the physical sample. The material parameters and geometry-related information are obtained from COMSOL material libraries or from the datasheets and existing research. Simulation utilizes Ray Tracing to evaluate irradiance and optically induced disinfection performance.

Irradiance was measured with the Avantes AvaSpec-ULS2048CL-EVO spectrometer and Bentham Instruments D7 Cosine Corrected Transmission Diffuser. The measurements were repeated at three different distances from 10, 20 and 50 cm. COMSOL Multisphysics was used to simulate digital models in similar environment at the same distances. The number of rays were set to 400 for each point-like light source to reduce the simulation memory demand. Still, 400 rays were producing reasonable and realistic-looking power distribution results (Fig. 1b). Irradiance values peaked at 405 nm, but simulated values were a bit higher than measured. Both measurements and simulation results are presented in Fig. 1c and in Table 1.

The measurement and simulation results for the LED lighting element in different setup configurations are well aligned proving the relevance of the model. Simulation models can be used to evaluate similar lighting elements in a very fast and cost-effective manner and still have reasonably accurate results, thus accelerating technology development. In this setup, measured and simulated irradiance for the lighting element was

observed to be about 152 µW/cm$^2$ and 176 µW/cm$^2$ at the closest distance of 10 cm. This is a bit problematic since it was estimated to take over 6 days of radiation at 10 cm to achieve a one log reduction of Staphylococcus bacteria. [9] It is worth mentioning that photocatalytic coatings could improve the disinfectant efficiency [10, 11]. Small differences between the simulated and measured results can be an outcome of multiple sources such as: 1) LED characteristics in the datasheet are given in graph form and minor inaccuracies are inevitable data is transformed into table form. 2) Minor inaccuracies in components geometry and material parameters due to model simplification and material doping. 3) Evaluation method differs a bit as spectrometer has a light sensitive element (photomultiplier tube, CCD camera, etc.) and simulations integrates the irradiance over the sample surface. 4) The heating of LED is known to reduce its efficiency [12, 13] and thermodynamics was excluded from the current version of the simulation.

As a conclusion, the results did suggest the glass laminate lighting unit being a feasible concept. The current lighting element was not efficient enough and requires optimization. Still, the resulting irradiance had the right response spectrum, and in principle, it could be used for disinfectant purposes. The comparison between the measured and simulated results indicated simulations being reasonably accurate. This is a remarkable observation on the device and structural optimization point of view. A designer can quickly redesign the structure and estimate the irradiance output by simulating without producing direct waste material. After reaching desired energy levels, one can move on to the fabrication of physical devices.

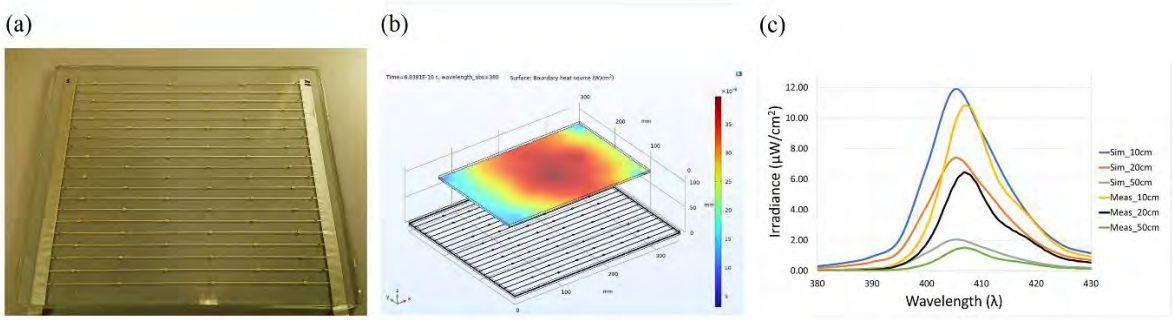


Fig. 1. Photos of a) LED glass laminate b) simulation model c) Measured vs. simulated irradiance spectrum.

Table 1. Measured vs. Simulated total irradiance

| **Total Irradiance (µW/cm$^2$)** | **@10cm** | **@20cm** | **@50cm** |
|---|---|---|---|
| Measured | 152 | 88.6 | 21 |
| Simulated | 176 | 109 | 30.5 |

**References**


1. F. Fung, H. Wang and S. Menon, *Biomedical Journal* **41**, 88-95 (2018).
2. A. Borchers, S. Teuber, C. Keen and M. Gershwin, *Clinical Reviews in Allergy & Immunology* **39**, 95–141 (2009).
3. T. Awad, D. Asker and B. Hatton, *ACS Applied Materials & Interfaces* **10**, 22902-22912 (2018).
4. S. Sokunrotanak, K. Iqbal and H. Sang-Do, *Food Control* **31**, 572-585 (2013).
5. M. Vigil, M. Pedrosa Laza, H. Moran-Palacios and J. Alvarez Cabal, *Sustainability* **12**, 3674 (2020).
6. M. Eide, J. Homleid and B. Mattsson, *LWT - Food Science and Technology* **36**, 303-314 (2003).
7. M. Maclean, K. McKenzie, J. Anderson, G. Gettinby and S. MacGregor, *Journal of Hospital Infection* **88**, 1-11 (2014).
8. H. Singh, S. Bhardwaj, M. Khatri, K.-H. Kim and N. Bhardwaj, *Chemical Engineering Journal* **417**, 128084 (2021).
9. M. Hessling, B. Spellerberg and K. Hoenes, *FEMS Microbiology Letters* **364**, 2 (2016).
10. V. Yemmireddy and Y. Hung, *Comprehensive Reviews in Food Science and Food Safety* **16**, 617-631 (2017).
11. S. Deshmukh, S. Patil, S. Mullani and S. Delekar, *Materials Science and Engineering C* **97**, 954-965 (2019).
12. E. Hannila, N. Heinilehto, K. Remes, J. Lauri, K. Keränen and T. Fabritius, *IEEE Transactions on Instrumentation and Measurement* **70**, 1-10 (2021).
13. E. Hannila, N. Heinilehto, J. Lauri, K. Keränen and T. Fabritius, *IEEE International Instrumentation and Measurement Technology Conference (I2MTC)* **Dubrovnik**, 1-6 (2020).

# The PPG and ECG comparison at difference body postures according to the Poincaré plots and variance inflation factor

Matti Huotari[1]

[1] *BISG, University of OULU, FINLAND*

*Corresponding author: matti.huotari7@gmail.com*

**Keywords:** PPG, ECG, HRV, Poincaré plots, variance inflation factor, supine, sitting, standing

Both Photoplethysmography (PPG) and electrocardiography (ECG) can be applied to determine heart rate variability (HRV) and pulse rate variability (PRV), which are noninvasive techniques for monitoring changes in the inter beat intervals (IBI) and in the inter pulse intervals (IPI or IBI). The biophotonic techniques especially wearables have received much attention and research setups. They have been applied for assessing the autonomic activity. These measurement method highly correlated in healthy young subjects, however, the differences in HRV and PRV have been observed between elderly subjects under various physiological conditions, i.e., supine, sitting, and standing postures. The reasons for the great differences in assessing the degree of IPI vs. IBI has remained unknown until nowadays. That's why we evaluated the impact of supine, sitting, and standing postures on the young and elderly PRV and HRV, respectively.

In the physiological measurements we used a labmade electrophysiological amplifier to amplify the ECG, a labmade photoplethysmographic device for the PPG and a 16 bit National Instruments card to collect the ECG and PPG simultaneously sampled at a rate of 1 kHz to ensure a high enough resolution. To acquire the ECG signal, three electrodes were attached to the participant, using standard lead II connection. The PPGs were collected from the right forefinger. To the left forefinger the Coresense sensor was attached with mobile data collection. In calculations of beat and pulse intervals we applied local maxima rule in the second derivative A pulse of PPG, but we applied window search in the OriginLab software to find the IBI in the ECG. All the found A pulses and R signals were visually checked that there was no missing wave or false found.

The Poincaré plot analysis result suggests, that supine posture has a higher SD1 and SD2 values in the Poincaré plane, i.e., higher sympathetic influence and hence supine has a better resting condition than sitting and standing in the cases, which accurately were shown by Poincaré plane. In addition, we determined the variance inflation factor (VIF) which show suitability as a correlation indicator. Because body posture significantly influences heart rate variability (HRV) through the autonomic nervous system (ANS), it is indicated in the Poincaré plot analysis. The HRV analysis is non-invasive, easily done, and can also accurately separate between sympathetic and parasympathetic function, and has become a popular means of everybody´s assessing tool how the ANS controls heart rate. HRV determination is based on an electrocardiogram (ECG), and pulse rate variability on a photoplethysmogram (PPG). Both HRV and PRV analysis could be used to monitor variations in HRV and in PRV over time and provide vital information on ANS function. Here we calculate PRV both PPG and mobile Elite HRV means. In these case, HRV are derived from the analysis of the IBI dynamics of the intervals between R waves in the ECG signal, known as the RR, and PRV that of IBI dynamics of the intervals between A waves in the second derivative of the PPG time series, known as the PP, respectively. HRV analysis is a technique for measuring HRV over 5 min during each posture state. From the result, it can be concluded that in all three postures, inter beat intervals (IBIs) become smaller from supine posture followed by sitting and at last standing. Supine is a more relaxed condition than sitting or standing. Also PPG signal has been introduced as an alternative for ECG and is used in some applications such as modern biophotonic wrist-worn heart rate monitors.

IBIs obtained from ECG and maximum of PPG and its second derivative for subject. The PPG and ECG signals are illustrated as an example, Fig. 1(a) shows a schematic picture ECG for 30 s and Figure 1(b) second derivative of PPG. Fig. 2(a) shows a schematic picture correlation of IBI of PPG in supine, (b) sitting, (c) standing, and (d) Poincaré plot supine, (e) sitting, and (f) standing.

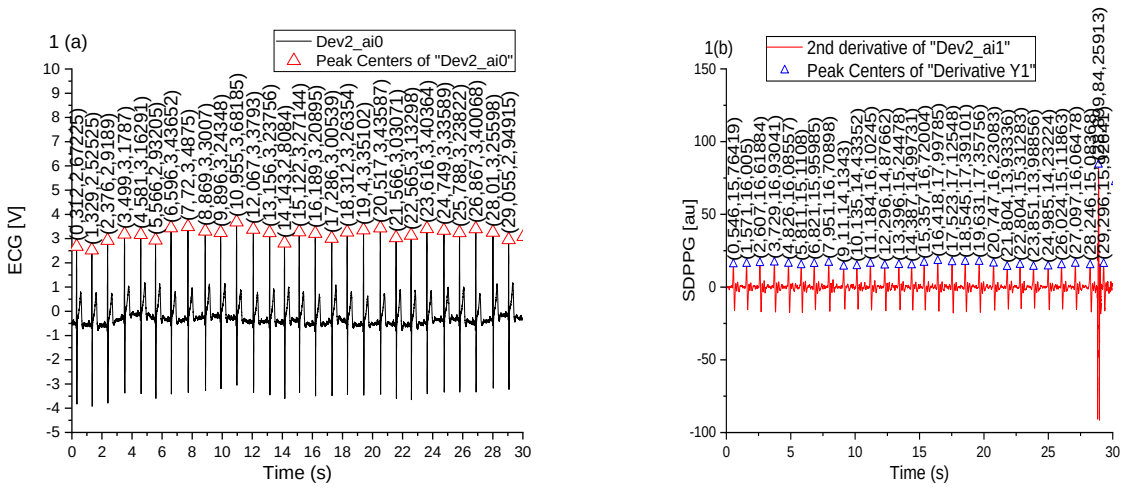


Fig. 1. The 30s ECG (a) and the corresponding second derivative PPG (b).

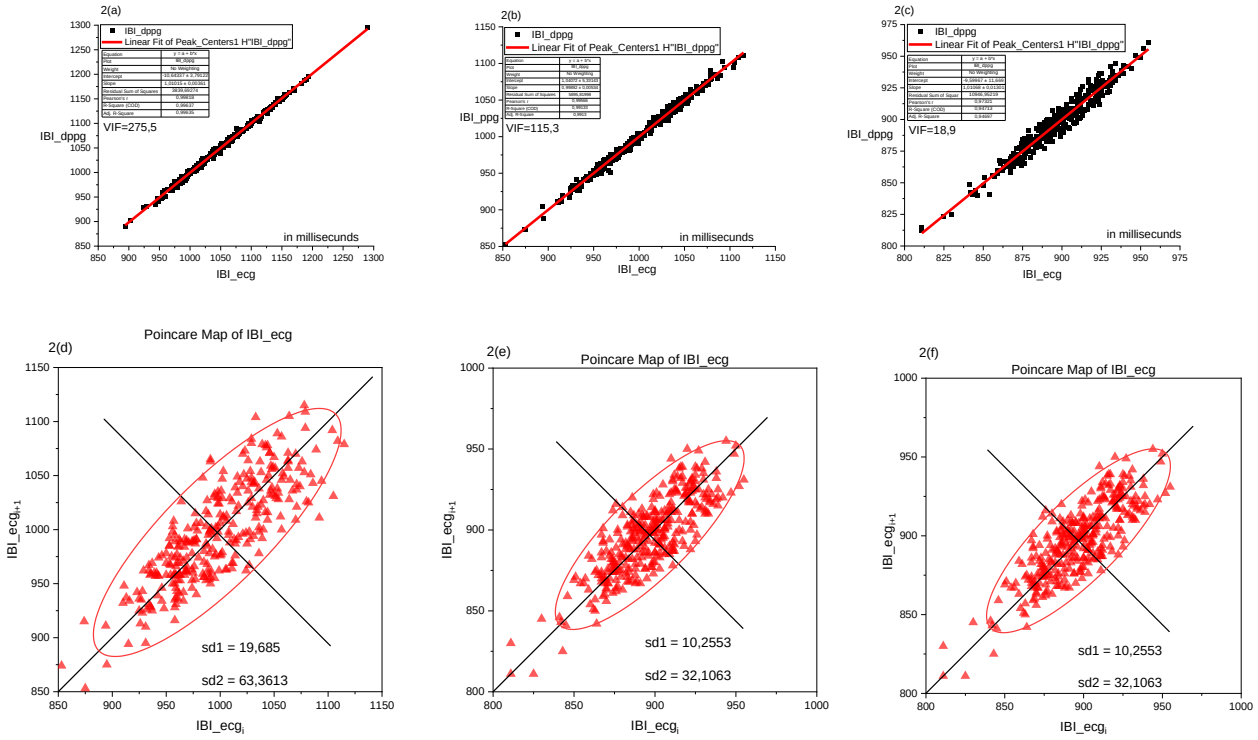


Fig. 2(a) shows IBI of PPG vs ECG in supine, (b) sitting, (c) standing shown with the VIF values, and (d) Poincaré plot of supine, (e) sitting, and (f) standing posture shown with the SD1 and SD2 values, respectively.

The important parts of the coming works would be evaluation of elderly persons and some other ways to define the health condition for correlation purposes in the PPG signal and also to evaluate different PPG measurement locations, i.e., forehead for analysis of correlations between HRV and PRV parameters with young and elderly as well as vascular patients.

**References**


1. Burma, J.S.; Griffiths, J.K.; Lapointe, A.P.; Oni, I.K.; Soroush, A.; Carere, J.; Smirl, J.D.; Dunn, J.F. Heart Rate Variability and Pulse Rate Variability: Do Anatomical Location and Sampling Rate Matter? Sensors 2024, 24, 2048.
2. Jan, HY., Chen, MF., Fu, TC. et al. Evaluation of Coherence Between ECG and PPG Derived Parameters on Heart Rate Variability and Respiration in Healthy Volunteers With/Without Controlled Breathing. J. Med. Biol. Eng. 39, 783–795 (2019).

# Advanced biospeckle based microbioassay for rapid detection of water toxicity using bacteria

Devi Arti[1], Hirofumi Kadono[1]*, R. Uma Maheswari[2]

[1] *Graduate School of Science and Engineering, Saitama University, Saitama*
[2] *Dept. Mech, Eng. Faculty of Engineering. Shibaura Institute of Technology, Tokyo*

*Corresponding author: *kadono@mail.saitama-u.ac.jp*

**Keywords:** laser biospeckle, bioassay, water toxicity, bacteria, Copper, environmental toxicity

Recently, the environmental pollution caused by various hazardous chemicals has become a very serious problem. Traditional toxicity assessment of the polluted water has been done by identifying and analyzing each chemical individually. Nowadays, there are more than 200 million kinds of chemical substances registered. Therefore, it is technically very difficult and costly to analyze and identify each chemical individually, and then evaluate its environmental toxicity. On the other hand, a direct toxicity assessment (DTA) or a bioassay offer a comprehensive alternative by evaluating the overall toxicity without identifying specific chemicals. Bioassays measure how organisms respond to pollutants compared to controls. In microbioassays, where microorganisms are used, the toxicity is gauged by key factors such as whether organisms are alive/dead and their swimming ability. However, one potential limitation of the bioassay is the requirement of microscopic observation and hence the limited focal depth of the imaging system. This leads to the difficulties in simultaneous monitoring of many organisms as a decrease in the size of the microorganisms. To overcome this, we developed a novel microbioassay technique based on a dynamic biospeckle generated from the biological activities of organisms, such as movement and cell morphological change [1]. This activity is quantitatively evaluated using the crosscorrelation function between an initial reference frame and subsequent frames of the biospeckle pattern. The method's reliability has been demonstrated using planktons, *Paramecium* and *Euglena,* under different heavy metal toxicants such as Zn, Fe, and Cd [2-4]. We further applied this method to bacteria exposed to varying concentrations of Copper (Cu) that is an emerging pollutant. Industrial activities, domestic wastewater, mining wastewater, and weathering of copper-bearing rocks are the major sources of copper in surface and ground waters.

The experimental setup to record the biospeckle is shown in Fig. 1. The system consists of a laser diode of wavelength, 638nm. The laser light was collimated by lens L1 with a focal length of 30 mm. The sample cell with a gap of 1 mm was illuminated vertically from the bottom with the light reflected by mirror M1. The illuminated area or probe area on the sample cell was 15 mm in diameter. The light transmitted through the sample cell was focused by a lens L2 of focal length 250 mm. A spatial filter was placed at the Fourier transform plane of the sample to filter out the specular components of transmitted light. The dynamic biospeckles reflecting the internal activities and external morphological changes of the cells under different Cu concentrations were captured by a CCD camera at 60 frames per second (fps) for 2 min. The recorded movies were analyzed to evaluate the variation rate in the biospeckle.

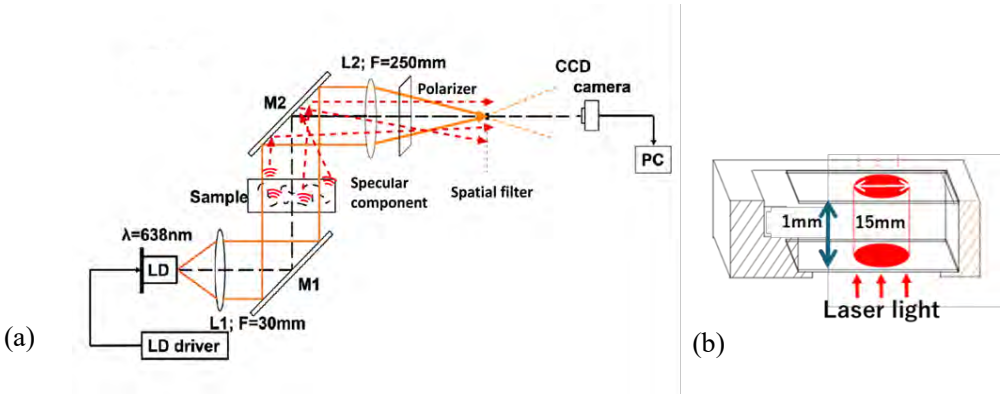


Fig. 1(a) Schematic diagram of experimental system. M1~M2: mirrors, L1~L2: lenses. Sample cell (cell gap: 1mm) containing *bacteria* is illuminated by the parallel beam, (b) Sample cell used for this study.

A crosscorrelation method was applied, where the crosscorrelation coefficient $\rho(t_i)$ was calculated between the first frame ($t=t_0$) being fixed as a reference and the frame at $t=t_i$ as given by,

$$\rho(t_i) = \frac{\sum_{x,y}\{I(t_i;x,y)-\langle I(x,y)\rangle\}\{I(t_0;x,y)-\langle I(x,y)\rangle\}}{\sqrt{\sum_{x,y}\{I(t_i;x,y)-\langle I(x,y)\rangle\}^2 \sum_{x,y}\{I(t_0;x,y)-\langle I(x,y)\rangle\}^2}}, \quad (1)$$

where $I(t_i; x, y)$ is the intensity at coordinate $(x, y)$ at time $t_i$, and $\langle I(x, y)\rangle$ denotes the time average of the intensity over the observation period. Next, a correlation time, $\tau_c$, is derived that can be used to measure the biological activities of the bacteria as longer correlation time would indicate slower movement or change while smaller correlation times would indicate swifter change. The correlation time $\tau_c$ was defined as the time when the crosscorrelation coefficient falls to $\frac{1}{e}$.

The bacteria were exposed to varying concentrations of Cu for 1.5 hours. The permissible level (PL) for Cu is 1mg/L in drinking water decided by the WHO. Figures 2(a) and (b) illustrate the variation of the crosscorrelation function's over time, and the correlation time for the different concentrations of Cu, respectively. It can be seen that, the width of the crosscorrelation function or correlation times at 0.05×PL, 0.5×PL, and 1×PL (0.05, 0.5, 1mg/L) were observed significantly longer than that of the control suggesting the reduction in both internal movement and morphological change of the cells. This is likely due to Cu inhibiting bacterial activity by damaging bacterial cell membranes, generating reactive oxygen species (ROS), and disrupting essential proteins and enzymes within the cell. Both figures demonstrate that the correlation times were significantly longer compared to the control, indicating reduced bacterial activities under Cu exposure. Specifically, the correlation times increased by factors of 1.7, 2.5, and 2.4 at Cu concentrations of 0.05, 0.5, and 1 mg/L, respectively. It should be noted here that the significant variations in the correlation time could be observed in the concentration range much smaller than PL, i.e., the proposed method is very sensitive for the pollutant, Cu.

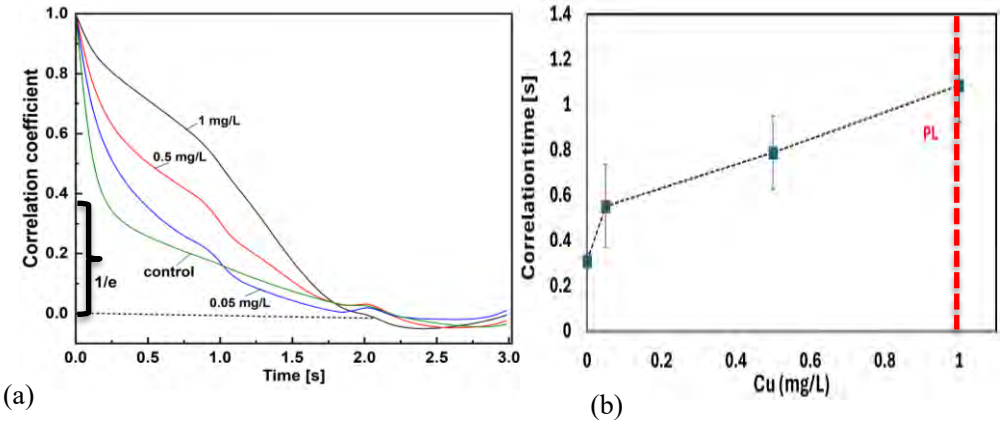


(a) (b)

Fig. 2(a) Correlation coefficient as a function of time for bacteria for 1.5 hoursn exposure, (b) Correlation time as a function of Cu concentrations.

The variation in biological activites of bacteria/organisms is strongly related to environmental toxicity, and it was confirmed that their biological activities could be quantitatively evaluated by converting the image of bacteria into a speckle image with a further analysis using the crosscorrelation. Unlike conventional microbioassay, the advantage of our method is that the method does not require the observation with microscope to obtain the microorganism's condition such as alive or dead status. Since large number of organisms can be evaluated as an aggregate, this method is more reliable and efficient than the conventional method where one must individually evaluate the alive or dead status of the microorganism using microscope. Since an image of any randomly distributed object can be converted into a speckle pattern, the same evaluation method can be applied to any organism such as fungi, and somatic cells.

## References


1. J. W. Goodman, "Statistical properties of laser sparkle patterns," *(No Title),* 1963.
2. A. Devi, H. Kadono, and U. M. Rajagopalan, "Laser biospeckle method for a fast and reliable microbioassay," *Appl. Opt.,* vol. 63, no. 21, pp. 5721-5727, 2024/07/20 2024, doi: 10.1364/AO.528227.
3. A. Devi, H. Kadono, and U. M. Rajagopalan, "Fast and reliable micro bioassay techniques based on biospeckle for swift water assessment using plankton," in *Biophotonics in Point-of-Care III*, 2024, vol. 13008: SPIE, pp. 11-18.
4. A. Devi, H. Kadono, and U. M. Rajagopalan, "Fast Assessment of Quality of Water Containing Inorganic Pollutants Using Laser Biospeckles in Microbioassay," *Applied Sciences,* vol. 14, no. 13, p. 5558, 2024.

# Biospekle optical coherence tomography (bOCT) reveals the size and dose-dependent impact of micro and nano copper oxide particles on lentil seed's internal activity

Lavista Tyagi[1], Hirofumi Kadono[1*], Uma Maheswari Rajagopalan[2]

[1]*Graduate School of Science and Engineering, Saitama University, 255 Shimo-Okubo, Sakura-Ku, Saitama- Shi, Saitama, 338-8570*

[2]*Shibaura Institute of Technology, 3-7-5 Tyosu, Koto City, Tokyo 135-8548, Japan*

*Corresponding author:* kadono@mail.saitama-u.ac.jp

**Keywords:** Biospeckle, Optical coherence Tomography, Nanoparticles, Copper oxide, Lentil, Toxicity, Environment

Nanoparticles (NPs) have become increasingly prominent as new contaminants of concern due to their broad applicability in several fields, including agriculture, industry, and medicine. The potential impacts of NPs on seed germination and plant development remain largely unexplored, demanding the development of advanced analytical techniques to elucidate plant responses to NPs exposure. Considering that NPs have the ability to penetrate seed structures and perhaps interfere with cellular processes, comprehensive studies are required to understand how NPs affect plant growth and seed germination.

We have developed Biospeckle optical coherence tomography (bOCT), for visualizing the internal activities of plants with the advantages of real-time, non-invasive, and high sensitivity, and the current study proposes the application of bOCT to investigate the size and dose-dependent effects of copper oxide (CuO) nano and microparticles on the internal activity of lentil seeds. Lentil is a major food crop in Asia, valued for its significant nutritional benefits, having high protein, flavonoids, fiber, and essential minerals like iron and magnesium. Understanding the impacts of CuO NPs are crucial, as their extensive use in agriculture, electronics, energy storage, and biomedical industries poses risks to the plant health and ecosystem stability. Our previous research effectively demonstrated the capability of bOCT to assess the size-dependent effects of $TiO_2$ and ZnO NPs on lentil seeds revealing significant positive impacts of 21 nm and <5 µm $TiO_2$ particles at concentrations of 25 and 100 mg/L, while ZnO NPs <50 nm exhibited negative effects compared to those <5 µm at both concentrations [1,2].

The bOCT experimental system is illustrated in Fig.1(a) utilizing the swept source of bandwidth 130nm with a central wavelength of 1.3 µm. The axial resolution was 6 µm, and the lateral resolution was 39µm. A total of hundred frames of 3048 (x) × 1000 (z) pixels of lentil seeds were acquired at an acquisition rate of 12.5 frames per second over an 8 sec. At each pixel of the bOCT structural images along the temporal axis, intensity fluctuation can be seen originating from the biological activities of the cells while a conventional OCT gives only anatomical images. When coherent light, such as laser light, is illuminated on a plant, the light is scattered by rough scattering structures inside the plant. Such scattered light interferes randomly to form a granular speckle pattern known as biospeckle [3]. A degree of fluctuation is characterized by a quantity, biospeckle contrast, $\gamma$ which is defined by the ratio of the standard deviation of the intensity to the mean value at each pixel along the temporal axis over the total scan was calculated according to the following equation,

$$\gamma\,(x,y) = \frac{1}{<I_{OCT}(x,y)>}\left[\frac{1}{N}\sum_{j=1}^{N}\{I_{OCT}(x,y,t_j) - < I_{OCT}(x,y) >\}^2\right]^{\frac{1}{2}}, \quad (1)$$

where,

$$< I_{OCT}(x,y) \geq = \frac{1}{N}\sum_{j=1}^{N} I_{OCT}(x,y,t_j)\,,$$

and $x$ and $y$ represent the pixel coordinates, $j$ is the scan number, $t_j$ is the time corresponding to each scan, and $N$ indicates the total number of scans [2].

In the experiment, the lentil seeds were exposed to CuO NPs of two distinct sizes (<50 nm and <10 µm) at concentrations of 25 and 100 mg/L. bOCT measurements were conducted at 0, 5, 10, and 30 hours

post-exposure. The average speckle contrasts were calculated over a fixed area under the surface and normalized with the initial values, as illustrated in Figs.1(b) and (c). Figure 1(b) shows a significant decrease of approximately 10.2% in $\gamma$, indicating reduced internal activity of lentil seeds after 10 hours of exposure to smaller CuO NPs (<50 nm) at 100 mg/L. In contrast, larger particles (<10 µm) exhibited no significant changes in seed internal activity compared to that of the control. Figure 1(c) reveals a different trend for larger particles (<10 µm), displaying a significant positive impact after 30 hours of exposure, evidenced by a 10.3% increase in $\gamma$. In contrast, CuO NPs at the lower concentration of 25 mg/L did not induce significant changes in lentil seed internal activity. These results suggest that smaller CuO NPs exert a negative effect on lentil seed's internal activity at 100 mg/L concentration, while CuO microparticles (<10 µm) show a significant positive impact on internal activity at 25 mg/L concentration.

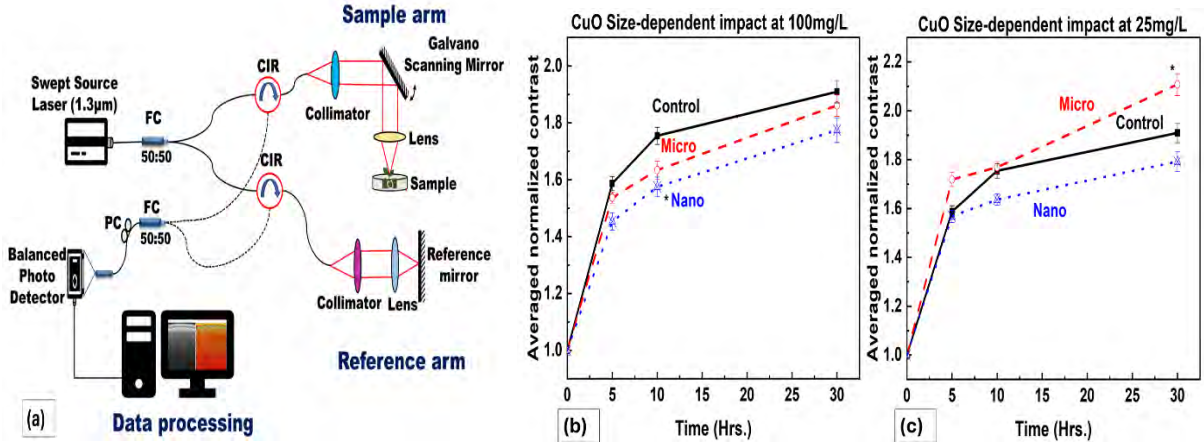


Fig. 1 (a) Schematic of bOCT experimental system, (b) Averaged normalized contrast of bOCT image under CuO NPs exposure at 100mg/L, (c) Averaged normalized contrast of bOCT image under CuO NPs exposure at 25 mg/L. Asterisk (*) represents statistical significance.

The experimental results revealed that CuO NPs at 100 mg/L concentrations exhibit a significant adverse effect just after 10 hours of exposure on the internal activity of lentil seeds. This is because, like leaves have stomata for gas exchange, seed coats have micropyles (pores) that enable water uptake and gas exchange during germination. In lentil seeds, these pores are approximately 4µm in size, allowing smaller CuO NPs to penetrate and potentially interact with cellular structures, interact with cell membranes, release $Cu^{2+}$ ions, and generate reactive oxygen species, thereby disrupting cellular processes. In contrast, larger CuO particles <10 µm showed no significant changes in the internal activity at 100 mg/L but exhibited a significant positive effect at a lower concentration of 25 mg/L on the internal activity of lentil seeds within just 30 hours of exposure. The larger particles, unable to penetrate the seed pores, may serve as a beneficial micronutrient source without causing cellular damage, as Cu is known to be a micronutrient at lower concentrations. Interestingly, these findings align with our previous study on leaf foliar exposure to CuO nano and microparticles at 100 mg/L [4]. When exposed to CuO NPs, leaves showed a rapid and significant decrease in internal activity, with $\gamma$ decreasing by approximately 45% compared to the control within 24 hours. In contrast, microparticle-exposed leaves showed no significant change. This comparison suggests that leaves have a more pronounced sensitivity to foliar exposure to CuO NPs than seeds. The impact on leaves was more pronounced because of their larger surface area and higher metabolic activity, allowing for greater absorption and interaction with the NPs. The proposed bOCT technique successfully compared the impacts of CuO nano (<50nm) and microparticles (<10 µm) on seeds and leaves both at a very early stage, even before germination individually.

## References


1. Y. Sanath, U.M. Rajagopalan, H. Kadono, D. Li, Chemosphere, Volume 303, Part 2, 2022, 135162
2. L. Tyagi, H. Kadono, U.M. Rajagopalan, SPIE Photonics Europe, Tissue Optics and Photonics III (2024).
3. Goodman, J. W. Statistical Properties of Laser Speckle Patterns. 9–75 (1975) doi:10.1007/978-3-662-43205-1_2.
4. L. Tyagi, H. Kadono, U.M. Rajagopalan, JSAP Annual Meetings Extended Abstracts, The 85th JSAP Autumn Meeting, p. 03-468 (2024).

# Laser Biospeckles as a speedy tool to investigate the effects of Environment in Plant Science

Uma Maheswari Rajagopalan[1], Ayato Suzuki[1], Takeshi Baba[1], Takahiro, Kono[2], Jun Yamada[1], and Hirofumi Kadono[3]

*1 Shibaura Institute of Technology; aa20002@shibaura-it.ac.jp*

*2 Tokyo Metropolitan University; kono-t@tmu.ac.jp*

*3 Saitama University, kadono@mail.saitama-u.ac.jp*

* *Correspondence: UMR, uma@shibaura-it.ac.jp*

**Keywords:** Lasers, Biospeckle, Scattering, Lentil seeds, Environmental effects

**Introduction:** Apart from water, light, carbon dioxide, temperature, and humidity, sound has also been established to play are an essential role in important conditions for plant growth. Sound of a particular frequency appropriate to a plant species at the seed germination stages as well at the grown plants, sound has been proven to affect the behavior. Vincent et al.(1) reported the effect of white noise on the germination of maize seeds using germination factor as the measure which requires till the wait of germination time of seven days. However, speedy evaluation methods remain a challenge. We reported earlier the application of laser biospeckles in the speedy evaluation of the response of plants to sound stimulation under different frequencies (2). Here, we have employed laser speckles to the investigation of lentil seed germination under the exposure of sounds white noise of two different sound pressures. We found that sound had significant impact by delaying the germination as against no sound.

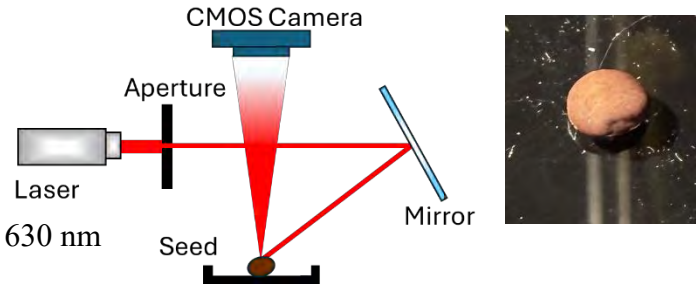


Figure 1 Experimental system with an inset of the seed.

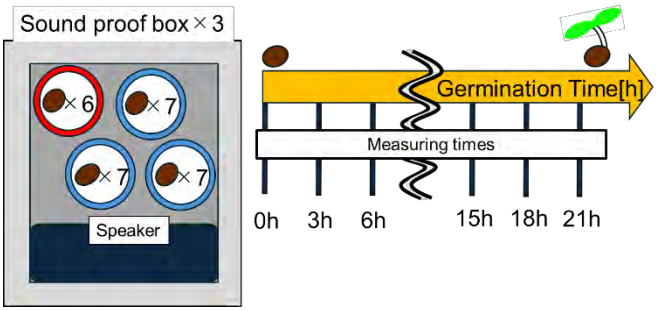


Figure 2 Sound exposure protocol with measurement done at indicated times. Seeds were in soundproof box while being exposed to white noise. Each petri dish consisted of 6 to 7 seeds.

**Experiments:** When a random surface is illuminated by a coherent laser, we get speckles. When the object becomes a living tissue such as a seed, the intensity of the speckles themselves varies according to the internal activity within the seeds. This monitoring the temporal variation of the seed could become a measure of the seed activity. Figure 1 shows the experimental system with an inset of the seed. Seeds illuminated by a collimated beam (1 mm × 3 mm) produce speckles on hte camera plane and were captured by a CMOS camera at 15fps for 10 sec. The acquired speckle videos were analysed by MATLAB. The correlation coefficient (γ) between the first and subsequent frames was calculated and correlation was analyzed by a quantity called Biospeckle activity (1-γ) to evaluate the seed activity.

Figure 2 shows the full protocol with the seeds being placed on a petridish which was then in a sound proof box with each box at condition of no sound, white noise with sound pressure level 80dB and White noise sound pressure level 100dB. Sound was generated from PC by Audacity which was then played from a speaker placed within the box. Sound was played throughout the time except when the seeds were taken out of the box for measurement. A total of 7 seeds were used for measurements under each condition with speckles from a seed acquired for 6 times.

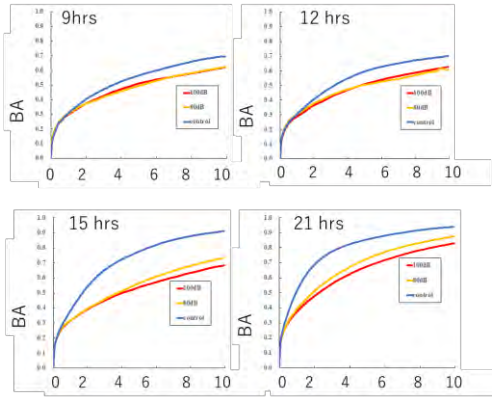


Figure 3. BA given as a function of time for control(blue), and white noise, 80dB(yellow) and 100dB (red).

**Results:** Figure 3 shows the biospeckle contrast as a function of acquisition time in secs under at different hours for different sound pressure levels. As can be seen, the BA largely differs depending on the sound environment. Considering the germination time of lentil seeds which is within a day, a clear difference in the monotonus increase is seen. In order to evaluate quantitatively, the time taken for BA to reach half its value was calulated and the results are given in Fig.4.

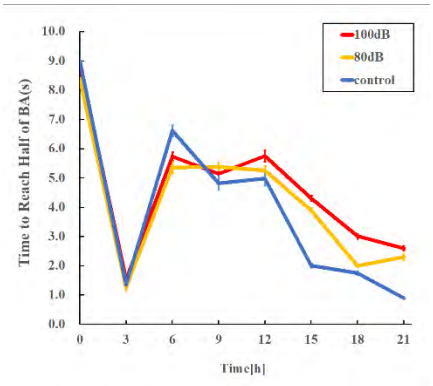


Figure 4. Time taken for BA to reach half its maximum is given as function of the measurement hour for different sounds with control indicated in blue and white noise 80 dB in yellow and 100 dB in red. Error bars indicate standard error.

As can be seen from Fig.4, beyond 9 hours, the effects of sound on germination start to emerge with a clear dependence seen on the sound. While the seeds under control germinate faster, the germination of seeds under white noise is delayed significantly especially under 100 dB. This indicates that sound can play a siginificant role in the speed of germination and that can be evaluated based on biospeckles much earlier in comparison to the coventional methods that involve counting, weight and seedling length measurement and so on.

In the current study, we focused only on white sound at two different sound pressures. Currently, we are conducting measurements at different sound freuqencies of 100 Hz, 1kHz and 10kHz as conducted in our previous study with argula seedling (2). We are also conducting the measurement with a dormant seed to test the effectiveness of the measurement itself. Our earlier study revealed higher frequncies have detrimental effects in comparison to lower frequencies. We believe for seeds too, higher frequencies could have siginificant impact.

**References:**

1. C.M.Vicient , BMC Res Notes, **10(1)**,1–5 2017.

2. U. M.Rajagopalan, R.Wakumoto, D.Endo , M. Hirai , T.Kono , H.Gonome , et al.

PLoS One, **16**(10 October),1–15, 2021.

http://dx.doi.org/10.1371/journal.pone.0258973

## *Session 2: Photonics Materials*

## Tuesday Jan 7, 2025

10:40-11:00 Shin-ichi Satake: Three-dimensional patterning technique for plasmonic nanostructure by dwell-time algorithms with iterative blind deconvolution method

11:00-11:20 Alex Berdin: Printing of holographic elements in reconfigurable thin films with a digital holographic microscope

11:20-11:40 Harri Lipsanen: 2D materials for memristors

11:40-12:00 Junji Yumoto: High-performance 3D-printed functional hollow waveguides for 200–400 GHz band applications

# Three-dimensional patterning technique for plasmonic nanostructure by dwell-time algorithms with iterative blind deconvolution method

Shin-ichi Satake[1], Ryunosuke Komine[1], Noriyuki Unno[1] and Jun Taniguchi[1]

[1] *Department of Applied Electronics, Tokyo University of Science, Tokyo, Japan*

*Corresponding author: satake@te.noda.tus.ac.jp*

**Keywords:** Plasmonic Nanostructure, Electron beam lithography, three-dimensional patterning, dwell time adjustment technique

**Abstract**

Nano- and micropatterned surfaces are attracting considerable research attention because they can be used in various applications such as surface plasmonic sensors. In particular, three-dimensional (3D) surfaces similar to periodic structures on devices have been widely studied. However, strong demand exists for a suitable high-throughput patterning technique that enables the use of such complex 3D surfaces in industrial applications. Nanoimprint lithography (NIL) represents a major breakthrough for this purpose because it is a simple patterning technique. However, the NIL procedure includes a contact process; a 3D master mold is therefore required to produce complex 3D surfaces using NIL. Electron beam lithography (EBL) is widely used to fabricate master molds for NIL applications, but obtaining a smooth 3D mold with a sub-500 nm step pattern directly using conventional EB dose modulation methods is difficult. In this study, we propose a dwell-time algorithm to fabricate a smooth surface using direct 3D patterning based on EBL. As a result, we obtained a target distribution of a 3D pattern with a two-step structure for EBL.

## Introduction

Three-dimensional (3D) surfaces similar to periodic structures on devices have been widely studied. Nano- and micropatterned surfaces can provide various useful functions for optics. For example, surfaces with surface plasmons are attracting considerable attention because they can be used as sensors [1-3]. Such surfaces have complex three-dimensional (3D) structures. For such complex 3D surfaces to be fabricated and used in industrial applications, a high-throughput patterning technique is required. Nanoimprint lithography (NIL) is a major technological breakthrough for this purpose because it enables sub-10-nm patterning with high throughput [4]. Electron beam lithography (EBL) is widely used to fabricate master molds for NIL because it offers sub-10 nm resolution. In the case of 3D step patterning using EBL, the electron beam (EB) dose is typically modulated at a constant acceleration voltage to obtain different heights after development of the surface [5, 6], which is possible because higher EB doses produce deeper patterns when a positive-type EB resist is used. To obtain a smooth 3D pattern, researchers have developed an EBL technique with proximity-effect correction [7] for sub-500 nm patterning. Although conventional patterns have a gentle slope, the 3D step pattern for plasmonic nanostructures typically requires steep 3D hole patterns at the sub-500 nm scale. In the present study, a dwell-time adjustment technique for direct and smooth 3D step patterning via EBL is demonstrated using the iterative blind deconvolution method [8] while considering only forward electron scattering. The dwell-time adjustment technique is typically used in direct machining or milling processes, and the desired 3D pattern is calculated using a unit removal shape [9]. By contrast, EBL processing produces a desired pattern after development; the developed patterns are thus used as a unit removal shape in the present study. Figure 1 depicts the concept of the fabrication process for plasmonic nanostructure via EBL using dwell-time algorithms. First, EB writing is carried out with the dwell-time control calculated by the dwell-time adjustment technique (Fig. 1a). The EB-exposed area is then developed in an EBL developer (Fig. 1b), and a master mold is obtained (Fig. 1c). After a release coating is applied to the master mold, the UV–NIL process is carried out (Fig. 1d–f). As a result, a reverse pattern is fabricated. The reverse pattern is then coated with a thin metal layer via a physical vapor deposition process (Fig. 1g). Finally, nanotransfer printing [10] is carried out to obtain 3D plasmonic nanostructures with metal nanopatterns. As shown

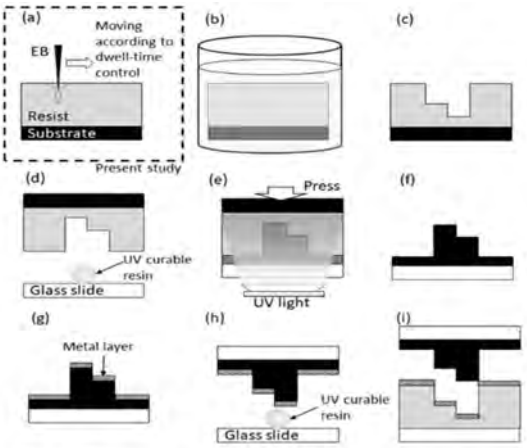


Fig. 1 The concept of the fabrication process

here, the dimensions of the obtained 3D plasmonic nanostructures will be strictly defined by the 3D master mold. Consequently, a precise fabrication technique to obtain a master 3D mold is key for this concept. Therefore, in the present study, the dwell-time adjustment technique using the ideal unit removal shape in EBL is investigated to improve the smoothness of the 3D step pattern obtained via the EB-dose-modulation method.

## 2. Numerical method

### 2.1 Dwell-time adjustment algorithm

A dwell-time adjustment algorithm was originally developed to enable calculation of the quantity of polishing of an optical mirror on the basis of Preston's hypothesis [11]. In a previous study [12], we suggested a dwell-time adjustment algorithm based on the fast Fourier transform (FFT). We applied the algorithm to the focused ion beam (FIB) technique [13] and recently developed an algorithm that overcomes the problem of the negative dwell-time value encountered when using the FFT [8]. In the present study, we apply our latest algorithm to mold manufacturing using an EB on a plasmon surface. The algorithmic details are provided elsewhere [8]; a simple explanation is provided in the next paragraph. The removal by etching using the electron beam is carried out on the basis of the convolution model led by Preston's hypothesis.

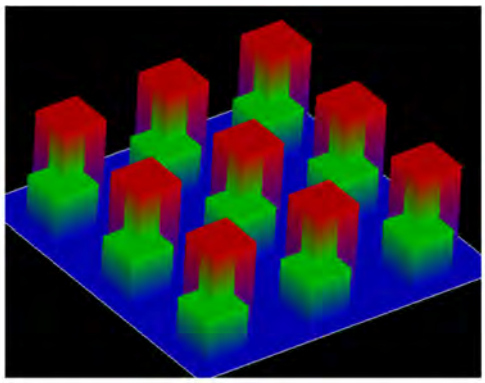

Fig. 2 Target 3D pattern for a plasmonic surface.

### 2.2 Target 3D profile

Two steps are observed in the depth direction of the structure. The calculation domain consists of nine manufactured structures. These nine structures are described in 2048 × 2048 pixels in the calculation domain (Fig. 2).

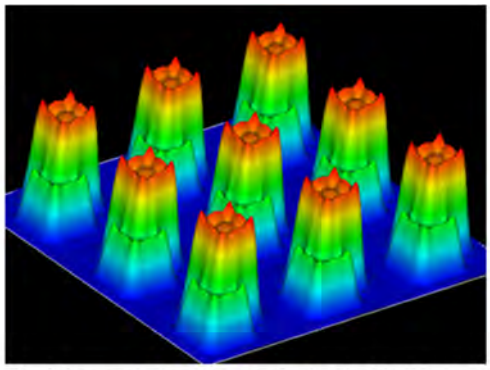

Fig. 3 Removed shape calculated using the Modified AD algorithm.

## 3. Results and discussion

A 3D representation of the target shape corresponding to the Modified AD method is shown in Fig. 3. The top part clearly shows the two steps of the structure, although the distribution is sharp.

## 4. Conclusion

A target distribution for a smooth 3D patterning technique using EBL based on the dwell-time adjustment technique was obtained. In this study, a developed pattern was used as a unit removal shape for the dwell-time adjustment technique, and the shape was considered to be a single Gaussian distribution. We successfully fabricated a mold for direct 3D-patterning EBL using the dwell-time adjustment technique.

**References**


1. Kubo, W., Fujikawa, S., *Nano Letters* **11** (1), 8-15 (2011).
2. Mudachathi, R., Tanaka, T., *Sci. rep.*, 7(1), 1199 (2017).
3. Frank, B., Yin, X., Schäferling, M., Zhao, J., Hein, S. M., Braun, P. V., Giessen, H., *ACS nano*, **7**(7), 6321-6329 (2013).
4. Chou,S. Y., Krauss,P. R., Zhang, W., Guo, L. , Zhuang,L., *J. vac. sci. technol., B, Microelectronics process. phenom* 15.6, 2897-2904 (1997)
5. Hirai, Y., Kikuta, H., Okano, M., Yotsuya, T., Yamamoto, K. *Jpn. J. Appl. Phys.* (39), 6831–6835 (2000)
6. Chen, K.-S., I-Kuan, L. , Fu-Hsang K.:,*J. Micromech. Microeng.* 15.10, 1894 (2005)
7. Grella, L., Di Fabrizio, E., Gentili, M., Baciocchi, M., Maggiora, R.,*Eng.*, 35(1-4), 495-498 (1997).
8.Tanebe, S., Satake, S., *Appl. Opt.* 61, 1743-1749 (2022)
9. Xie, M., Cheng, J., Ma, Z. et al., *Int J Adv Manuf Technol* **130**, 3151–3178 (2024)
10. Unno, N., Taniguchi, J, Microelectron. Eng., 87(5-8), 1019-1023(2010).
11. Aspden, R. McDonough, and F. R. Nitchie, *Appl. Opt.* **11**, 2739-2747 (1972)
12.Satake, S. , Yamamoto, K., Igarashi, S, *Communications in Computational Physics.* **1** (4), 701-715 (2006).
13. Taniguchi, J., Satake,S., Oosumi,T., Fukushige,A., Kogo, Y, *Nucl Instrum Methods Phys Res, Sect B* **307**,248-252 (2013)
14. Ayers, G. R., Dainty, J. C., *Appl. Opt.* **13**, 547–549 (1988).

# Printing of Holographic Elements in Reconfigurable Thin Films with a Digital Holographic Microscope

Alex Berdin[1], Arri Priimägi[1]
[1] *Smart Photonic Materials, Tampere University*
*Corresponding author: alex.berdin@tuni.fi*

**Keywords:** optics, interference holography, azobenzene, nanostructures

In contrast to the advances in miniaturization of electronic components, optical components are often still bulky. Control over material properties such as topography and refractive index is a promising way for miniaturized optics, the fourth-generation optics.[1] We show that surface patterning of photochromic materials using a digital holographic microscope (DHM) with integrated laser interference system shows a "printer"-like fabrication of diffractive optical elements (DOEs).[2] The light-induced mass-migration of azobenzene-containing materials, enables the inscription of topographies in a one-step photolithographic process, which poses a challenge to existing microfabrication methods.[3] This method also enables real-time observation of surface modifications, thus the study, control and metrological analysis of the material and inscribed patterns.

In this contribution, we show how thin films containing azobenzene can be patterned with DHM by superimposing multiple surface relief gratings (SRGs) to create complex topographies.[4] Computer-controlled scanning of the sample position and tuning of interference conditions enable pixelated patterning of large areas with customized surfaces. We show how such light-configurable topographies could benefit applications such as waveguide couplers in near-eye displays. As an example of control, we present optical components with highly controlled diffraction patterns and a true-color hologram generated by a precise superposition of SRGs.

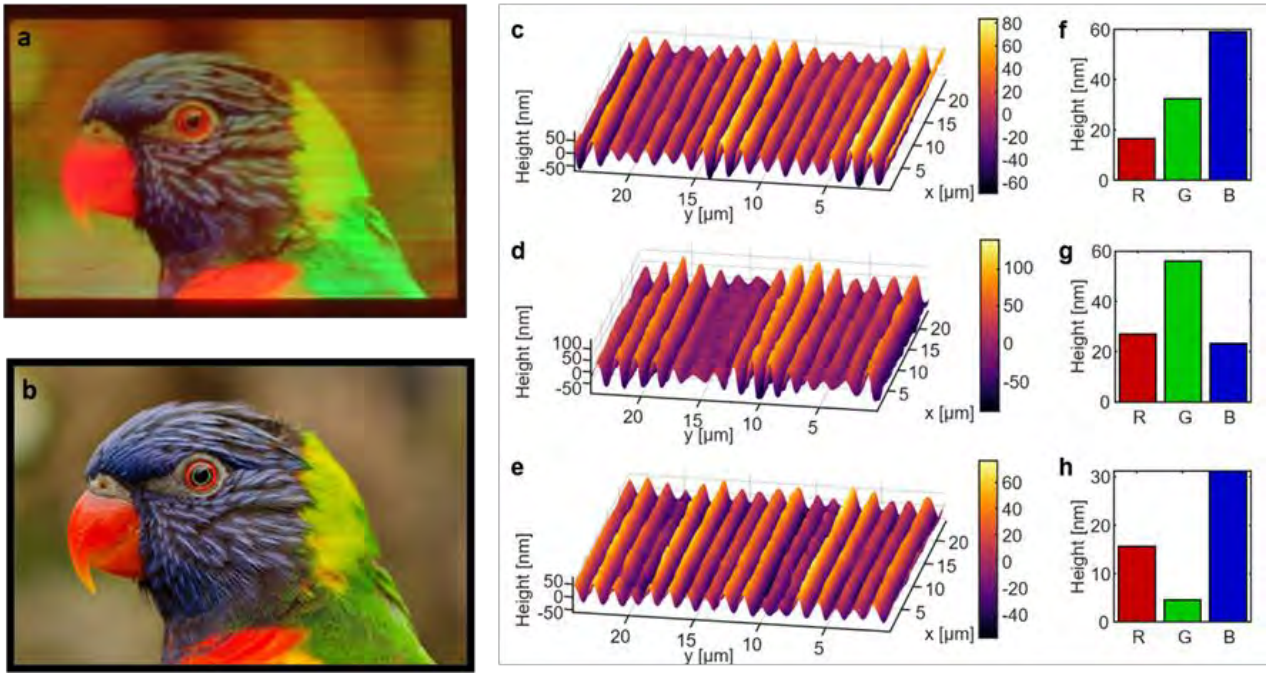


Fig. 1. Full color image writing by stacking gratings. (a) A hologram inscribed into an azobenzene-containing film (b) Source image for patterning. (c–e) Surface profiles of three pixels imaged with the DHM, consisting of a mixture of three grating periods with the measured grating heights shown in (f–g).

Structural colors are common in nature and of great interest for optical applications. In Fig. 1., we show the use of superimposed surface relief gratings to diffract the three primary colors — red, green, and blue — at the same angle for additive color mixing. By controlling the pitch of the inscribed SRG, we vary the angle of the diffracted light, while controlling the amplitude sets the luminance. Scanning the sample on a translation stage and writing in the topographies pixel by pixel according to a reference image results in a printed true-color hologram.

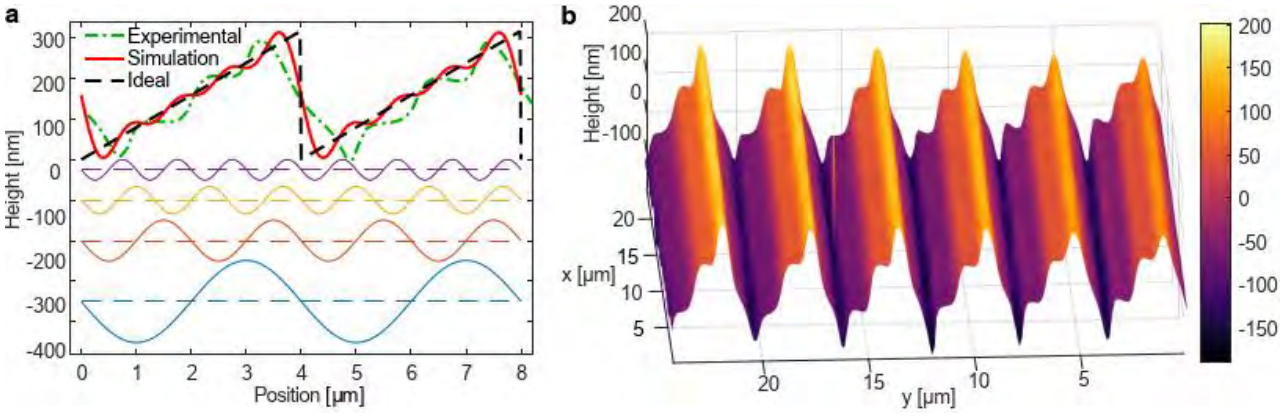


Fig. 2. (a) Simulation of a sawtooth profile composed of 4 components, (b) Realized profile imaged by the DHM.

Fourier analysis has shown that any periodic pattern can be decomposed into sinusoids and their harmonics; conversely, such patterns can be synthesized by superimposing these waves. To inscribe complex patterns on a sample using an interference setup, precise control of the amplitude, phase, and pitch of the SRGs is essential. In the presented setup, the amplitude is controlled by the exposure dosage and the phase is locked via a built-in feedback loop. When exposing the sample subsequently to four interference patterns with fixed phases and pitches of 4 µm, 2 µm, 1.33 µm, and 1 µm, respectively, a linear superposition of the patterns can be observed, as shown in Fig. 2. The inscribed sawtooth pattern can act for example as a blazed grating for diffractive optics.

In summary, the ability to select photolithographic inscription parameters and obtain immediate feedback on SRG formation via digital holographic microscopy opens up new possibilities for controlled surface patterning in applications such as optical Fourier surfaces and other complex DOEs. The examples presented were made possible by the unique combination of DHM and photolithography in azobenzene materials, enabling a one-step printing process to create the target patterns.

**References**


1. N. Tabiryan, D. Roberts, D. Steeves, B. Kimball, *Photonics Spectra*. **51** (2017) 46–50.
2. H. Rekola, A. Berdin, C. Fedele, M. Virkki, and A. Priimagi, *Sci. Rep*. **10** (2020) 19642.
3. A. Priimagi, A. Shevchenko, *J Polym Sci B Polym Phys* **52** (2013) 163–182.
4. A. Berdin, H. Rekola, A. Priimagi, *Adv. Optical Mater.* **12** (2024) 2301597.

# 2D materials for memristors

Mohamed Radwan[1], Seyed Hossein Hosseini-Shokouh[2], Catarina Dias[2], Abde Mayeen Shafi[1], Erxiong Ding[1], Faisal Ahmed[1], Zhipei Sun[1], Harri Lipsanen[1]

[1] *Department of Electronics and Nanoengineering, Aalto University, FI-02150, Finland*
[2] *Departamento de Física e Astronomia, Universidade do Porto, 4169-007 Porto, Portugal*

*Corresponding author: harri.lipsanen@aalto.fi)*

**Keywords:** memristor, 2D materials, semiconductors

In recent years, two-dimensional (2D) materials have garnered significant attention as promising candidates for neuromorphic applications.[1-2] These 2D materials, composed of single or few atomic layers, exhibit much stronger interactions within the x- and y-plane compared to the z-direction. This unique structure endows them with advantages such as flexibility, low operating voltage, high electrical endurance, and minimal energy consumption. The diverse properties of 2D materials include conductors like graphene, semiconductors such as black phosphorous and transition metal dichalcogenides (TMDs), and insulators such as boron nitride. Despite the popularity of graphene, its lack of a band gap has driven interest towards semiconducting 2D materials. Among these, molybdenum ditelluride ($MoTe_2$) emerges as a promising candidate, showcasing a large band gap, structural stability, and the ability to phase transition between the semiconducting 2H phase and the metallic 1T phase. Furthermore, $MoTe_2$'s ambipolar behavior distinguishes it from other materials like molybdenum disulfide ($MoS_2$), which exhibits inherent n-type semiconductor characteristics. A memristor or memory resistor is a two-terminal device capable of maintaining its internal resistance based on the previously applied voltage and current. The memristor is not an active element, meaning that it does not generate or store any power. What makes the memristor attractive is the similarity between its behavior and many of the learning processes in the brain. Our work demonstrates that $MoTe_2$ is a great candidate for future low-dimension neuromorphic computing.[3]

In this work, we utilized mechanically exfoliated $MoTe_2$ without any prior treatment to construct two innovative bio-inspired nano-devices: the memristor and the memtransistor. The fabrication process starts with the mechanical exfoliation of $MoTe_2$ by using a Scotch tape. The flakes are then transferred to a p-doped silicon substrate covered with a 285 nm thick $SiO_2$ layer with pre-deposited gold markers. $SiO_2$ is used as a gate insulator for memtransistor. After exfoliation, electron beam lithography is used for electrode patterning. A memristor, characterized by its two-terminal structure with an active material in between, can be configured either vertically or laterally. In the lateral configuration (Fig. 1 a), $MoTe_2$ is arranged horizontally between two parallel electrodes, spaced a few micrometers apart, requiring a relatively high switching voltage (5-10 V) as shown in Fig. 1 b. During voltage sweep processes 1 and 2 (i.e., 0 to 10 V to 0), the device is initially in a low resistance state (LRS) before switching to a high resistance state (HRS). This process is called the RESET process (i.e., increasing resistance or decreasing conductance). On the other hand, during the voltage sweep processes 3 and 4 (i.e., 0 to -10 V to 0), the device switches from HRS to LRS. This process is called the SET process (i.e., decreasing resistance or increasing conductance). Conversely, in the vertical configuration, where $MoTe_2$ is sandwiched between top and bottom electrodes, the electrode spacing is reduced to a few nanometers, resulting in a lower switching voltage (1-2 V). To avoid complexity, a lateral memristor was employed in this study. The second device, the memtransistor, incorporates an additional gate terminal to provide enhanced control over the device's transfer characteristics. A memtransistor combines memory and transistor functionality into a single device.

Both the memristor and memtransistor were fabricated, and their electrical characteristics, along with their ability to mimic synaptic behaviors, were thoroughly examined. The devices demonstrated excellent endurance stability, withstanding up to 400 cycles (Fig. 1 c). They also show the ability to mimic biological synapses under applied voltage pulses. These stimuli were able to strengthen or weaken the devices' resistance to imitate two biological synapse processes (long-term potentiation/depression). These promising results highlight the potential of $MoTe_2$-based nano-devices in advancing neuromorphic computing technologies.

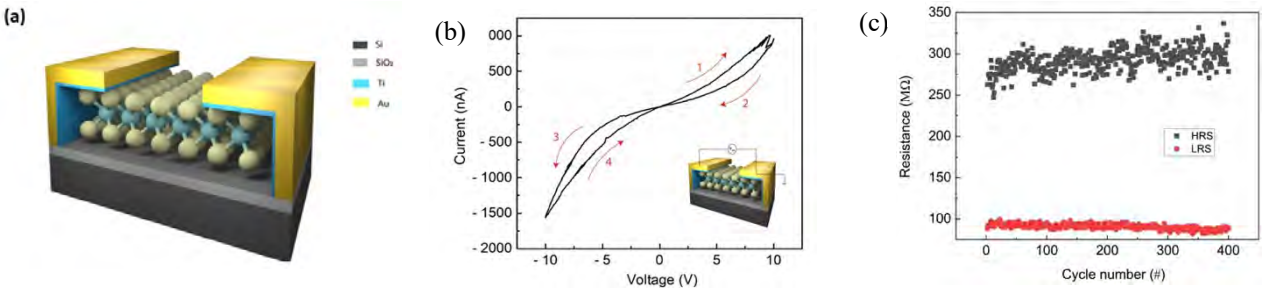


Fig. 1. a) Schematic of lateral $MoTe_2$ memristor. b) I-V characteristics of the device plotted in linear scale. d) Endurance of the $MoTe_2$ memristor measured at 1 V, HRS/LRS = high/low resistance state.

Leveraging the unique electrical properties of 2D materials, we successfully demonstrated bipolar resistive switching behavior in mechanically exfoliated $MoTe_2$-based memristors and memtransistors configured laterally. Fabricated using standard techniques, both devices exhibited outstanding endurance, maintaining functionality after 400 cycles, and effectively mimicked long-term potentiation and depression. These capabilities underscore their potential for high-performance neuromorphic computing. This work highlights the feasibility of using 2D $MoTe_2$ in memristive and memtransistor applications and paves the way for its integration into the next generation of neuromorphic computing technologies, promising enhanced efficiency and scalability. Our study is the first step to mimic more demanding real-life applications, such as in-sensor computing devices[4] that can perform several event-based human brain-inspired tasks such as audio/visual processing and identification.

**References**


1. J. J. Yang, D. B. Strukov, and D. R. Stewart, *Nature Nanotechnology* **8**, 13-24 (2013).
2. M. Wang *et al.*, *Nature Electronics 1*, 130-136 (2018).
3. M. Radwan, S. H. Hosseini-Shokouh, C, Dias, A.M. Shafi , C. Dias, F. Khalid, F. Ahmed, Z. Sun, and H. Lipsanen, "Dual Functionality 2D $MoTe_2$ Based Device as Memristor and Memtransistor for Neuromorphic Computing", submitted.
4. S. Seo, S.-H. Jo, S. Kim, J. Shim, S. Oh, J.-H. Kim, K. Heo, J.-W. Choi, C. Choi, S. Oh, D. Kuzum, H.-S. P. Wong and J.-H. Park, "Artificial optic-neural synapse for colored and color-mixed pattern recognition", Nature Communications 9, 5106 (2018).

# High-performance 3D-printed functional hollow waveguides for 200–400 GHz band applications

Kentaro Soeda[1], Kazunori Naganuma[1], Yoshinori Yamaguchi[1], Kuniaki Konishi[1], Hiroharu Tamaru[1], Norikatsu Mio[1], Hiroshi Ito[1], and Junji Yumoto[1]

[1] *Institute for Photon Science and Technology, The University of Tokyo, Tokyo, Japan*

*Corresponding author: yumoto@ipst.s.u-tokyo.ac.jp*

**Keywords:** THz, waveguide devices, 3D printer, metal plating

ABSTRACT: This study introduces a novel approach for fabricating hollow waveguide (WG) devices in the 200–400 GHz range, leveraging advanced 3D printing and metal plating techniques including bent WG, twisted WG, and spiral WG. These devices fabricated using 3D printing and metal plating achieve low insertion losses of less than 1 dB per inch. Furthermore, a Mach-Zehnder Interferometer (MZI) WG is demonstrated. This technology not only paves the way for the development of three-dimensional THz wave integrated circuits (3DTICs) but also represents a breakthrough in THz device miniaturization and functionality.

The terahertz (THz) band (above 100 GHz) is increasingly recognized for its potential in communication, sensing, and other applications. Realizing this potential requires not only advanced signal sources and detectors but also versatile devices such as frequency filters, polarization controllers, and wave combiners/splitters. While conventional metal WGs are widely used in the microwave and millimeter-wave bands, advancing to higher frequencies necessitates significant downsizing of WG dimensions. In the THz band, this leads to sub-millimeter-scale cross-sectional dimensions. For example, the standard WG cross-sectional dimensions for the 220–325 GHz band (J-band) are 0.86 × 0.43 mm². Additionally, the WG length must typically exceed 1 inch (25.4 mm), resulting in an aspect ratio greater than 30 for hollow WG structures. Traditional subtractive manufacturing techniques, such as mechanical machining, face significant challenges in fabricating these high-aspect-ratio, sub-mm scale hollow structures with precision.

3D printing facilitates the fabrication of hollow structures, including those with high aspect ratios, through a layer-by-layer manufacturing process. Despite extensive research on 3D printing [1], creating sub-millimeter-scale, high-aspect-ratio structures (smsHS) for THz WG devices remains a significant challenge.

To address this issue, we developed a state-of-the-art UV-curable resin-based 3D printer, RECILS [2], capable of fabrication with a resolution of 20–30 μm within a compact form factor. However, objects printed using RECILS do not inherently confine electromagnetic waves effectively. A practical solution to enable wave confinement is to coat the surface of RECILS-printed objects with metal. By combining RECILS and metal plating, we successfully fabricated low-loss WGs [3].Furthermore, we demonstrated bandpass filter (BPF) WG devices incorporating five internal resonators connected by a cavity iris. The bandpass characteristics of these devices closely align with simulation results for metal WGs with identical structures [4].

The WG manufacturing technology developed for the THz band using RECILS and metal plating can be extended to fabricate other functional WG devices. A twisted WG for the J-band was fabricated using RECILS, featuring a cross-sectional size of 0.86 × 0.43 mm² and standard UG387 flanges at both ends. The 180-degree twist at the center spans an 8-mm-long region (Fig. 1(a) and (b)).

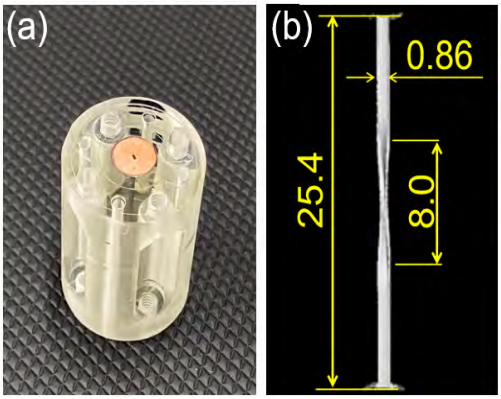


Fig. 1 (a) RECILS-printed waveguide for J-band (b) X-ray CT images of the twisted WG.

The insertion loss of the twisted WG is presented in Fig. 2, showing an average insertion loss of 0.37 dB per inch. This

value is nearly identical to that of a straight WG, indicating that the twisted structure does not introduce any additional loss.

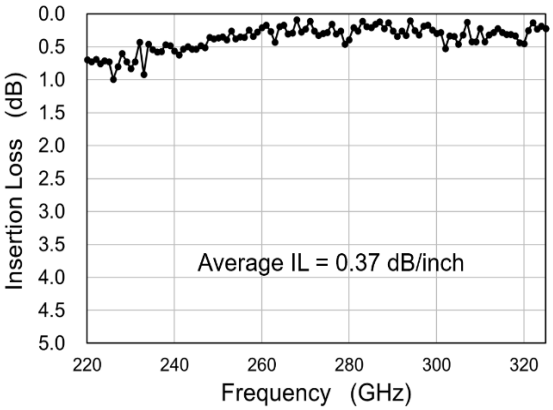


Fig. 2 IL of a twist WG. The average IL is 1.0 dB for 220 – 325 GH.

The twisted WG was fabricated using a mono-block (MB) method. In contrast, other 3D printers are unable to produce such structures directly, requiring the use of a split-block (SB) method instead. In the SB method, the internal features of the WG are precisely machined onto the mating surfaces of separate blocks. These machined blocks are then carefully aligned using alignment pins and secured together with screws [5]. As a result, WG circuit design in the SB method is restricted to the mating surfaces, allowing for the realization of only two-dimensional WG circuits. On the other hand, RECILS enables the fabrication of smsHS WGs using the MB method. This capability allows for the creation of three-dimensional free-form WG circuit designs.

Figure 3 illustrates the structure of a three-dimensional Mach-Zehnder Interferometer (MZI) WG. The design consists of two Y-branch WGs connected by coupling flanges at the two ports. Additionally, unbalanced MZI-WGs, featuring different branch lengths, can be easily fabricated. The Free Spectral Range (FSR) is controlled by adjusting the length difference between the two branch arms. Our results showcase FSRs of 10 GHz and 20 GHz with extinction ratios exceeding 20 dB, marking a significant advancement in THz waveguide design.

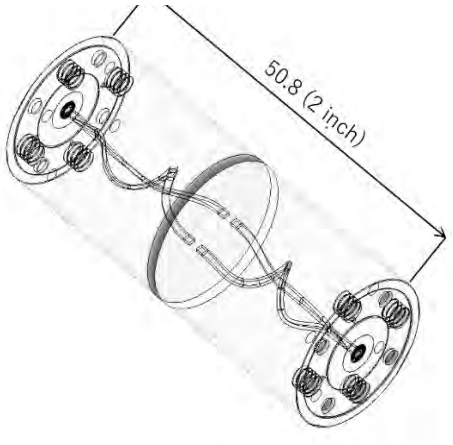


Fig. 3 Structure of 3D-MZI WG

In the THz band, 3D printing technology unlocks the potential to realize three-dimensional photonic integrated circuits (3DTICs), overcoming the limitations of conventional two-dimensional designs. This breakthrough not only overcomes the dimensional and precision limitations of traditional manufacturing techniques but also opens new horizons for wireless communication and sensing technologies, driving transformative innovation across industries.

This work was partly supported by JSPS KAKENHI Grant Number JP21H0132, the Beyond 5G R&D Promotion Program (JPJ012368C-00901) from the National Institute of Information and Communications Technology (NICT), Japan, MEXT-Quantum Leap Flagship Program, Grant Number JPMXS0118067246 and JST, CRONOS, Japan Grant Number JPMJCS24N6.

**References**

1. William J. Otter and Stepan Lucyszyn, Proceedings of The IEEE, vol. 105, pp 756-767, April 2017.
2. Kentaro Soeda, Hirosuke Suzuki, Shuichi Yokobori, Kuniaki Konishi, Hiroharu Tamaru, Norikatsu Mio, Makoto Kuwata-Gonokami and Junji Yumoto, Lasers in Manufacturing Conference 2021 Proceedings, https://wlt.de/sites/default/files/2021-10/system_technology_process_ control/Contribution_322.pdf.
3. Kentaro Soeda, Kazunori Naganuma, Yoshinori Yamaguchi, Kuniaki Konishi, Hiroharu Tamaru, Norikatsu Mio, Hiroshi Ito and Junji Yumoto, 47th International Conference on Infrared, Millimeter and Terahertz Waves (IRMMW-THz)IRMMW-THz 2022, https://doi.org/10.1109/IRMMW-THz50927.2022.9895857.
4. Kentaro Soeda, Kazunori Naganuma, Yoshinori Yamaguchi, Kuniaki Konishi, Hiroharu Tamaru, Norikatsu Mio, Hiroshi Ito and Junji Yumoto, Lasers in Manufacturing Conference 2023, https://wlt.de/sites/default/files/2023-09/Contribution_1132.pdf.
5. R. Payapulli, Lian Zhu, Sng-Hee Shin, Manoj Stanley, Nick M. Ridler and Stepan Lucyszyn, IEEE Access 11, 32272 (2023)

## *Session 3: Microstructures and Spectroscopy*

**Tuesday Jan 7, 2025**

13:40-14:00 Anthony Beaucamp: Micro-fluidic gate based on photo-rheological fluid
14:00-14:20 Katsuhiro Ishii: MicroLiDAR with multi-reference paths
14:20-14:40 Erik Vartiainen: Deep learning models in extracting Raman line-shapes from CARS
14:40-15:00 Yuri Svirko: CARS microscopy of diamond micro-needles
15:00-15:20 Jarkko J Saarinen: Raman spectroscopic characterization and quantification of brominated flame retardants (BFRs) in plastics

# Micro-Fluidic Gate based on Photo-Rheological Fluid

Motoi Watanabe[1], Okiharu Kirino[2], Anthony Beaucamp[1]
[1] *Department of System Design Engineering, Keio University, Yokohama, 223-8522, Japan*
[2] *Anax Optics Inc., Kohoku-ku, Shin-Yokohama, 222-0033, Japan*
*Corresponding author: beaucamp@sd.keio.ac.jp*

**Keywords:** photo-rheology, micro-fluidics

Photo-rheological fluids (PRF) have controllable viscosity as function of the wavelength of light with which they are irradiated. A light controlled micro-fluidic gate based on PRF is proposed and demonstrated, with 90% of the fluid exiting the intended outlet when the inlet flow is as high as 5 mm/s.

## 1. Introduction

Microfluidic systems control minute amounts of fluid in various applications including biochemistry, cell sorting, blood flow manipulation, and chemical synthesis [1]. Flow control can be achieved by varying the surface condition between hydrophobic and hydrophilic. Various methods have been used to create such surfaces, such as laser texturing, etching, or electrochemical processes [2], however this approach can only produce non-reconfigurable systems. The ability to dynamically control fluid flow through the application of an external force is thus desirable. Dielectrophoresis is a possible approach [3], although it requires imprinting electrodes on the surface which is time-consuming. Temperature control is another approach, in which a localized rise in temperature can cause fluid gelation [4] or convection [5] in some regions, around which the fluid is routed. However, the response time can be slow and the existence of temperature gradients renders fine control difficult. Instead, the use of photo-rheological fluids (PRF) based on light-sensitive cis-trans isomeric molecules is proposed here. The viscosity of a PRF can change reversibly depending on the wavelength of light irradiation. Hyuntaek et al [6] proposed inexpensive PRFs that can be made with commercially available components. It is proposed to use PRFs as microfluidic carrier fluid. By changing the viscosity in certain regions of the PRF, it is shown that the fluid flow direction can be affected with the fluid moving in the low-viscosity portion and stagnating in the high-viscosity portion.

## 2. Experimental Method

PRF was prepared by mixing pure water with 3.0 mM/L of ACA (azobenzene-4-carboxylic acid), 3.3 mM/L of NaOH, and 3.4 mM/L of Lipothoquad O/12 (di-POE(2) oleoyl methylammonium). Viscosity of the PRF under UV (365 nm) and visible (445 nm) irradiation was measured using a rheometer (HR10, TA). Next, a transparent fluid gate consisting of 1 inlet and 3 outlets, shown in Fig 1(a), was machined from an acrylic plate. The thickness of fluid between the bottom and top plate was set to 0.1mm, as shown in Fig 1(b), and the system was attached to a micro-syringe pump. The fluid gate was then installed into an experimental setup consisting of the 2 light sources and a photomask placed between the visible light source and gate. An inverted microscope with 2.5x objective and high-speed camera were used to record the motion of 10 µm glass beads (UVPMS-BG-1.00, Cospheric. Inc) suspended in the PRF. The OpenPIV software was used to analyze the motion of glass beads inside the microfluidic gate when UV only and UV+Visible irradiation is applied.


(a) Dimensions of fluid gate (b) Actual fluid gate (c) Experimental setup

Fig. 1. Design of fluid gate and experimental setup used for testing the photo-rheological fluid.

## 3. Results and Analysis

The results from Rheometer measurement are shown in Fig. 2. The viscosity quickly reduces as function of shear rate, reaching a condition similar to that of water around 30 $s^{-1}$. When the shear rate is low (1 $s^{-1}$), a noticeable difference is observed when the fluid is irradiated with UV only (32.4 mPa.s) and when it is irradiated with UV+Visible light (5.3 mPa.s). This means that the distribution of fluid viscosity can be controlled by using a single photomask to partially block the visible light, while simultaneously irradiating the entire area with UV. The results from particle image velocimetry (PIV) are shown in Fig. 3. When only UV irradiation is applied, the fluid flows generally from right to left, with a broadening of the flow region at the center of the gate. When an arc of visible light is applied between the inlet and the bottom outlet, the fluid instead flows preferentially between these 2 gates. The switch between the 2 states was found to occur within less than 1 second. For an inlet flow of 5 mm/s, over 90% of the fluid weas found to be exiting the cavity through the bottom outlet when irradiating with visible light.

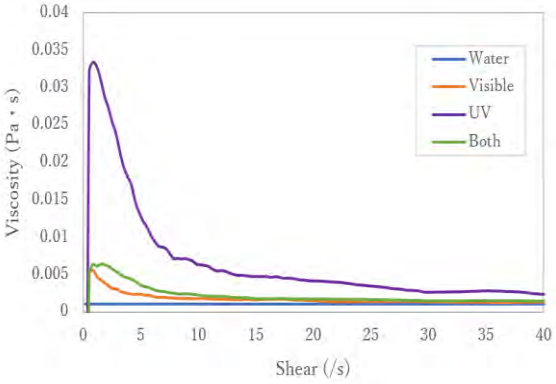


Fig. 2 Measured viscosity vs. shear rate

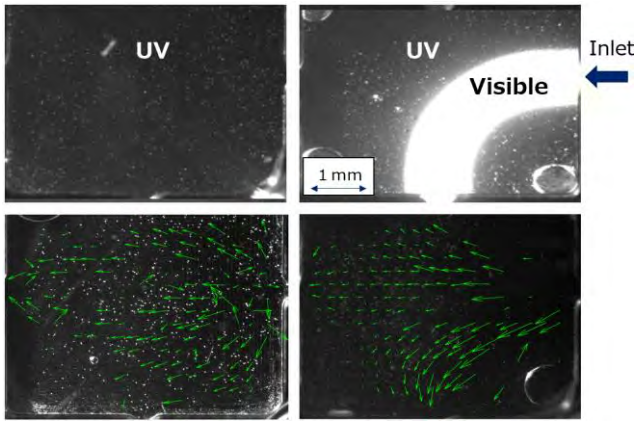


Fig. 3 Fluid flow under UV and UV/Visible irradiation

## 4. Summary and Outlook

The ability to control the direction of PRF fluid flow inside a micro-fluidic gate was demonstrated. A large change in viscosity was attained by irradiating the fluid inside gate with UV light and super-imposing a pattern of visible light passed through a photomask. The change in flow direction is rapid (less than a second) and reversible. Beyond the ability to control the flow of fluids in 2D to create fluid gates and separation devices, it is also expected that control of fluids in 3D should be possible by using a light-field based source of visible light [7]. It is expected that new types of micro-fluidic applications may become possible with 3D control of fluid flow, so this topic will be investigated in more details in future work.

## References


1. Tabeling, Patrick. Introduction to microfluidics. *Oxford university press* (2023).
2. Ge P, Wang S, Zhang J, Yang B. Micro-/nanostructures meet anisotropic wetting: from preparation methods to applications. *Materials Horizons*. **7(10)**, 2566-95 (2020).
3. Tatsumi K, Noma A, Honma R, Kuriyama R, Nakabe K. Particle timing and spacing control in microchannel flow by applying periodic force over space and time. *Microfluidics and Nanofluidics* **1-3** (2021).
4. Krishnan M, Erickson D. Optically induced microfluidic reconfiguration. *Lab on a Chip*. **12(3)**, 613-21 (2012).
5. Schmidt F, Vasista A, Ortega Arroyo1 J, Ruiz Reina E, Rica R, Quidant R. Dynamic 3D Optofluidic Control as a Multifunctional Platform for Microfluidic Applications. *Proc. EOSAM Naples* (2024).
6. Oh H, Ketner AM, Heymann R, Kesselman E, Danino D, Falvey DE, Raghavan SR. A simple route to fluids with photo-switchable viscosities based on a reversible transition between vesicles and wormlike micelles. *Soft Matter*. **9(20)**, 5025-33 (2013).
7. LePriol E, Sasaki A, Beaucamp A. Light-field based 3D optical tweezer. *Proc. EOSAM Naples* (2024).

# MicroLiDAR with multi-reference paths

Katsuhiro Ishii[1], Neisei Hayashi[1], Takahiro Deguchi[2],
Ryo Nomura[2], Hiroshi Hasegawa[2], Hideaki Furukawa[3]

[1] *The Graduate School for the Creation of New Photonics Industries, Hamamatsu, Shizuoka*
[2] *Nadex Co., Ltd., Tsuruga, Fukui*
[3] *National Institute of Information and Communications Technology, Koganei, Tokyo*
*Corresponding author: ishii@gpi.ac.jp*

**Keywords:** Optical ranging, low-coherence interferometer, time stretch dispersive Fourier transform

MicroLiDAR is an optical ranging method with a resolution of micrometers and is capable of high repetition measurements at 10 MHz or higher. It consists of a low-coherence interferometer that uses an ultrashort pulsed laser as a light source and performs high-repetition spectroscopic measurements using Time stretch dispersive Fourier transform. In this presentation, we demonstrate that an interferometer with multiple reference paths of different lengths can extend the measurement range without compromising measurement rate and resolution. Our MicroLiDAR system with center wavelength of 1550 nm had repetition rate of 10 MHz and resolution of 10 μm, and measurement range of 16mm. By using an interferometer with four reference paths, the measurement range was expanded to 50 mm.

Real-time measurement of keyholes generated during laser welding is an important technology for controlling laser welding [1-4]. Low-coherence interferometers can be applied to real-time keyhole measurement. We developed a high-speed optical ranging system using a low-coherence interferometer and time stretch dispersive Fourier transform, which is named microlidar [5,6]. Microlidar is succeessfully applied to real-time measurement of keyhole shape during laser welding. The developed microlidar system uses an ultrashort pulse light source with a central wavelength of 1550 nm and a repetition rate of 10 MHz, and acquired interference signals is recoreded byan oscilloscope with a frequeccy band of 15 GHz. The measurement repetition rate is 10 MHz, the distance resolution is 10 μm, and the measurement range is 16 mm. A wider measurement range is required for measuring the welding of thick steel plates. In this papaer, we proposed a method to expand the measurement range by dividing the reference path into multiple paths with different lengths. This makes it possible to expand the measurement range without reducing the distance resolution and repetition rate by using a detection system with the same frequency band.

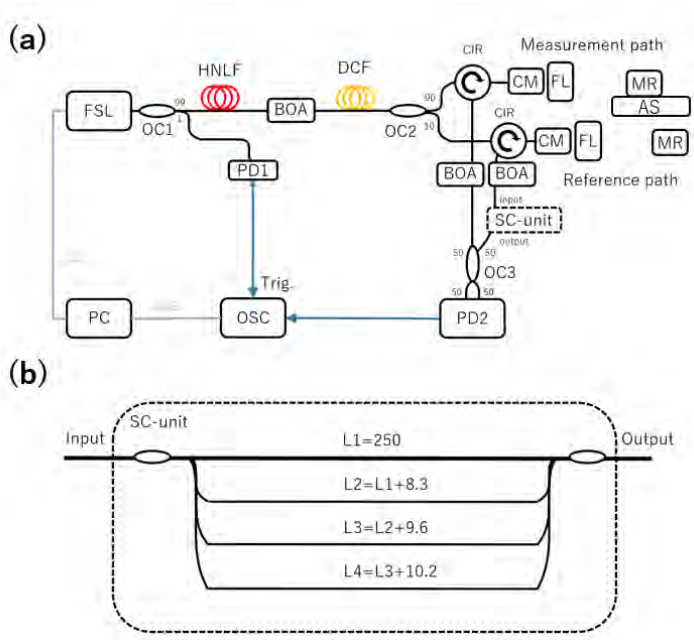


Fig.1 (a) Experimental setup (AS; auto stage, CM; collimator, BOA; Booster optical amplifier, DCF; dispersion compensated fiber, FSL; femto-second laser, FL; focus lens, HNLF, highly nonlinear fiber, MR; miller, OC; optical coupler, OSC; oscilloscope, PD1; single photodetector, PD2; balanced photodetector, PC; personal computer, SC-unit: simplified cascaded reference arm unit), (b) configuration of SC-unit. The lengths of each arm (L1~L4) are different.

Figure 1 shows the experimental setup. The light source is optical fiber base femto-second laser (FSL) with repetition rate of 10 MHz, the average peak power of 6 dBm, The center wavelength of 1550 nm and pulse width of 450 fs. A 20-m-long highly nonlinear fiber (HNLF) is used to extend the wavelength range of light source. Then, the

light is amplified by a broadband semiconductor optical amplifier (BOA) and stretched by 7-km-long dispersion compensating fiber (DCF). The total dispersion was 935 nm/s. Optical fiber coupler (OC2) divided into a measurement light and a reference light. The measurement light is irradiated onto the sample. The reflected light from the sample is merged with the reference light that passed through the SC-unit. The SC-unit is shown in Fig.1 (b). The reference light is divided into four and each light is merged to one by an optical coupler. The length of each path is set to 250 mm, 258.3 mm, 267.9 mm, and 278.1 mm. The interference signal is converted to an electrical signal with a balanced photo detector (BPD) with frequency range of 23 GHz. The electrical signals are recorded by an oscilloscope (frequency range: 15 GHz, keysight, DSO81304A) and then analyzed with a personal computer.

Figure 2 shows the interference signals and FFT results of them for three positions of sample mirror. Horizontal axis of FFT result is frequency of interference signals, which correspond to the optical pathlength difference between the measurement light and reference light. Since the reference light has four different pathlength, several peaks observed in FFT result. For one reference light, an interference signal is observed over a range of about 14 mm. over a range of 50 mm, an interference signal with one of the reference lights is observed. Since multiple interference signals are observed simultaneously and the optical path length difference of each reference light is different, the distance can be estimated from multiple peaks over the entire range. We also attempt to automatically estimate distance using dual entry method, a type of machine learning. In the presentation, The details of the results will be reported.

We demonstrated the 50-mm-long distance measurement with MicroLiDAR including SC-unit. After analyzing the acquired data with the fast Fourier transform to calculate the distance, we obtained the actual distance ranging from 0 mm to 50 mm.

**References**


1. Y. Feng, X. Gao, Y. Zhang, C. Peng, X. Gui, Y. Sun, and X. Xiao, The International Journal of Advanced Manufacturing Technology, **112**, 2301–2312 (2021).
2. T. R. Allen, W. Huang, J. R. Tanner, W. Tan, J. M. Fraser, and B. J. Simonds, Physical Review Applied, **13**, 064070 (2020).
3. J.J. Blecher, C.M. Galbraith, C. Van Vlack, T.A. Palmer, J.M. Fraser, P. J. L. Webster and T. DebRoy, Science and Technology of Welding and Joining, **19**, 560–564 (2014).
4. Z. Zhang, Y. Huang, R.Q. Z. Lei, and G. Wen. IEEE Transactions on Instrumentation and Measurement **70**, 1-10 (2021).
5. M. Hoshikawa, K. Ishii, T. Makino, T. Hashimoto, H. Furukawa, and N. Wada, Opt. Rev. **27**, 246–251 (2020).
6. N. Hayashi, M. Hoshikawa, K. Ishii, T. Fujita, M. Kanamori, T. Deguchi, R. Nomura, H. Hasegawa, T. Makino, T.Hashimoto, H. Furukawa,and N. Wada, Optics Express **29**, 32169-32178 (2021).


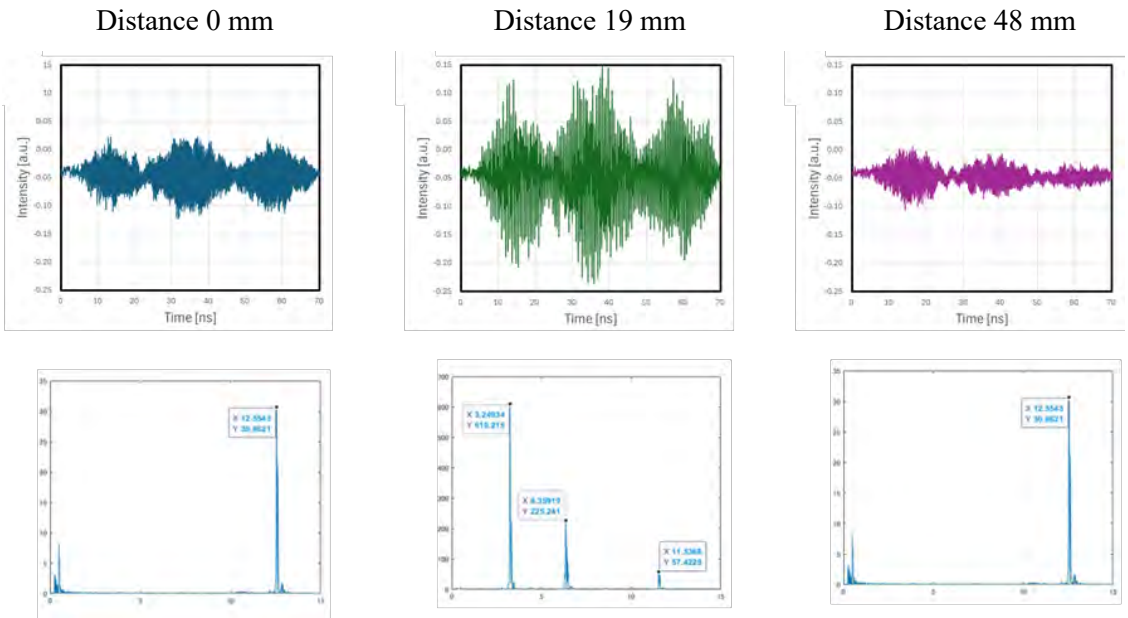


Fig. 2. Measurement results on time-domain and frequency-domain region with MicroLiDAR

# Deep learning models in extracting Raman line-shapes from CARS

Rajendhar Junjuri[1], Ali Saghi[2], Lasse Lensu[2] and Erik M. Vartiainen[2]

[1] *Leibniz Institute of Photonic Technology, 07745 Jena*

[2] *LUT School of Engineering Sciences, LUT University, 53851 Lappeenranta*

*Corresponding author: erik.vartiainen@lut.fi*

**Keywords:** CARS microspectroscopy, deep learning, Raman signal extraction

Coherent anti-Stokes Raman scattering (CARS) microspectroscopy offers a powerful tool for label-free, quantitative, chemically specific, and submicron 3D imaging of samples in material and life sciences [1, 2]. However, achieving chemical specificity and quantitative analyses requires extracting Raman signals from CARS spectra [3-5]. Moreover, retrieving this information should be unsupervised to be practical in microscopic imaging. In this work, we evaluate four deep learning (DL) models – Convolutional Neural Network (CNN) [6], Long Short-Term Memory (LSTM) [7], Very Deep Convolutional Autoencoder (VECTOR) [8], and Bi-directional LSTM (Bi-LSTM) [9] – for retrieving Raman signals from CARS spectra.

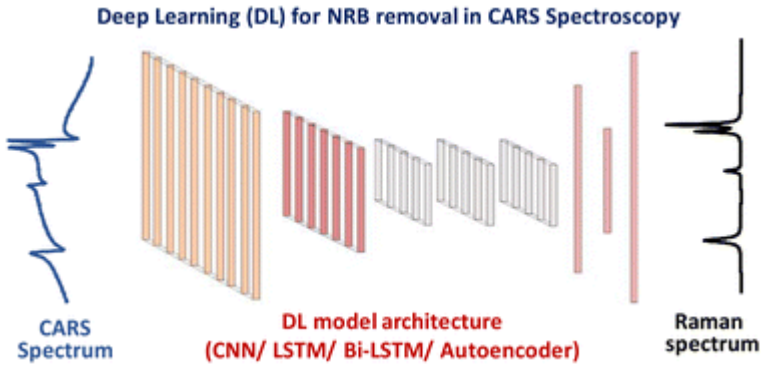


Fig. 1. An example of a convolutional neural network model. Data (CARS spectrum) is fed to the input layer, processed in the hidden layers and output is the predicted Raman signal [10].

The deep learning models were trained using synthetic CARS spectra. A dataset of 50,000 spectra was generated for training purposes, incorporating randomness in the nonresonant background (NRB), peak amplitude, linewidth, and noise levels to simulate various realistic conditions. The trained models were tested on synthetic and experimental datasets to assess their efficiency in retrieving Raman signals. The CNN and VECTOR models were based on previously established architectures, while the LSTM and Bi-LSTM models were explored for the first time for this application. The Bi-LSTM architecture included three bidirectional layers designed to process input data sequences in both forward and backward directions, thereby improving how the long-term dependencies in spectral data are taken into account [10].

The Bi-LSTM showed the best performance on synthetic test data among the four models. The Bi-LSTM model achieved a mean squared error (MSE) that was 60 times lower than that of the other models and showed a high Pearson correlation coefficient (PCC) above 0.99 for 94% of the test spectra. It consistently predicted the Raman spectral lines across the full spectral range, including regions with weak signals or near the edges of the spectral range, where the other models struggled. The CNN and VECTOR models showed good performance in mid-spectrum regions, but they failed to predict certain peaks near the spectrum boundaries, leading to higher MSE values. The LSTM model showed weaker predictive capability, with lower PCC values across most test spectra.

The models were further tested on experimental CARS data obtained from various biological and material samples, including proteins, lipids, yeast cells (Fig. 2), and nucleotide mixtures (ADP, AMP, and ATP). The Bi-LSTM model outperformed the others, providing accurate Raman signal predictions for most samples. In particular, it successfully retrieved important spectral features such as amide I and III bands in protein samples and lipid CH stretching bands. While the VECTOR and CNN models performed well in regions with strong Raman signals, they introduced noise or missed weak signals in complex spectra. The LSTM model underperformed significantly in both synthetic and experimental scenarios, often introducing spurious signals or broadening spectral lines.

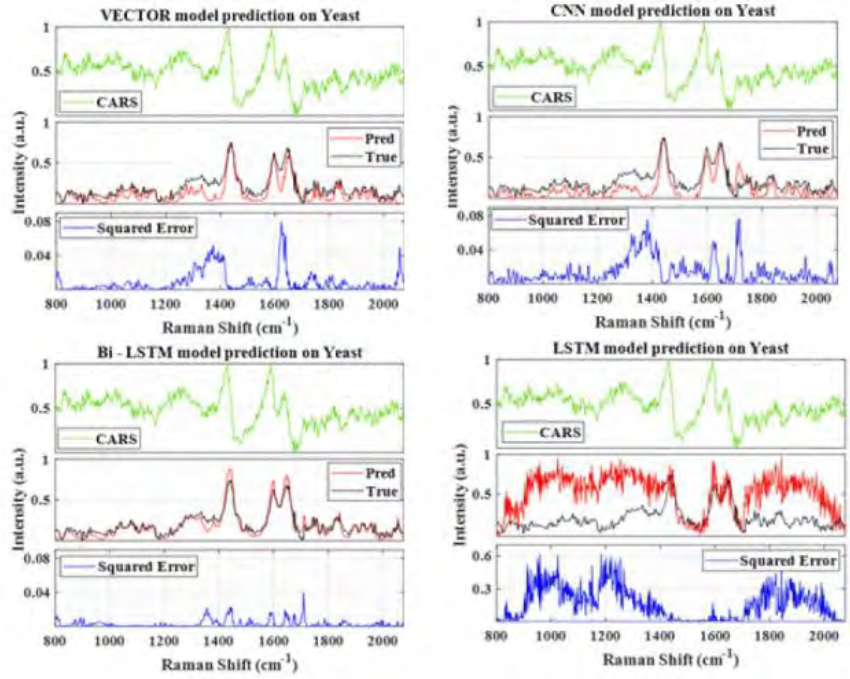


Fig. 2. Test results using CARS (green line) and Raman (black line) spectra of a yeast sample. The predicted Raman spectra are shown with red line, and the prediction error with blue.[10]

This study demonstrates the potential of deep learning for automating the extraction of Raman signals from complex CARS spectra. The Bi-LSTM model, with its bidirectional architecture, proved to be the most effective at handling spectral line shapes and resolving weak or overlapping signals. These results suggest that deep learning can provide a robust alternative to traditional numerical methods for CARS data analysis. Future work will focus on refining the model by introducing additional training data that account for varying noise levels and expanding the model's application to other spectroscopic techniques.

**References**


1. A. Zumbusch, G. R. Holtom, and X. S. Xie, *Phys. Rev. Lett.* **82**, 4142-4145 (1999).
2. M. Müller and A. Zumbusch, *ChemPhysChem* **8**, 2156-2170 (2007).
3. E. M. Vartiainen, H. A. Rinia, M. Müller, and M. Bonn, *Opt. Express* **14**, 3622-3630 (2006).
4. C. H. Camp Jr, Y. J. Lee, and M. T. Cicerone, *J. Raman Spectrosc.* **47**, 408-415 (2016).
5. Y. Kan, L. Lensu, G. Hehl, A. Volkmer, and E. M. Vartiainen, *Opt. Express* **24**, 11905-11916 (2016).
6. C. M. Valensise, A. Giuseppi, F. Vernuccio, A. De la Cadena, G. Cerullo, and D. Polli, *APL Photonics* **5**, 61305 (2020).
7. R. Houhou, P. Barman, M. Schmitt, T. Meyer, J. Popp, and T. Bocklitz, *Opt. Express* **28**, 21002-21024 (2020).
8. Z. Wang, K. O' Dwyer, R. Muddiman, T. Ward, C. H. Camp, and B. M. Hennelly, *J. Raman Spectrosc.* **53**, 1081-1093 (2022).
9. S. Zhang, D. Zheng, X. Hu, and M. Yang, in *Proceedings of the 29th Pacific Asia Conference on Language, Information and Computation*, p. 73–78, Shanghai, China, 2015.
10. R. Junjuri, A. Saghi, L. Lensu and E. M. Vartiainen, *Phys. Chem. Chem. Phys*. **25**, 16340-16353 (2023).

# CARS microscopy of diamond micro-needles

Yuri Svirko[1], Andrej Dementjev[2], Renata Karpicz[2], Bo Xu[1], Sergei Malykhin[1], Polina Kuzhir[1]

[1]*Department of Physics and Mathematics, University of Eastern Finland, Joensuu, Finland*

[2]*Department of Molecular Compounds Physics, State research institute Center for Physical Sciences and Technology, Vilnius, Lithuania*

*Corresponding author: yuri.svirko@uef.fi*

**Keywords:** nonlinear optical spectroscopy, CARS, nanotechnology, diamond color centers

Exceptional thermal conductivity and broadband transparency has made diamond a material of choice for numerous applications spanning from high-power electronics to the hostile environment sensing. Diamond has recently emerged as a particularly promising platform for sensing, which employs a long spin coherence time of color centers at room temperature [1]. Quantum sensing devices can employ diamond needles (DNs), which can be fabricated by plasma enhanced chemical vapor deposition (CVD) [2]. At the length of several micrometers, the DN enriched with nitrogen–vacancy (NV) and silicon-vacancy (SiV) centers provides the efficient collection of PL photons from its tip having apex curvature of 2-10 nm thus enabling a sensing with nanoscale spatial resolution [3]. It is worth noting that the symmetry and homogeneity of the crystalline field in the vicinity of the color center determines quantum sensing performance. However, the important question on the DN apex crystallinity remains unanswered. Specifically, distortion of the crystal lattice over the DN length may complicate quantum applications, which essentially rely on the prescribed orientation of color centers within unit cell of the diamond lattice. Moreover, $sp^2$-hybridized carbon atoms in the vicinity of the apex will scatter or absorb photons emitted by a color center thus reducing signal-to-noise ratio.

We demonstrate the needle crystallinity can be visualized by polarization sensitive Coherent anti-Stokes Raman scattering (CARS) microscopy. By measuring the resonant CARS signal over the whole needle we proved that the crystallinity of 70 micrometers long diamond needle remains the same in the micrometers thick base and in the nanometers' thin apex. This result was confirmed by the measurements of the linewidth of the SiV color center.

In our experimental conditions, the anti-Stokes wave at the frequency $\omega_{AS} = 2\omega_P - \omega_S$ , where $\omega_P$ and $\omega_S$ are frequencies of the pump and Stokes beams, is determined by the third-order nonlinear polarization $P^{(3)}(\omega_{AS})$ of the diamond and the thickness of the needle:

$$P_i^{(3)}(2\omega_P - \omega_S) = \chi_{ijkl}^{(3)} E_{Pj} E_{Pk} E_{Sl}^* \qquad (1)$$

where $\boldsymbol{E}_P$ and $\boldsymbol{E}_S$ are amplitudes of the pump and Stokes beams, $\chi_{ijkl}^{(3)}$ is the tensor of the third-order susceptibility of diamond. The intensity of the measured CARS signal is determined by the polarization of the interacting waves.

The intensity of the CARS signal measured after analyzer oriented at angle $\alpha$ with respect to the X-axis of the laboratory frame is given by the following equation:

$$I_{CARS} \propto \cos^2(\phi - \alpha) + a^2[(\sin 2\phi \sin(\phi + \alpha) + \sin^2 2\psi \sin^3 \phi \sin \alpha]^2 \qquad (2)$$

where $a$ is the ratio of the resonant and non-resonant nonlinear susceptibility of the diamond, $\phi$ and $\psi$ determine orientation of the [110] axis and polarization azimuth of the pump and Stokes beams with respect to the X axis of the laboratory frame (see Fig.1a).

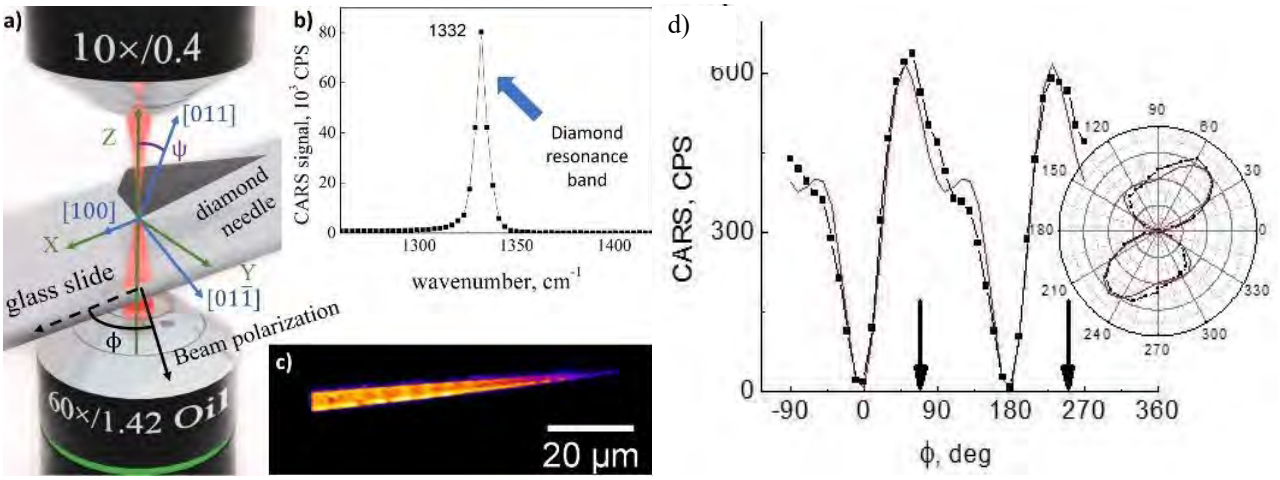


Fig. 1 (a) CARS microscope setup. The orientation of the polarization azimuth of the collinear pump and Stokes beams is determined by angle $\phi$, which is controlled by rotating an achromatic λ/2 plate placed before the oil objective. Angle $\psi$ between the slide normal and [011] crystallographic axis of diamond defines orientation of the needle on the glass slide. Cartesian laboratory axes {XYZ} are also shown. In the polarization-resolved experiment, the analyzer was placed after the objective collecting the anti-Stokes signal. (b) The spectrum of the CARS signal in counts per second. (c) CARS image of the needle recorded at $\omega_P - \omega_S$ = 1332 $cm^{-1}$. (d) CARS signal as a function of $\phi$ measured at the analyzer orientation of α= 70 degrees (black arrows). The solid red lines show fitting at $a^2$ = 17400, $\psi$ = 40°.

The performed measurements [4] showed that a very strong Raman-like band at 1332 $cm^{-1}$ makes it possible to employ CARS microscopy for visualization of the crystallinity over the several micron long diamond needle by exploring the pronounced polarization dependence of the CARS signal. By mapping CARS signals over the whole needle we demonstrate that the needle is a single crystal, i.e. the quality of the diamond lattice and orientation of the crystallographic axes are the same in both several micron thick base and a nanoscale thin tip of the needle. The measured polarization-sensitive CARS spectra are well described in terms of the third-order nonlinear optical susceptibility of the diamond. High crystal quality of DNs was verified by showing that FWHM of the SiV color centers emission does not depend on the color center position in the needle. The developed polarization-resolved CARS microscopy technique, which is capable of mapping diamond crystallinity with micrometer precision, can complement the local high-resolution electron microscopy and X-ray diffraction usually applied for the millimeter- scale crystals for diamond diagnostics.

**References**


1. E.D. Herbschleb, et al, Nat. Commun. 10(1), 3766 (2019).
2. A.N. Obraztsov et al, Diam. Relat. Mater. 18(10), 1289 (2009).
3. S. Malykhin, et al," Diam. Relat. Mater. 125, (2022).
4. A. Dementjev et al, Appl. Phys. Lett, 124, 211903 (2024)

# Raman spectroscopic characterization and quantification of brominated flame retardants (BFRs) in plastics

Mahtab Ashraf[1], Ville H. Nissinen[1], Ilkka Rytöluoto[2], Milad Mosallaei[2], Kirsi Korpijärvi[3], Janne Jänis[1] and Jarkko J. Saarinen[1]

[1] *Department of Chemistry and Sustainable Technologies, University of Eastern Finland, Joensuu, Finland*
[2] *VTT Technical Research Centre of Finland Ltd., 33101 Tampere, Finland*
[3] *VTT Technical Research Centre of Finland Ltd., 40400 Jyväskylä, Finland*
*Corresponding author: jarkko.j.saarinen@uef.fi*

**Keywords:** Raman scattering, recycling, plastics, brominated flame retardants (BFRs)

Plastics are one of the most commonly used materials in many applications, especially in consumer products such as electronics and packaging. Traditionally, plastics are derived from fossil fuels from which approximately 4 to 6 % are consumed in plastics manufacturing. Use of plastics has grown steadily since the 1950s and is expected to rise globally. Current production of plastics is more than 400 million tons annually, and almost 10 billion metric tonnes of plastics have been manufactured since their invention around hundred years ago. Out of the 10 billion primary production of plastics, only less than 10 % has been recycled [1].

Plastics have versatile physical and chemical properties that can be tailored by various additives including antioxidants, flame retardants, light stabilizers, and plasticizers that are mixed into the polymer matrix during manufacturing for improved properties. [2] Flame ratardants (FRs) are typically added into plastics of electric and electronic equipment to delay combustion, and they are commonly found in vehicles, construction materials, and furniture in the range of 5–30 wt-%. Among FRs, halogenated FRs and especially brominated FRs (BFRs) are the most widely used additives. Unfortunately, many BFRs are very stable, bioaccumulative, and hazardous thus posing a significant risk both for the environment and human health. Therefore, some BFRs such as polybrominated diphenyl ethers (PBDEs) are already strictly regulated by the European Union. It is thus vital to identify and quantify the amounts of such materials especially in the recycled plastic streams.

Commercially used plastics are typically mixtures of different types of polymers and additives. Therefore, accurate and multi-technique characterization is needed to improve recyclability and circularity. Some common analytical techniques are, for example, thermal analytical tools (differential scanning calorimetry DSC), chromatography (gel permeation chromatography GPC), mass-spectrometry (trapped ion mobility MS), and spectroscopic techniques (NMR, IR, and Raman spectroscopy),

In this paper we use Raman spectroscopy to measure the amount of BFRs and $Sb_2O_3$ in micro compounded model polymer samples. The Raman intensities displayed are interlinked to X-ray fluorescence (XRF) quantification of bromine content. Figure 1 shows the measured Raman spectra from different samples. The ABS backbone characteristic peaks were observed around 1 000 $cm^{-1}$ (C-C stretching) and 1 450 $cm^{-1}$ ($CH_2$ deformation). TBBPA exhibited unique peaks between 200–1 200 $cm^{-1}$ indicating C-Br, C-O stretching and aromatic ring vibrations. $Sb_2O3$ exhibited peaks around 140 to 260 $cm^{-1}$ (Sb=O vibrations and Sb-O-Sb bending). Finally, deca-BDE exhibited distinct peaks around 1 500 $cm^{-1}$ (aromatic C=C stretching) and relatively strong features near 100–250 $cm^{-1}$ that are associated with the C-Br stretching.

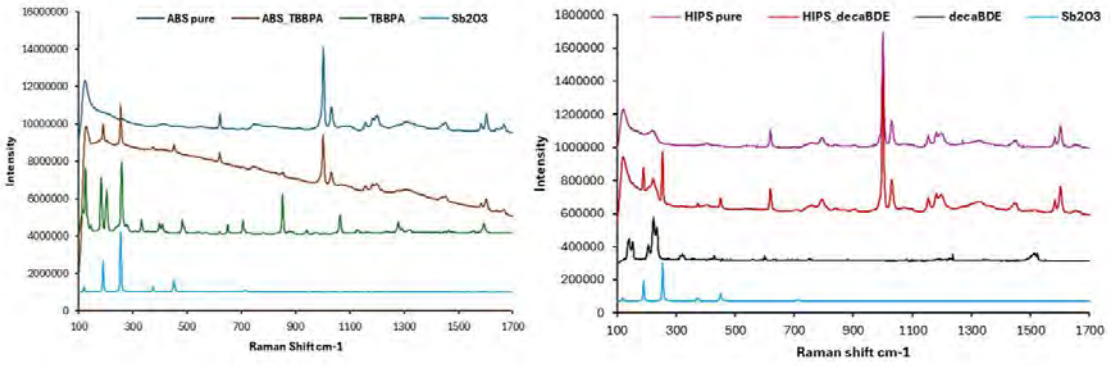


Fig. 1. Raman spectra of ABS with TPPBA and $Sb_2O_3$ (left) and HIPS with decaBDE and $Sb_2O_3$ (right)

Two different polymer matrices were used: high-impact polystyrene (HIPS) and acrylonitrile butadiene styrene (ABS) were mixed together with a known concentration (0 – 10 wt%) of bromine in BFR. Three most common BFRs were investigated: tetrabromobisphenol A (TBBPA), hexabromocyclododecane (HBCD), and decabromodiphenyl ether (deca-BDE). In addition, a common synergist, antimony trioxide ($Sb_2O_3$), which is commonly used together with BFRs was added in a $Sb_2O_3$ / BFR ratio of 1:2 (w/w). All Raman spectra were acquired under an excitation wavelength of 785 nm since excitation at 514 nm generated a significantly higher level of fluorescence. However, the HBCD containing samples were highly fluorescent even at 785 nm excitation preventing Raman signal analysis.

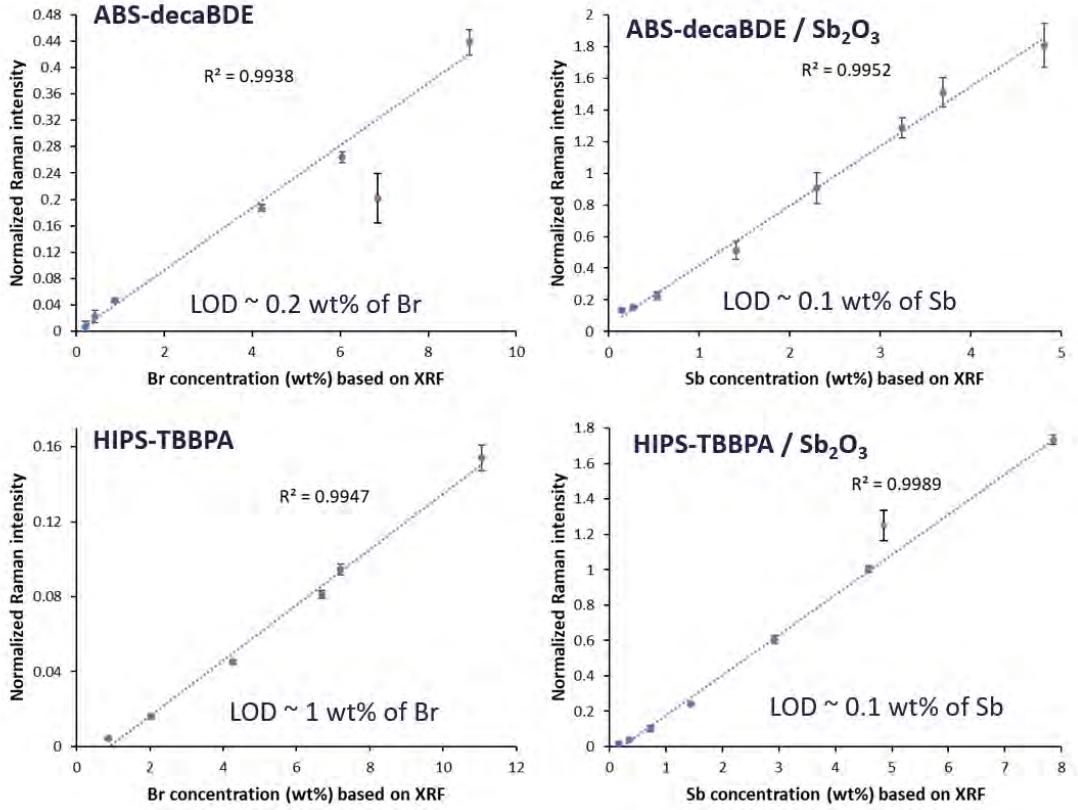


Fig. 2. Correlation between Raman spectra and XRF quantification of bromine and antimony for ABS-deca-BDE (top) and for HIPS-TBBPA (bottom).

Figure 2 shows the observed correlation between the measured Raman spectra and the XRF quantification for different polymers and BRFs together with synergist antimony trioxide. It can be concluded that for both studied polymers (HIPS, ABS) and for both studied BFRs (TBBPA, deca-BDE) the observed correlation between Raman and XRF measurements was excellent with $R^2$=0.98 or higher.

As a summary, it was demonstrated that Raman spectra can be used to identify and further to quantify BFRs directly from plastic samples without any sample preparation. The observed correlations between the Raman and XRF measurements were excellent.

In general, there is a significant demand for solutions to provide ecologically, economically, and environmentally friendly solutions for circular plastics. To enhance recyclability and circularity it is crucial to identify and quantify the content of the recycled plastic waste streams accurately that will allow their usage in value-added applications. It is believed that Raman analytics can provide solutions for such analytics in plastics recycling.

This work was supported by the European Union from the Horizon Europe Programme through the European Health and Digital Executive Agency (HADEA) under Grant Agreement No. 101057067.

**References**

1. R. Geyer, J. R. Jambeck, and K. L. Law. Production, use, and fate of all plastics ever made. *Sci. Adv.* **3**, e1700782 (2017). https://doi.org/10.1126/sciadv.1700782.
2. R. Pfaendner, *Polymer Additives* in *Handbook of Polymer Synthesis, Characterization, and Processing*; Eds. E. Saldivar-Guerra and E. Vivaldo-Lima, (John Wiley & Sons: Newark, United States, 2013), pp 225−247.

## *Session 4: Optical Measurements*

**Wednesday Jan 8, 2025**

8:30-8:50 Aleksandr Danilenko: Application of a bandwidth correction method to thin-film reflectance measurements

8:50-9:10 Koyo Watanabe: Precision measurement of chromatic dispersion using a femtosecond-resolution pulse shaper and autocorrelator

9:10-9:30 Yusuke Ogura: Spatial photonic Ising machine using a digital micromirror device

9:30-9:50 Takamasa Suzuki: Down-sampling vibration-measurement technique based on a laser diode interferometry

9:50-10:10 Ryohei Hanayama: Development of body surface vibration meter using speckle shearing interferometer

# Application of a bandwidth correction method to thin-film reflectance measurements

Aleksandr Danilenko[*1], Masoud Rastgou[1], Farshid Manoocheri[1], and Erkki Ikonen[1,2]

[1]*Aalto University, Metrology Research Institute, Maarintie 8, 02150 Espoo, Finland*

[2]*VTT MIKES, Tekniikantie 1, 02150 Espoo, Finland*

* *Corresponding author: aleksandr.danilenko@aalto.fi*

**Keywords:** Richardson-Lucy method, bandwidth correction, reflectometry technique, thin-film measurements.

The bandpass function is a crucial aspect of monochromators and array spectrometers that can influence measurement accuracy, especially in samples with sharp spectral features, such as narrow-band filters or thick-coated thin films. One method for measuring thin-film thicknesses is reflectometry [1-3], a non-destructive technique that analyzes the reflected light spectrum from the film's surface.

To improve accuracy in reflectance measurements, bandwidth correction software is often used to deconvolute the measured spectrum as if it were obtained with a narrow bandpass function [4]. In reflectometry, achieving a good fit between the measured and fitted spectrum is essential for accurate results. To evaluate bandwidth correction methods for thin-film applications, we analyzed the reflectance spectrum of a 2-µm-thick $SiO_2$ coating on a Si wafer. This analysis involved comparing the bandwidth corrected measured spectrum with a simulated one, generated using MATLAB software based on the transfer-matrix method [5].

The measurements were performed using a Sentech RM 2000 array spectrometer [6], which has a 4 nm bandwidth. The simulation fits the sample's physical parameters, such as layer thickness, to match the corrected measured spectrum. The model uses two fitting parameters: the average thickness of the $SiO_2$ layer and the width of its thickness distribution. The average thickness is the primary parameter, while the distribution width reflects the assumption that the $SiO_2$ layer's thickness may vary within the spot size of the reflectometer.

The results of fitting show an average layer thickness of about 2015 nm, with the thickness varying between 2010 and 2019 nm. Figure 1(a) illustrates the measured, corrected, and simulated spectra, while Figure 1(b) highlights the differences between bandwidth corrected and uncorrected spectra.

Most notable differences occur at shorter wavelengths due to narrower peak widths, indicating that bandwidth correction is more impactful for sharp peaks, while flatter data, such as with thinner layers, remains largely unchanged. Another effect of bandwidth correction is the appearance of artificial spikes near the wavelength range edges, seen in the gray-shaded areas of Figure 1. These artifacts are typical for Richardson-Lucy method [4], and to avoid them, the analysis range was limited to 310-940 nm instead of 300-950 nm.

The reliability of the fitting model is assessed through sensitivity analysis [3]. A noticeable deviation occurs when the layer thickness differs from the optimal value by 5 nm. The standard uncertainty due to the fitting model is 2.9 nm. Taking into account other uncertainty components leads to the combined standard uncertainty of 5.3 nm.

This study emphasizes the significance of bandwidth correction for accurately measuring thin-film layer thickness using the reflectometry technique. By analyzing the reflectance spectrum of a 2-µm-thick $SiO_2$ layer on a silicon wafer, the key features and advantages of the Richardson-Lucy correction method were demonstrated. Utilizing Richardson-Lucy corrected data yields a more dependable estimation of layer thickness with reflectometry, as the simulated spectrum is aligned with the bandwidth corrected spectrum, effectively reducing the impact of the known spectrometer bandwidth.

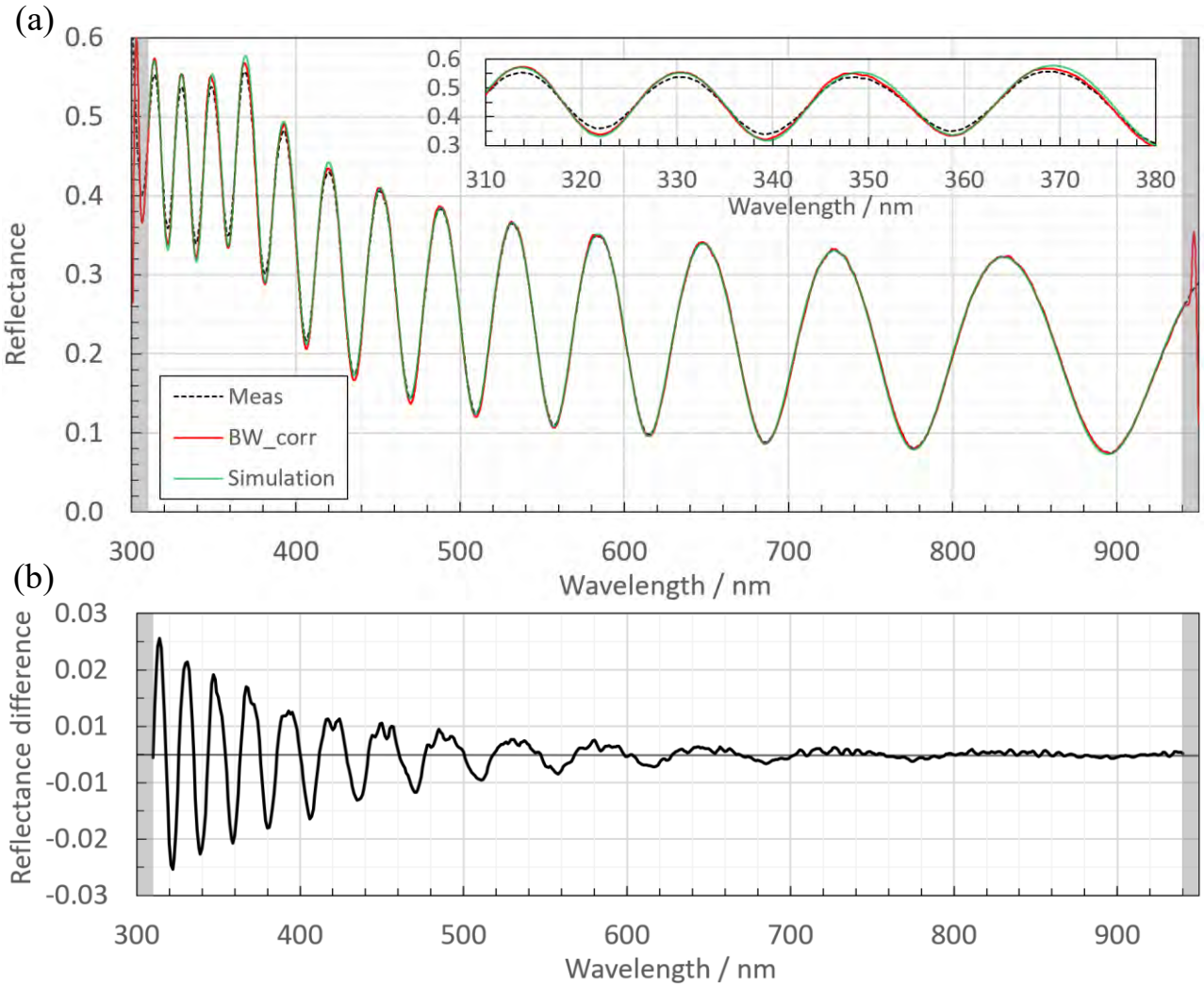


Fig. 1. (a) Measured (Meas), bandwidth corrected (BW_corr) and simulated spectra.
(b) Reflectance difference between bandwidth corrected and uncorrected spectrum.

**Acknowledgments**

The project 20IND04 ATMOC leading to this publication has received funding from the EMPIR program co-financed by the participating states and the European Union's Horizon 2020 research and innovation program. The work is part of the Research Council of Finland Flagship Programme, Photonics Research and Innovation (PREIN), decision number 346529, Aalto University.

**References:**

1. Haapalinna, A. et al (1999). High-accuracy measurement of specular spectral reflectance and transmittance. *Analytica Chimica Acta*, *380*(2-3), 317-325.
2. Pourjamal, S. et al (2014). Characterization of thin-film thickness. *Metrologia*, *51*(6), S302-S308.
3. Danilenko, A. et al (2023). Characterization of PillarHall test chip structures using a reflectometry technique. *Measurement Science and Technology*, *34*(9), 094006.
4. Eichstädt, S. et al (2013). Comparison of the Richardson–Lucy method and a classical approach for spectrometer bandpass correction. *Metrologia*, *50*(2), 107-118.
5. Furman, S. A., & Tikhonravov, A. V. (1992). *Basics of optics of multilayer systems*. Atlantica Séguier Frontieres.
6. Wang, S. W. et al (2007). Concept of a high-resolution miniature spectrometer using an integrated filter array. *Optics Letters*, *32*(6), 632-634.

# Precision measurement of chromatic dispersion using a femtosecond-resolution pulse shaper and autocorrelator

Koyo Watanabe[1], Ryu Niigaki[1], Takashi Inoue[1], Hugo Thienpont[2] and Nathalie Vermeulen[2]

[1] *Hamamatsu Photonics K. K., Central Research Laboratory, Hirakuchi 5000, Hamana-ku, Hamamatsu City, Shizuoka, 434-8601, Japan*

[2] *Brussels Photonics (B-PHOT), Department of Applied Physics and Photonics (IR-TONA), Vrije Universiteit Brussel (VUB), Pleinlaan 2, 1050 Brussel, Belgium*

*Corresponding author: koyo.watanabe@crl.hpk.co.jp*

**Keywords:** chromatic dispersion measurement, time of flight, spatial light modulator

In the research on developing femtosecond-pulsed fiber laser sources, the chromatic dispersion of optical fibers is a particularly important physical parameter, significantly influencing the shape of the pulse waveform and its spectrum. With the diversification of fiber laser sources, shortening the fiber length is required to achieve precise pulse control and system miniaturization. However, conventional methods [1] for monitoring chromatic dispersion lack simplicity and sufficient sensitivity for millimeter-scale length optimization of such fibers, making it challenging to accurately determine chromatic dispersion. Therefore, we propose a novel, highly sensitive, and simple method for measuring chromatic dispersion.

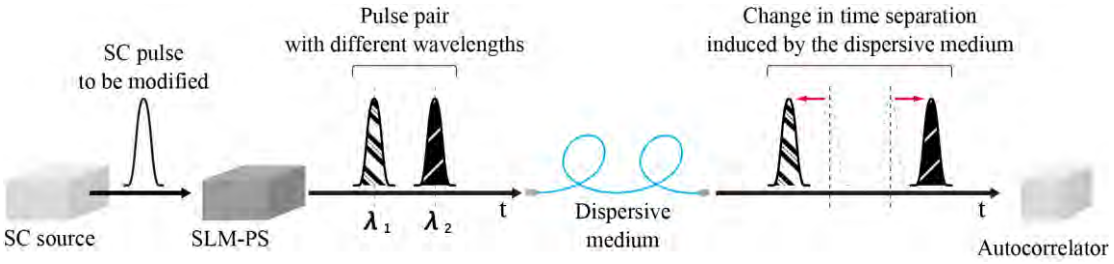


Fig. 1. Proposed system to measure the chromatic dispersion of a dispersive medium [2].

Figure 1 shows the schematic diagram of the proposed system for measuring chromatic dispersion in an optical fiber sample [2]. The system is based on time-of-flight measurements of femtosecond laser pulses travelling through the fiber. We have developed a femtosecond-resolution pulse shaping system that uses a spatial light modulator (SLM-PS) [3], allowing us to precisely control both the temporal waveform and spectrum of the incoming light beam [4,5]. This SLM-PS can split a single pulse from a supercontinuum (SC) source into two pulses with distinct center wavelengths. As the time separation between the pulses varies significantly when passing through dispersive materials, we propose using this phenomenon to measure chromatic dispersion by observing the relative changes in time separation. To achieve accurate measurements, we utilize a highly sensitive autocorrelator as the detector.

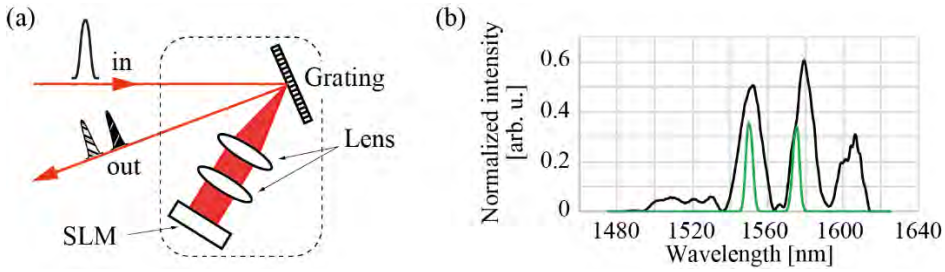


Fig. 2. (a) configuration of SLM-PS, and (b) example of SC source spectrum (black) and sliced Gaussian spectrum with SLM-PS (green).

The detailed configuration of the SLM-PS is shown in Fig. 2(a). It consists of a grating, a pair of cylindrical lenses, and an SLM. Using the SLM, we slice the incoming SC intensity spectrum into two Gaussian shapes, as shown in Fig.2 (b). Then we apply a different linear phase modulation to each Gaussian spectrum, splitting a single pulse into two temporally separated pulses with distinct center wavelength, as shown in Fig.3 (a)-(b).

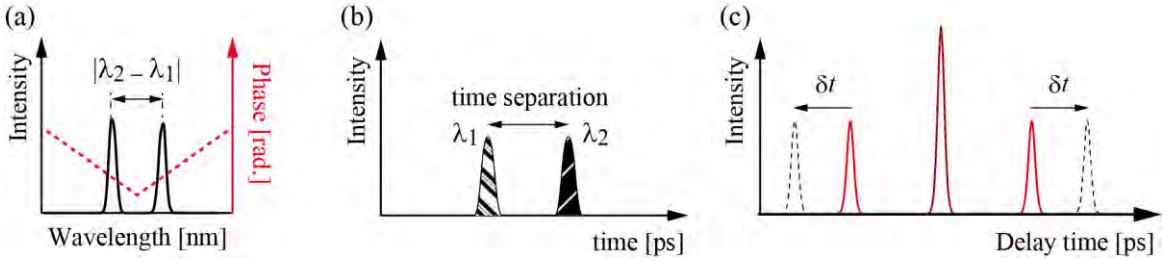


Fig. 3. (a) shows spectral intensity waveform and phase pattern to be applied with SLM. (b) temporal waveform, which corresponds to the spectral waveform shown in (a). (c) autocorrelation waveform of (b).

Figure 3(c) shows the autocorrelation waveform of (b). The change in time separation induced by the chromatic dispersion appears as $\delta t$ in the autocorrelation waveform. Based on equation (1), the chromatic dispersion (CD) can be calculated using $WS$ and $L_{fiber}$, which stand for wavelength separation, $|\lambda_2 - \lambda_1|$, and length of fiber, respectively.

$$CD\left[\frac{\text{ps}}{\text{nm km}}\right] = \frac{\delta t\ [\text{ps}]}{WS\ [\text{nm}] \times L_{fiber}[\text{km}]} \tag{1}$$

To demonstrate the measurement principle and its precision, we measured the change in time separation induced by optical fibers of type PM1550-XP. Figure 4(a) shows the change in time separation as a function of fiber length measured at 1565 nm. In the experiment, we set the wavelength separation as 25.4 nm. We confirmed that the change in time separation depends linearly on the fiber length, as expected from Equation (1). Chromatic dispersion of the fiber sample can be derived from the slope value, and it is shown in Fig.4(b), along with the reference values provided by the fiber vendor. The result shows good correspondence.

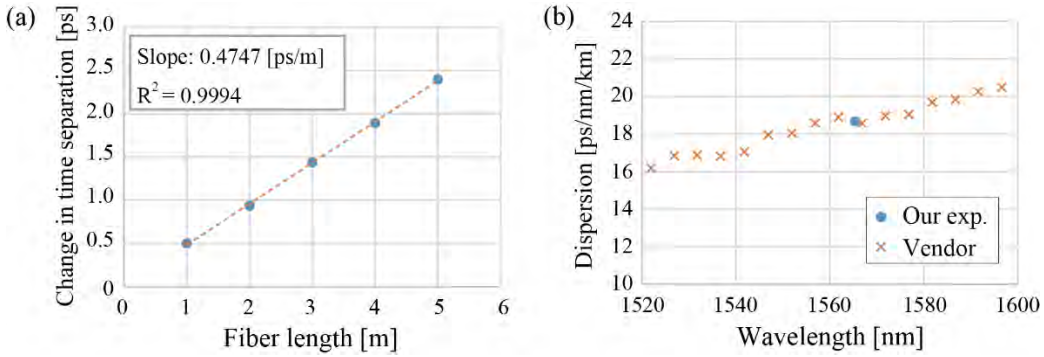


Fig. 4. (a) change in time separation as a function of fiber length measured at 1565nm. (b) measured dispersion data and comparison with the dispersion data provided by vendor.

Regarding measurement precision for the time separation, our experiments indicate that the measurement error in the proposed system is in the femtosecond range. If we assume the error is as 1 fs, the proposed dispersion characterization system has a capability of distinguishing the length of the fiber at the precision of ~ 2.1 mm.

In conclusion, our novel time-of-flight-based method for measuring chromatic dispersion in optical fibers using a spatial light modulator-based pulse shaping system (SLM-PS) has demonstrated high sensitivity and simplicity. This approach effectively addresses the limitations of conventional methods [1], particularly for short optical fibers. The experimental results show a strong correlation with reference values, confirming the accuracy and reliability of our system. With a measurement error in the femtosecond range, our method offers precise dispersion characterization of short optical fiber with the capability of distinguishing the length of typical fiber types at the precision of ~ 2.1 mm. Future work will focus on further refining the system and exploring its applications in various optical waveguide technologies.

**References**

1. Zong, Appl. Opt., 54(26), 7973 (2015).
2. K. Watanabe, K. Shigematsu, T. Inoue, U.S. Patent application No. US20220178752A1 (2022).
3. K. Watanabe, H. Takahashi, K. Shigematsu, N. Matsumoto, and T. Inoue, **31**, 236-241 (2024).
4. H. Takahashi, K. Watanabe, K. Shigematsu, T. Inoue, and H. Satozono, Opt. Lett., **46**, 1534-1537 (2021).
5. K. Watanabe, T. Inoue,Opt. Express, **28**, 1481 –14823 (2020).

# Spatial photonic Ising machine using a digital micromirror device

Yusuke Ogura, Takumi Sakabe, Suguru Shimomura, Hiroshi Yamashita, Hideyuki Suzuki, and Jun Tanida
*Graduate School of Information Science and Technology, Osaka University*
*Corresponding author: ogura@ist.osaka-u.ac.jp*

**Keywords:** Ising machine, DMD, spatial modulation, combinatorial optimization problem

## 1. Introduction

Many kinds of problems strongly related to people's daily life, including communication networks, commodity distribution, and drug development, are often formulated as a combinatorial optimization problem. Thus developing methods for efficiently solving such problems, in particular large-scale problems, at a high speed is an important issue. Ising machines are a dedicated hardware to find the ground state of an Ising model, which originates from the behavior of magnetic materials' spins, and they can be applied to solve combinatorial optimization problems. To date, Ising machines are realized using a variety of physical pseudo-spins, for example, appeared in trapped ions, CMOS circuits, and optical pulses[1]. Spatial modulation of light is also promising for realizing pseudo-spins, and Pierangeli firstly demonstrated a spatial photonic Ising machine (SPIM) in 2019 [2]. The features of the SPIMs include instant execution of sum-of-products operations, implementation of fully-connected Ising models, and high scalability in the number of spins. Some extensions and improvement of the primitive SPIM systems have been achieved [3,4]. We have also constructed a multi-component model to extend the classes of optimization problems that can be dealt with in the SPIM, and have demonstrated its validity with temporal or spatial multiplexing of light [5,6]. However, in the current SPIM systems, a liquid-crystal spatial light modulator (SLM) is generally employed to encode a spin distribution, and the frame rate of the SLM is a limiting factor of the system performance.

We here present implementation of an SPIM system using a digital micromirror device (DMD) instead of a liquid-crystal SLM. The potential frame rate of DMDs is over 30,000 Hz and this can contribute to improve the computing speed. On the other hand, the DMDs provide binary amplitude modulation alone, although the spins in the SPIM are encoded into phases. In this study, we investigated a method for controlling phase with DMDs, and demonstrate its usability in the SPIM system. Furthermore, the property of the system for different types of problems was examined because implementation suitable for the nature of given problems is important. Note that the SPIM is a good example of optical computing that shines in the realization of high-performance domain specific systems on the basis of the nature of light and recent progress of optical devices. The knowledge on the direction of implementation is helpful in full utilization of such potential.

## 2. Implementation

To control the phase distribution using a DMD, we consider a pair of adjacent micromirrors as a single pixel, and use the difference between optical path lengths of light waves reflected by individual micromirrors. With suitable configuration of the incident angle to the DMD, the phase 0 and $\pi$ can be given to these light waves. Consequently, switching only one of the two adjacent micromirrors ON makes it possible to express the phase required for the corresponding pixel.

The configuration of the experimental system is shown in Fig. 1. A unit-amplitude plane-wave light from a laser source is modulated to $\xi_j$ by an amplitude-type liquid-crystal SLM, where $j\ (= 1,2,\dots,N)$ denotes the pixel position and $N$ is the number of the pixels. Note that the amplitude distribution $\xi_j$ is fixed during computation because it is determined by the problem to be solved, and therefore this SLM does not affect the computing speed. The light just after the SLM is imaged on the DMD using lenses L2 and L3, and then modulated by a DMD with $\sigma_j = \exp\{i\pi\phi_j\} \in \{-1, 1\}$ where $\phi_j$ is the phase distribution and $\sigma_j$ is the $j$-th spin

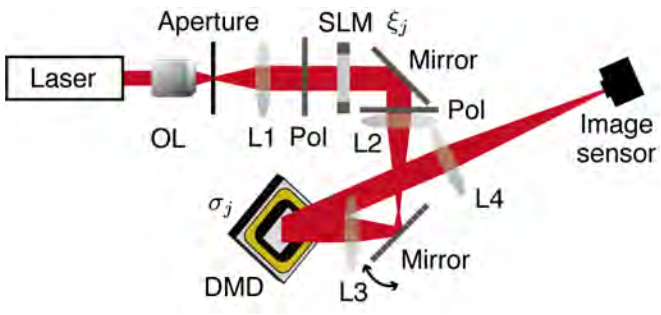


Fig. 1 Experimental setup. OL: objective lens; Pol: polarizer; L: lens; SLM: spatial light modulator (liquid-crystal, amplitude-type).

variable. The light is finally Fourier transformed by lens L4. The intensity at the center position on the image sensor corresponds to $H = A\sum_{j,k}\xi_j\xi_k\sigma_j\sigma_k$ , which is the Hamiltonian of the Ising model implemented by the system. Here $A$ is a constant. The Hamiltonian value is evaluated in each iteration, and the spin variables are updated based on the framework of simulated annealing.

## 3. Experiment

To test the feasibility, our system was examined with a number partitioning problem for 256 spins (Prob. #1). In the given problem, all elements in a multiset are set to be the same, so that the optimal solution is the case where the number of the variables with $\sigma_j = 1$ is 128. The result for 10 trials is shown in Fig. 2(a). You can see from the left graph that the obtained solution converges to approximately optimal ones with increasing the iteration. The Hamming distances between the obtained solutions and their nearest optimal solutions are 0 or no more than 4, which shows that our DMD-based system works as an SPIM.

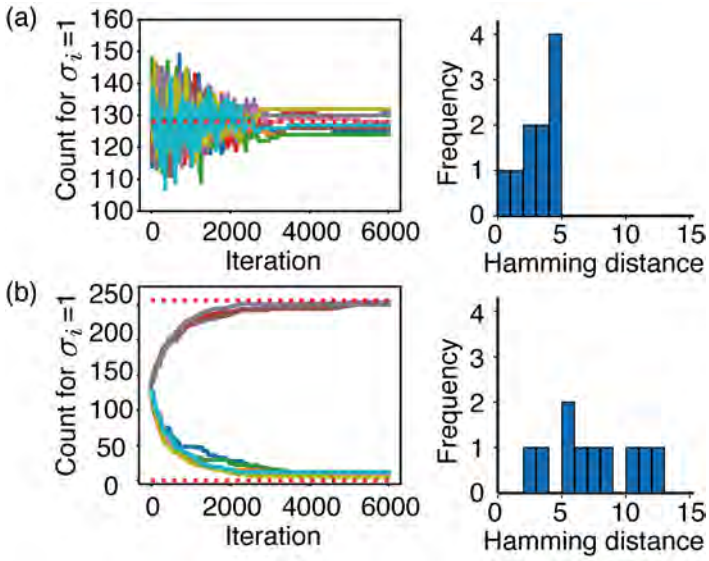


Fig. 2 Experimental results for (a) a number partitioning problem and (b) a problem searching the ground state under the strong magnetism. Left: Variations of obtained solutions on iteration. Different colors indicate different trials. Red dotted lines denote an optimal value. Right: Histogram of Hamming distance of the obtained solutions.

Next, to investigate a property of the system for the problem nature, we examined another kind of problem, a problem for searching the ground state under the strong magnetism (Prob. #2). In the optimal solution for this problem, all spin variables take the same value. Figure 2(b) shows the result for a 256-spin problem. The obtained solution approaches to either one of the two optimal solutions as with Prob. #1. This supports again the effectiveness of the system. On the other hand, the system could not find the optimal solution within 6,000 iterations in contrast to Prob. #1. We can find the difference between the processes for these problems; the central intensity on the image sensor is minimized through the iteration for Prob. #1, and it is maximized for Prob. #2. In case of maximization, the signal to noise ratio becomes higher when the obtained solution approaches to the optimal one, but a wide dynamic range is required for an image sensor. This suggests that the problem nature or the modeling methods can affect the performance of the SPIM, and an SPIM system should be designed with considering it.

## 4. Conclusions

In this study, an SPIM system with a DMD to encode spin variables is introduced. The experimental results demonstrate its effectiveness in finding the optimal solution for combinatorial optimization problems. We also found out that the physical property in the computing process can affect the system's performance. Future issues include demonstration of the high-speed computation capability of the DMD-based SPIM system.

**Acknowledgement**

This work was supported by JST-ALCA-Next Program Grant Number JPMJAN23F2, Japan.

**References**

1. N. Mohseni, P. L. McMahon, and T. Byrnes, Nat. Rev. Phys. **4**, 363–379 (2022).
2. D. Pierangeli, G. Marcucci, and C. Conti, Phys. Rev. Lett. **122**, 213902 (2019).
3. J. Ouyang, Y. Liao, Z. Ma, D. Kong, X. Feng, X. Zhang, X. Dong, K. Cui, F. Liu, W. Zhang, and Y. Huang, Commun. Phys. **7**, 168 (2024).
4. D. Pierangeli, G. Marcucci, D. Brunner, and C. Conti, Nanophotonics **9**, 4109-4116 (2020).
5. H. Yamashita, K. Okubo, S. Shimomura, Y. Ogura, J. Tanida, and H. Suzuki, Phys. Rev. Lett. **131**, 063801 (2023).
6. T. Sakabe, S. Shimomura, Y. Ogura, K. Okubo, H. Yamashita, H. Suzuki, and J. Tanida, Opt. Express **31**, 44127-44138 (2023).

# Down-sampling vibration-measurement technique based on a laser diode interferometry

Takamasa Suzuki, Samuel Choi, and Osami Sasaki
*Niigata University, Faculty of Engineering, 8050 ikarashi 2-nocho, Nishi-ku, Niigata, 950-2181 Japan*
*Corresponding author:takamasa@eng.niigata-u.ac.jp*

**Keywords:** vibration-measurement, laser diode, interferometry, down-sampling

Optical interferometry is useful for the precise measurement of the surface profile or vibration of an object. This technique is advantageous because it performs noncontact measurements and does not affect the vibrations to be measured.
Several types of vibration sensors can easily measure high-speed vibrations [1, 2]. In some fields, such as process control in industrial applications, vibration analysis in biological engineering, and vibration-mode analysis in acoustic engineering, the measurement of two-dimensional (2D) vibrations over a wide field of view is required. In this case, a high-speed video camera is required to measure the high-frequency vibrations of the object. The problem with this method is that such a video camera is extremely expensive. Another technique using heterodyne signal processing has been proposed; however, it can only be adapted to measure a single vibration frequency [3].
In this study, we introduced precise vibration measurement techniques based on laser diode interferometers using video cameras. This technique combines phase-shifting interferometry (PSI) and a down-sampling technique (DST). High-precision 2D vibration sensing can be performed using a budget video camera as the detector. Harmonic vibrations are observed.
The DST is used to recover high-frequency periodical signals using a sampling pulse, which has a frequency much lower than that of the target signal. The vibrations are calculated using the signal obtained through the DST.
The relationship between the target signal and the sampling pulse for the DST is given by

$$\frac{1}{f_s}-\frac{m}{f}=T_s-mT=\Delta t\,, \qquad (1)$$

where $f$, $f_s$, $T_s$, $T$, $m$, and $\Delta t$ are the vibration frequency, sampling frequency, sampling period, vibration period, number of delay periods, and delay time, respectively. This relationship is illustrated in Fig. 1. In this case, m is 1, and sampling is performed once during the period of the target signal. The original signal was expanded along the time axis and recovered by tracing the sampled data. The number of samples in one period is given by

$$N=\frac{T}{\Delta t}=\frac{1}{\Delta t\cdot f}\,. \qquad (2)$$

The enlargement ratio K is defined by

$$K=mN=m\frac{T}{\Delta t}=\frac{m}{\Delta t\cdot f}\,. \qquad (3)$$

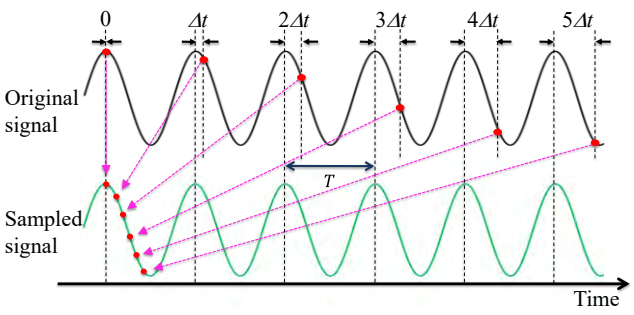


Fig. 1. Schematic of down-sampling technique.

The setup is illustrated in Fig. 2, where the stepwise modulation signal $I_m(t)$, shutter pulse, and sampling signal for the A/D converter are generated by the timing controller. The LD oscillated at a center wavelength of 658 nm at an output power of 80 mW. A piezoelectric transducer (PZT) was attached to the object mirror, and it was vibrated sinusoidally with the frequency of 500 Hz at the vibrating amplitudes of 329 $nm_{p\text{-}p}$ ($\lambda_0/2$). The timing controller controlled the phase-shift current and shutter timing of the

CCD camera. As we set Δt=100 μs and m=10, K was set to 200. The CCD camera captures images at a frame rate of 50 fps. The effective image size and pixel size were 640 × 480 pixels and 5.6 × 5.6 μm$^2$, respectively.

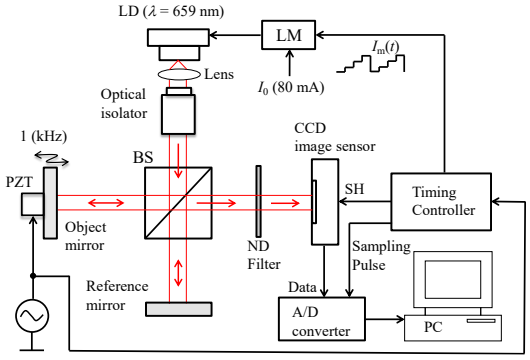


Fig. 2. Setup of PSI using DST.

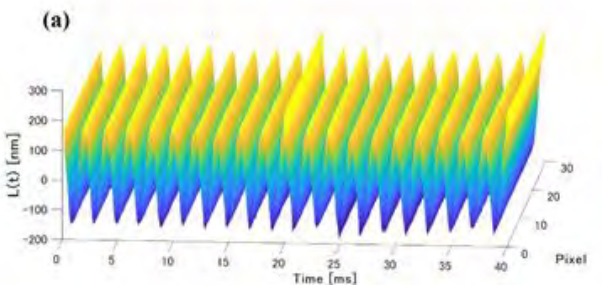


Fig. 3. Vibration distribution measured with DST.

The measured 2D vibration distributions are shown in Fig. 3. The average amplitude during these four periods was 156 nm. The measurement error was 8.5 nm compared with an amplitude of 164.5 nm ($\lambda_0/4$), which was estimated from the phase change in the interference signal. The vibration distribution can be measured using the system shown in Fig. 2. However, preliminary information regarding the vibration frequency is required. To overcome this limitation, we propose the system illustrated in Fig. 4. It is equipped with a frequency detection system and a frequency multiplier consisting of a phase-locked loop (PLL).

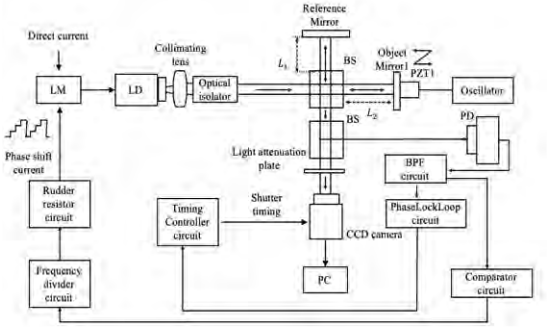


Fig. 4. Setup of PSI using DST with a PLL.

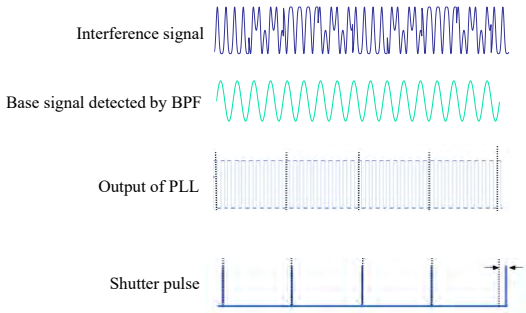


Fig. 5. Generation of a shutter pulse.

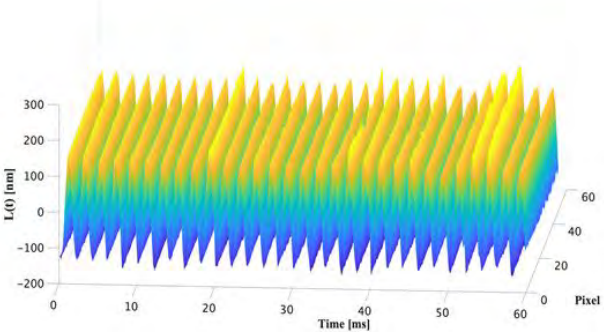


Fig. 6. Vibration distribution measured with the PLL.

A schematic of the shutter pulse generation is shown in Fig. 5. The fundamental signal was extracted from the interference signal using a bandpass filter (BPF). This signal was fed to the PLL, and frequency multiplication was realized. After the fourth sampling, we delayed the shutter pulse to only one cycle of the PLL output. The pulse count and delay were measured using a microprocessor. We measured 2D vibrations under the same conditions as those in the above experiment. The results are shown in Fig. 6. The average amplitude was 151.4 nm. The measurement error was estimated to be 13.1 nm compared with the amplitude of 164.5 nm ($\lambda_0/4$).

In conclusion, precise vibration measurement techniques that use down-sampling PSI were introduced. They can measure the high-frequency vibration distribution at a low frame rate using a budget camera.

**References**

1. T. Suzuki, O. Sasaki, K. Higuchi, and T. Maruyama, Applied Optics, **28**, 5270-5274 (1989).
2. B. K. A. Ngoi, K. Venkatakrishnan, B. Tan, N. Noel, Z.W. Shen, and C.S. Chin, Opt Commun., **182**, 175-185 (2000).
3. S. Choi, Y. Maruyama, T, Suzuki, F. Nin, H. Hibino, Opt. Commun., **356**, 343-349 (2015).

# Development of body surface vibration meter using speckle shearing interferometer

Ryohei Hanayama[1], Neisei Hayashi[1] and Katsuhiro Ishii[1]

[1] *The Graduate School for the Creation of New Photonics Industries (GPI), Hamamatsu*

*Corresponding author: hanayama@gpi.ac.jp*

**Keywords:** speckle interferometry, shearing interferometry, vibration measurement, human skin

We developed a body surface vibration meter using speckle shearing interferometer for non-contact pulse wave measurement. We focused on the volume pulse, or plethysmogram, that is used to diagnose diseases of blood vessel. It can be observed as the motion of skin surface. It can be thought that the vibration of skin surface shows the condition of human body. Moreover the developed device could potentially be used for non-contact medical diagnosis as an alternative to palpation. In this presentation we will introdue the develped device and some experimetnal results.

A photograph of the developed body surface vibrometer is shown in Fig. 1. This device is designed primarily for measuring pulse waves at the wrist. The person being measured inserts their wrist into the space at the bottom of the device (Fig. 2). The white box at the top is equipped with an illumination unit that irradiates the target with laser light and an interferometer unit. The optical system of the interferometer is based on the twyman-green interferometer. The mirror of one arm of the interferometer is slightly tilted from the optical axis, to realize the shearing interferometer. Then, the two reflected beams are slightly sheared each other on the imaging plane of the camera. Therefore, the inclination of the target can be measured. The opitcal system of the interferometer part is shown in Fig. 2. This interferometer consists of only one cube prism for mechanical stability. There is 0.2deg. of angle difference between the two of beams, because there is 0.1deg. of inclination in one face of the prism. The angle difference leads the image shearing. The shear amount depends on the distance from the interferometer to the object plane. When the working distance is 150mm, the shear amount is 0.5mm. The speckle interferograms are acquired using a high-speed camera with a spatial resolution of 1440 × 1080 pixels at a frame rate of up to 227 fps.

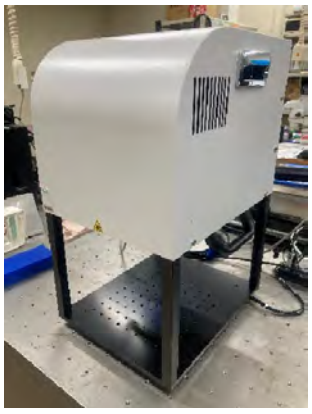

Fig.1 Developped body surface vibrometer

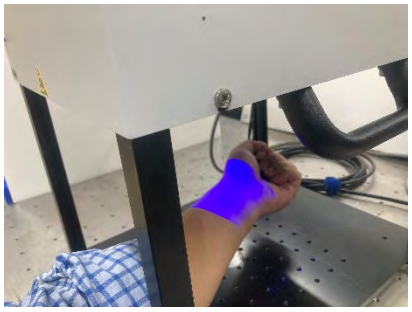

Fig.2 Measurement Scene

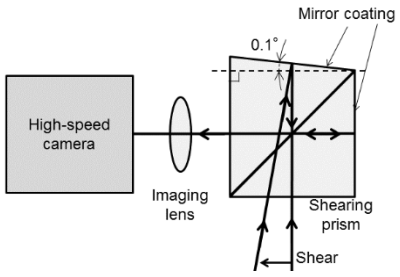


Fig.3 Schematic diagram of interferometer unit

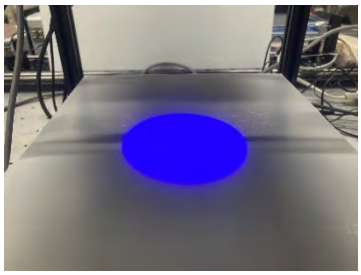

Fig. 4 Illumination beam

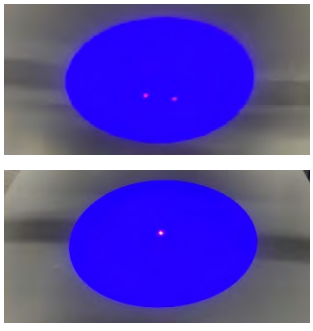

Fig. 5 Guide laser

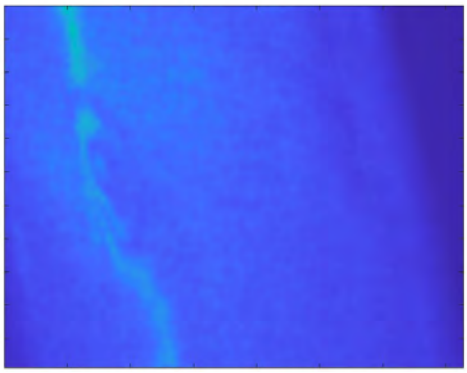

Fig.6 acquired interference fringe

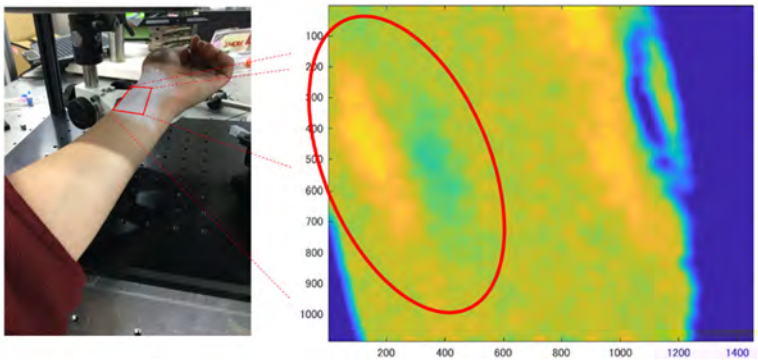


Fig.7 measurement result for wrist

The illuminating laser beam is emitted from the laser head and is diverged to a circular area with a diameter of 70 mm at the measurement point. The beam is well homogenized by a uniquely designed aspheric lens (Fig. 4). The beam is well homoginaized by designed aspherical lens. The wavelength is 445nm. Since we want to measure surface shapes, we use short wavelengths that are less likely to penetrate the skin. It also has a guide laser to help place the target in the correct position - where the two guide laser beams intersect is the correct position (Fig. 5).

Figs. 6 and 7 show some preliminaly experimental results. Fig. 6 shows the acquired interference fringe. The fringe pattern appeared on the skin over the artery in wrist. The fringe pattern shows a height difference of about seberal numbers of wavelength. As mentioned above, the maximum frame rate of the camera installed in this device is 227 fps. Therefore, it is possible to observe minute vibrations of human skin. Fig. 7 shows the results of the analysis using a different approach. That is based on the optical flow of speckle interferograms. By using this method, it can be succeeded to measure the velocity of pulse wave[1].

We are currently verifying these results and working to establish a method for measuring micro-vibrations on the skin surface.

**References**

1. N. Hayashi, R. Hanayama, and K. Ishii, *Proc. of SPIE* **12622**, 1262211 (2023).

## *Session 5: Photonics fundamentals*

## Wednesday Jan 8, 2025

10:40-11:00 Takeshi Yasui: Photonic 6G wireless communication
11:00-11:20 Ari T. Friberg: Self-evolving vector Bessel beams
11:20-11:40 Kuroo Nami: Parameter exploration in the framework of volumetric beam shaping
11:40-12:00 Kazuki Yamanouchi: Three-dimensional imaging through scattering media by constructing a digital twin based on Gaussian Splatting
12:00-12:20 Yoshio Hayasaki: Spatial and temporal stabilization in holographic beam shaping for industrial use

# Photonic 6G wireless communication

Takeshi Yasui
*Institute of Post-LED Photonics (pLED), Tokushima University, Tokushima, Japan*
*Corresponding author:* yasui.takeshi@tokushima-u.ac.jp https://femto.me.tokushima-u.ac.jp/eng/

**Keywords:** optical comb, microcomb, terahertz, wireless communication, 6G

## 1. Introduction

Terahertz (THz) waves are expected to serve as carrier waves for next-generation mobile wireless communication (6G, expected carrier frequency > 300 GHz), enabling much higher data rates compared to current wireless communication (5G, carrier frequency = 28 GHz or more) [1]. In particular, frequencies above 350 GHz have garnered attention for wireless mobile fronthaul and backhaul in 6G, offering higher data rates and avoiding interference with other 6G wireless applications. The main limitation for 6G is the performance of THz emitters. While electronic THz emitters based on frequency multiplication have been effective for 5G, 6G's higher carrier frequencies present technical challenges, including increased phase noise from higher-order frequency multiplication and power consumption.

Photonic technology can help mitigate these problems [2]. A key component is the optical frequency comb (OFC), with inherently stable frequency spacing ($f_{rep}$) and low phase noise due to mode-locking. Recently, a compact, cost-effective on-chip Kerr micro-resonator comb (namely, microcomb), has emerged [3]. Its small size enables $f_{rep}$ to increase to 6G carrier frequencies above 300 GHz. Two adjacent OFC modes from the stable soliton microcomb can be directly used for photomixing, producing a low-phase-noise THz wave without the need for optical frequency multiplication [4]; it further utilizes wireless THz communication [5,6].

In this paper, we injection-lock two distributed feedback laser diodes (DFBs) to adjacent modes of a 560-GHz-spacing soliton microcomb. The resulting low-phase-noise, high-OSNR DFB outputs were used to generate THz waves via photomixing with a uni-traveling carrier photodiode (UTC-PD). We demonstrate near error-free OOK wireless data transmission in the 560-GHz band using an SBD for detection, and we evaluate signal quality with BPSK, QPSK, and 16QAM modulation formats.

## 2. Experimental setup

Figure 1 illustrates the experimental setup. A 560-GHz-spacing0 1550-nm soliton microcomb was generated using a $Si_3N_4$ ring resonator (FSR = 560 GHz). The microcomb was split using a fiber coupler (FC2), with each half filtered to extract modes at 1551.6 nm (μOFC-M1) and 1547.2 nm (μOFC-M2). These modes were injected into distributed feedback lasers (DFB1, 193.2 THz; DFB2, 193.7 THz) as master lasers for optical injection locking (OIL).

OIL-DFB1 (unmodulated) and OIL-DFB2 (modulated by a $LiNbO_3$ intensity modulator) were combined and amplified by an EDFA (total power = 30 mW). The output was fed into an antenna-integrated UTC-PD to generate THz waves, which were detected by a Schottky barrier diode (SBD). The resulting signal was amplified and measured by a real-time oscilloscope. In BPSK, QPSK, and 16QAM, the oscilloscope demodulated the signal by accounting for the intermediate frequency ($f_{IF}$).

## 3. Results

We generated OOK-modulated THz waves by using an optical modulator on one of the two modes of soliton microcomb, while leaving the other mode unmodulated. These modulated THz waves were then directed into a UTC-PD. After propagating through free space, we detected the OOK-modulated THz waves using a SBD and measured their time waveform using a real-time oscilloscope. The bit rate for OOK data transmission was set at 1 Gbit/s. Figure 2(a) shows the measured eye diagram of the OOK signal, indicating that the eye is fully open. The calculated Q-value (=6.23) from this eye diagram is close to the error-free limit (Q-value = 6.36), achieving nearly error-free 1 Gbit/s OOK data transmission in the 560 GHz band.

Next, we evaluated the quality of data transmission using advanced modulation formats based on phase and amplitude for a carrier frequency of 560 GHz. Figures 2(b) and 2(c) show the constellation diagrams for 1 GBaud BPSK data transmission and QPSK data transmission ($f_{IF}$ = 5 GHz), with red and blue representing

symbols and their transitions. In both cases, isolated symbols are clearly visible. The rms EVM (Root Mean Square Error Vector Magnitude) for BPSK is 23.9%, and for QPSK, it is 23.6%, corresponding to BER values of $10^{-9}$ and $10^{-5}$, respectively. In either case, the BER values are below the FEC limit, ensuring error-free operation with standard FEC techniques. Figure 2(d) shows the constellation diagram for 16QAM data transmission at 0.1 GBaud ($f_{IF}$ = 5 GHz), with 16 isolated symbols clearly visible. The corresponding EVM is 8.07%, which is below the EVM limit of 15.8% set by IEEE 802.15.3d.

This research and development work was supported by the MIC/FORWARD # JPMI240910001.

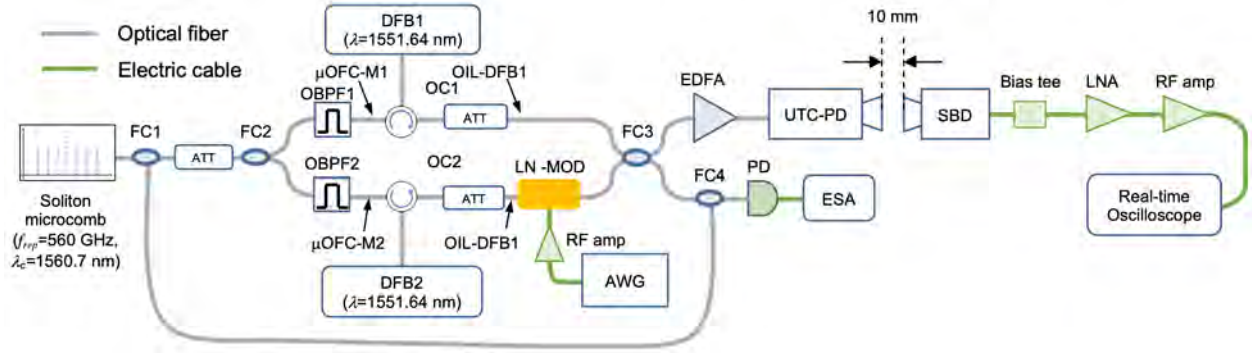


Fig. 1. Experimental setup.

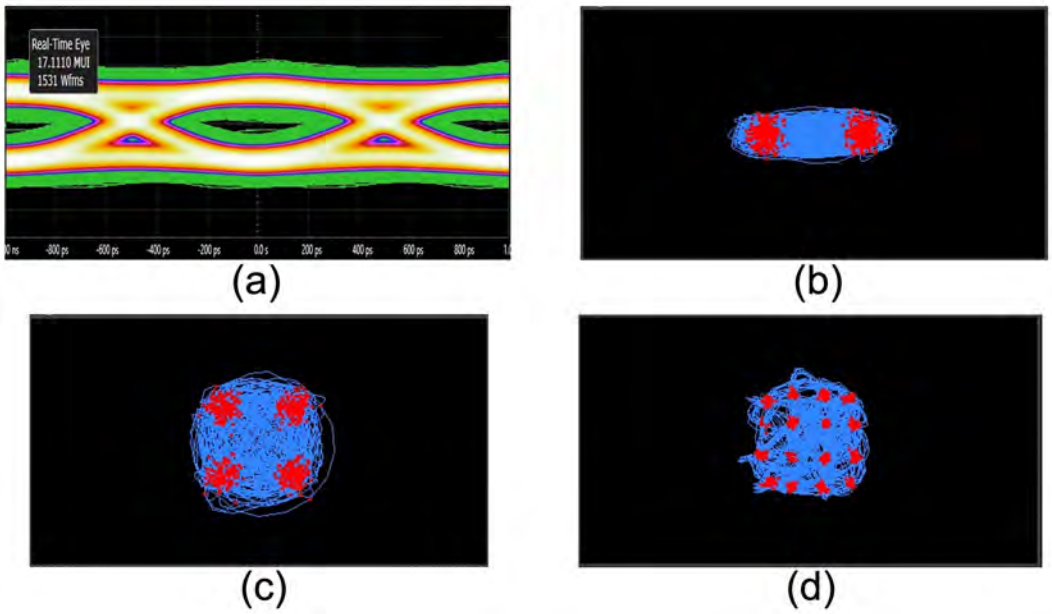


Fig. 2. Experimental results.

**References**

1. S. Dang *et al.*, *Nature Electron.* **3**, 20-29 (2020).
2. T. Nagatsuma *et al.*, *Nature Photon.* **10**, 371-379 (2016).
3. B. Shen *et al.*, *Nature* **582**, 365–369 (2020).
4. N. Kuse *et al.*, *Commun. Phys.* **5**, 312 (2022).
5. Y. Tokizane *et al.*, *Opt. Continuum* **2**, 1267-1275 (2023).
6. Y. Tokizane *et al.*, *Opt. Continuum* **3**, 1-8 (2024).

# Self-evolving vector Bessel beams

Jiaqi Yang, Tommi K. Hakala and Ari T. Friberg
*Center for Photonics Sciences, University of Eastern Finland, P. O. Box 111, FI-80101 Joensuu, Finland*
*Corresponding author: ari.friberg@uef.fi*

**Keywords:** Bessel beam, geometric phase, spin and orbital angular momentum, metasurface

Vector Bessel beams (VBBs) are diffraction-free, directional light waves of spatially inhomogeneous polarization states and Bessel-type transversal intensity profiles. They may exhibit a geometric Pancharatnam–Berry phase along the beam, possess spin angular momentum (SAM) depending on the chirality of circular polarization, and carry orbital angular momentum (OAM) owing to the spiral phase structure of the wave front. Beams of this type have recently attracted interest due to their creation by metasurfaces, their versatility, and potential applications in laser science, optical manipulation, and communication.

To describe the vector nature of VBBs, or vector vortex beams more generally, a useful representation called the higher-order Poincaré sphere (HOPS) has been introduced [1]. At the poles the $l$th-order HOPS has uniform orthogonal circular polarization states with beam phase patterns $e^{\pm il\varphi}$ ($\varphi$ is the azimuthal angle), while the other points correspond to different elliptical and linear polarizations. Beams characterized by HOPS thus carry both SAM and OAM. Through numerical simulations we have demonstrated an efficient method by which VBBs can be controllably generated simply with a single all-dielectric metasurface [2]. Specifically, by proper choices of the input polarization and the propagation distance from the metasurface, all points of the entire HOPS of any topological charge can be covered.

The spatial Fourier transform of a VBB yields a perfect vector beam (PVB) [3]. Such beams have the important feature that their transversal field profiles constitute sharp rings whose radii are independent of the topological charge, thus providing stable polarization states while maintaining high beam quality. We have analyzed the properties of dual perfect vector vortex beams implemented by means of vortex Dammann gratings [4].

Metasurfaces, made of nanoscale optical scatterers (see Figure 1), can arbitrarily tailor the phase, polarization state, and amplitude of light. Employing a single all-dielectric metasurface, we have demonstrated numerically a method for generating arbitrary VBBs and PVBs to cover the entire HOPS (see Figure 2).

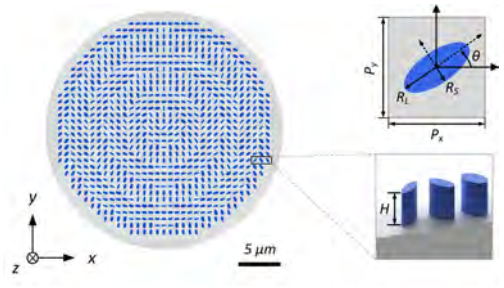


Figure 1: Schematic illustration of a metasurface. Elliptical nanorods of height $H$ and different radii $R_L, R_S$ and orientation $\theta$ in a regular matrix constitute an efficient and flexible platform [2].

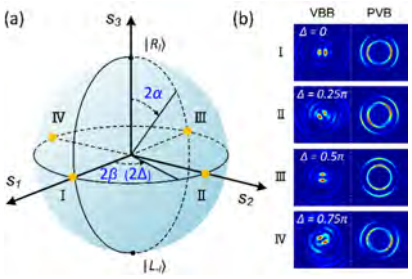


Figure 2: (a) Schematic illustration of HOPS. (b) The ensuing VBB and PVB intensity profiles for the case $l = 1$ at selected HOPS points (passing a horizontal polarizer) [4].

In general, each VBB on HOPS can be expressed as a superposition of right circular polarized (RCP, $|R\rangle$) and left circular polarized (LCP, $|L\rangle$) Bessel beams of opposite topological charges $\pm l$ [2]

$$\mathbf{E}(\rho, \varphi, z) \propto J_l(k_r \rho) \left\{ \cos\alpha e^{i\Delta(z)} e^{il\varphi} |R\rangle + \sin\alpha e^{-i\Delta(z)} e^{-il\varphi} |L\rangle \right\}, \tag{1}$$

where $\alpha$ and $\Delta(z)$ specify the spherical coordinates on HOPS, as shown in Figure 2(a). The metasurface, incorporating two different axicons, introduces (besides the spiral phases) an axial phase difference of $2\Delta(z)$ between the RCP and LCP components, while on the input side the phase difference is $2\beta$.

The focus in this work, however, lies on the basic properties and control of self-evolving vector Bessel beams. We analyze two types of self-evolving VBBs generated by a metasurface: one is an exact (paraxial) solution and the other a simplified representation, given by Eq. (1) above. In it, the axicon effects on the amplitudes of both circular polarization components are equal. It is shown (for both solutions) that when the electric field has traveled a distance $z_P$ satisfying $\Delta(z_P) = \pm\pi$, the polarization state has evolved to be identical with that at the metasurface plane [5]. Hence, $z_P$ is the field's propagation length for one polarization period.

We introduce a longitudinal Pancharatnam–Berry phase associated with the periodic polarization evolution and evaluate the orbital and spin angular momenta corresponding to the input beam and the metasurface.

As the field advances a distance $z_P$ parallel to the $z$ axis, the Poincaré vector evolves around a closed circular trajectory on the Poincaré sphere. The associated Pancharatnam–Berry phase [6, 7] is $\Phi_{\text{PB}}^{(e,s)} = \Phi_{\text{total}}^{(e,s)} - \Phi_{\text{dyn}}^{(e,s)}$, where the accumulated total and dynamic phases [8] are

$$\Phi_{\text{total}}^{(e,s)} = \arg[\mathbf{E}^*(\rho,\varphi,0)\cdot\mathbf{E}(\rho,\varphi,z_P)], \qquad \Phi_{\text{dyn}}^{(e,s)} = \text{Im}\int_0^{z_P} \frac{\mathbf{E}^*(\rho,\varphi,z)\cdot(\partial/\partial z)\mathbf{E}(\rho,\varphi,z)}{|\mathbf{E}(\rho,\varphi,z)|^2}dz. \tag{2}$$

Here $\arg$ denotes the phase, Im stands for the imaginary part, and the superscripts $(e,s)$ refer to the exact and simplified solutions, respectively. For the simplified case we find

$$\Phi_{\text{PB}}^{(s)} = \pm\Delta(z_P) - \Delta(z_P)\cos 2\alpha, \tag{3}$$

and for all self-evolving VBB solutions the magnitude of the Pancharatnam–Berry phase gradually grows from zero with increasing $2\alpha$ and abruptly changes sign at $2\alpha \approx 0.5\pi$ [5]. Therefore, we may conclude that the metasurface enables controlling the propagation-induced Pancharatnam–Berry phase of VBBs over the entire range from $-\pi$ to $\pi$ simply by tailoring the polarization state of the input field.

Making use of the fact that the linear momentum density of an electromagnetic wave field is proportional to the time-averaged Poynting vector, we consider the angular momentum associated with self-evolving VBBs and investigate the $z$ components of the total orbital ($J_{\text{orb}}^z$, vortex) and spin ($J_{\text{sp}}^z$, polarization) angular momentum within a polarization period. We show that for all VBBs and for all incident polarization states $J_{\text{orb}}^z = -nJ_{\text{sp}}^z$, where $n$ is the beam's charge [5]. Normalizing the angular momenta by the total energy $U$, in the simplified limit we find explicitly that $J_{\text{total}}^z/U = (J_{\text{orb}}^z + J_{\text{sp}}^z)/U = [(n-1)/\omega]\cos 2\alpha$, where $\omega$ is the angular frequency. For the normalized Pancharatnam–Berry phase and normalized total angular momentum it follows that [5]

$$\Phi_{\text{PB}}^{(s)'} = \Phi_{\text{PB}}^{(s)}/\Delta(z_P) = \pm 1 - \cos 2\alpha, \qquad J_{\text{total}}^{z'} = [\omega/(n-1)]J_{\text{total}}^z/U = \cos 2\alpha. \tag{4}$$

This indicates that for self-evolving VBBs the geometric phase and the total angular momentum are intimately connected. In this limit the sum of their normalized values clearly becomes a conserved quantity, i.e.,

$$\Sigma = \Phi_{\text{PB}}^{(s)'} + J_{\text{total}}^{z'} = \pm 1. \tag{5}$$

In conclusion, in this work we have investigated beam-like self-evolving VBBs created by metasurfaces and introduced a novel longitudinal Pancharatnam–Berry geometric phase. Further, we have shown that the orbital and spin angular momenta are closely related to the Pancharatnam–Berry phase and that they can be continuously tuned just by adjusting the incident polarization state. In the simplified limit the sum of their normalized values becomes a conserved quantity.

Funding: Research Council of Finland (project 359450 and PREIN Flagship 346518).

## References

1. G. Milione, H. I. Sztul, D. A. Nolan, and R. R. Alfano, *Physical Review Letters* **107**, 053601 (2011).
2. J. Yang, T. K. Hakala, and A. T. Friberg, *Physical Review A* **106**, 023520 (2022).
3. A. S. Ostrovsky, C. Rickenstorff-Parrao, and V. Arrizón, *Optics Letters* **38**, 534–536 (2013).
4. J. Yang, T. K. Hakala, and A. T. Friberg, *Optics Express* **32**, 20242–20255 (2024).
5. J. Yang, T. K. Hakala, and A. T. Friberg, submitted (2024).
6. S. Pancharatnam, *Proceedings of the Indian Academy of Sciences A* **44**, 247–262 (1956).
7. M. V. Berry, *Journal of Modern Optics* **34**, 1401–1407 (1987).
8. N. Mukunda and R. Simon, *Annals of Physics* **228**, 205–268 (1993).

# Parameter exploration in the framework of volumetric beam shaping

Kuroo Nami and Yoshio Hayasaki
*Center for Optical Research and Education (CORE), Utsunomiya University 7-1-2 Yoyo Utsunomiya, 321-8585 Japan*
*Corresponding author: kuroo_n@opt.utsunomiya-u.ac.jp*

**Keywords:** volumetric beam, computer-generated hologram, spatial light modulator

Laser processing has been increasingly required to be more sophisticated and complex, such as processing under tight constraints and complex geometries while meeting quality and throughput requirements [1, 2]. Therefore, only changes in the intensity and diameter of the Gaussian beam and the beam irradiation method are insufficient to optimize the processing. To meet industry demands, laser processing is performed using various beam shapes. In addition to two-dimensional beam shaping such as special focusing patterns and multiple beam generation, three-dimensional beam shaping (volumetric beam shaping) [3] that controls intensity in the optical axis direction at the same time is being realized. Volumetric beams are particularly effective for functional processing, as required by industry. A volumetric beam design framework has been established [4]. It is shaped using computer-generated holograms (CGH) displayed on a liquid-crystal spatial light modulator (LCSLM). The CGH is optimized using the weighted Gerchberg-Saxton (WGS) method [5, 6]. However, beam shaping demonstrated by using the framework is only for basic shapes such as three-dimensional arrayed focused beams and on-axis beams. Therefore, we investigate the properties of the parameters and better shaping methods in the framework to evolve to be more universal and to enable advanced shaping.

The volumetric beam needs to be shaped in the reconstruction space where the region of the reconstructive limit of the beam. If shaping is performed outside the region, poor shaping and unexpected errors will occur. We first investigate the space in the optical axis direction. The beam parameters and the system parameters in this analysis were values commonly used in laser processing. The laser beam has a wavelength of $\lambda$ = 1030 nm. The size of CGH is 12.8 × 12.8 mm. A circular aperture with a radius of $r$ = 6.4 mm is placed on the SLM. The focal length of the lens is $f$ = 155 mm. The focused beam intensity was investigated while changing the power of CGH $P_{\mathrm{CGH}}$. Figure 1 shows the change in the intensity ratio to the intensity without CGH at the focal point as the power of CGH is varied. The dependence on the input beam and the number of pixels $N$ was also confirmed. The circles, squares, and crosses indicate the intensity ratio under N = 512, N = 1024, and N = 4096. The red region is the range where the maximum spatial frequency of CGH does not exceed the spatial frequency of the display device. The CGH pattern for reconstructing the focused beam is more detailed as the power increases and as it nears the edge. The intensity ratio decreases as one goes outside of the red region in this result. Since the effective focal length of the optics is kept constant, the $NA$ is invariant. The intensity distribution is unchanged even if the focusing position is shifted in the axial direction. Therefore, this ratio should be 1.0, independent of CGH power ideally. This is considered to be because the patterns of the CGH are no longer correctly represented. The flat beam has more intensity distributed around the edge of the CGH, so the intensity ratio decreases more. It is considered that this region indicates an index of reconstruction space.

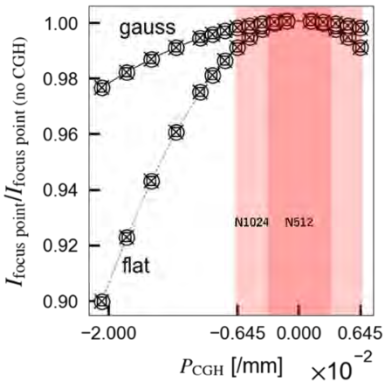

Fig. 1. Intensity ratio to the intensity without CGH at the focal point. The circles, squares, and crosses indicate the intensity ratio under $N = 512$, $N = 1024$, and $N = 4096$. The red regions indicate an index obtained from the spatial resolution of CGH.

Some examples of volumetric beam shaping within the reconstruction space are shown. The input beam is a Gaussian beam with a diameter of 3.0 mm. The SLM has a pixel number of $Nx = Ny = 1024$ and the pixel size is $px = py = 12.5$ μm. A circular aperture with a radius of $r = 5.76$ mm is placed on the SLM. The pixel size of the reconstruction plane is $\Delta x = \Delta y = 12.5$ μm. The values of the other parameters are as described above. Figure 2 (a) shows the focused beam intensity distribution without CGH for comparison. Figure 2 (b) shows a long-focused beam. The beam length $L$ is 10 times half of the focusing length $L_{\mathrm{FWHM}}$ (the full width at half-maximum of the laser beam profile in the axial direction). Figure 2 (c) shows a parallel long focused beam ($L$=4$L_{\mathrm{FWHM}}$). Figure 2 (d) shows multiple long focused beams. The beam lengths are 4$L_{\mathrm{FWHM}}$ and 5$L_{\mathrm{FWHM}}$, respectively. We succeeded in shaping a long focused beam with a continuous intensity distribution. The length can be changed arbitrarily. Throughput is increased and the structure is able to withstand tight structural constraints. Succeeded in shaping multiple beams in axial and trans-verse directions. Complex geometries can be processed.

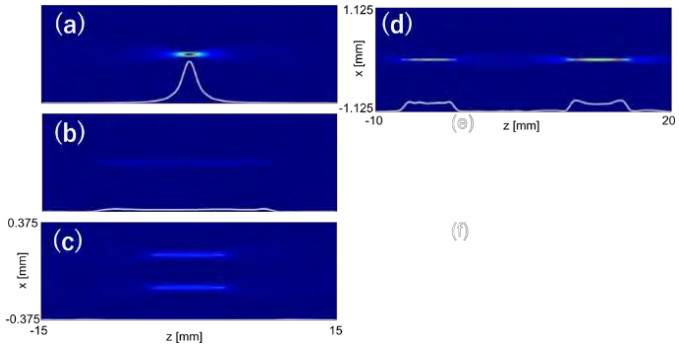


Fig. 2 Longitudinal cross sections of the intensity distribution of (a) the ordinary focused beam made in the optical system without CGH, (b) the long-focused beam with 10$L_{\mathrm{FWHM}}$, (c) parallel long-focused beams with 4$L_{\mathrm{FWHM}}$, and (d) multiple long-focused beams with 4$L_{\mathrm{FWHM}}$ and 5$L_{\mathrm{FWHM}}$.

We investigated the reconstruction space where the region of the reconstructive limit of the beam. This is one of the components of the volumetric beam shaping framework. The index for the optical axis reconstruction space is the range in which the maximum spatial frequency of the CGH does not exceed the spatial frequency of the display device. Long focused beams, parallel long focused beams, and multiple long focused beams were shaped within the reconstruction space. By shaping an arbitrary number of beams of arbitrary length with continuous intensity in the axial direction, functional processing with high throughput can be achieved.

**References**


1. H. Varel, D. Ashkenasi, A. Rosenfeld, M. Wahmer, and E. E. B. Campbell, "Micromachining of quartz with ultrashort laser pulses," Appl. Phys., A Mater. Sci. Process. **65**, 367–373 (1997).
2. R. R. Gattass, and E. Mazur, "Femtosecond laser micromachining in transparent materials," Nat. Photonics 2, 219–225 (2008).
3. H. Zhang, S. Hasegawa, H. Toyoda, and Y. Hayasaki, "Three-dimensional holographic parallel focusing with feedback control for femtosecond laser processing," Opt. Lasers Eng. **151**, 106884 (2022).
4. N. Kuroo and Y. Hayasaki, "Design framework of a computer-generated hologram that performs volumetric beam shaping for advanced laser processing," Opt. Continuum **3**, 1244-1253 (2024).
5. R. Di Leonardo, F. Ianni and G. Ruocco, "Computer generation of optimal holograms for optical trap arrays," Opt. Express **15**, 1913–1922 (2007).
6. Y. Zhao, L. Cao, H. Zhang, D. Kong, and G. Jin, "Accurate calculation of computer-generated holograms using angular spectrum layer-orient method," Opt. Express **23**, 25440–25449 (2015).

# Three-dimensional imaging through scattering media by constructing a digital twin based on Gaussian Splatting

Kazuki Yamanouchi, Suguru Shimomura and Jun Tanida
*Graduate school of Information Science and Technology, Osaka University, Japan*
*Corresponding author: k-yamanouchi@ist.osaka-u.ac.jp*

**Keywords:** Image processing, Scattering, Three-dimensional image processing

## Introduction

Imaging through scattering media is an important technique in various fields including bioimaging. In recent years, optical and computational approaches have developed the field of scattering imaging. However, while many of these methods focus on the two-dimensional shape of the object, achieving three-dimensional (3D) imaging continues to be a challenging task. A digital twin, which is a digital model constructed by data assimilation, emulates a complicated shape and a behavior of a physical object in virtual space. The construction of the digital twin and its interaction with a physical process enable the imaging of complex objects which would be difficult to observe in real space. We aim to achieve accurate 3D imaging through scattering media by using the digital twin. In this study, we attempt to construct a 3D digital twin based on Gaussian Splatting [1]. Gaussian Splatting is a method for representing 3D scenes using ellipsoids with opacities following a 3D Gaussian distribution. By introducing a scattering or de-scattering process into the native algorithm, which is proposed in Ref. [1], an object behind a scattering media can be reconstructed. We investigated a 3D model for a blurred object constructed by the proposed method.

## Method

Figure 1 shows a procedure of the proposed Gaussian Splatting with scattering process. A set of images captured from multiple viewpoints is input to Structure-from-Motion (SfM) [2], which produces a point cloud and estimates a set of camera poses, which are positions and orientations of cameras. The initial point cloud is converted to a set of 3D Gaussians with opacities following a Gaussian distribution by adding three parameters: (a) 3D covariance matrix Σ, (b) opacity $\alpha$, and (c) spherical harmonic coefficient $c$ which represents the color. For rendering, the 3D covariance matrix is transformed to a 2D covariance matrix $\Sigma^{2D}$ in the coordinates determined by the camera poses estimated by SfM. Each pixel value in rendered images is formulated as the alpha-blending of $N$ ordered points that overlap the pixel: $C_{\mathrm{pix}} = \sum_i^N c_i \alpha_i^{2D} \prod_j^{i-1}(1-\alpha_j^{2D})$, where $\alpha_i^{2D}$ represents the $i$-th Gaussian's opacity weighted by the 2D Gaussian covariance $\Sigma^{2D}$. In this study, the scattering process produces scattering images ($I_{\mathrm{scat}}$) from the rendered images ($I_{\mathrm{GS}}$) with the pixel value $C_{\mathrm{pix}}$ as follows:

$$I_{\mathrm{scat}} = \mathrm{PSF} * I_{\mathrm{GS}}, \tag{1}$$

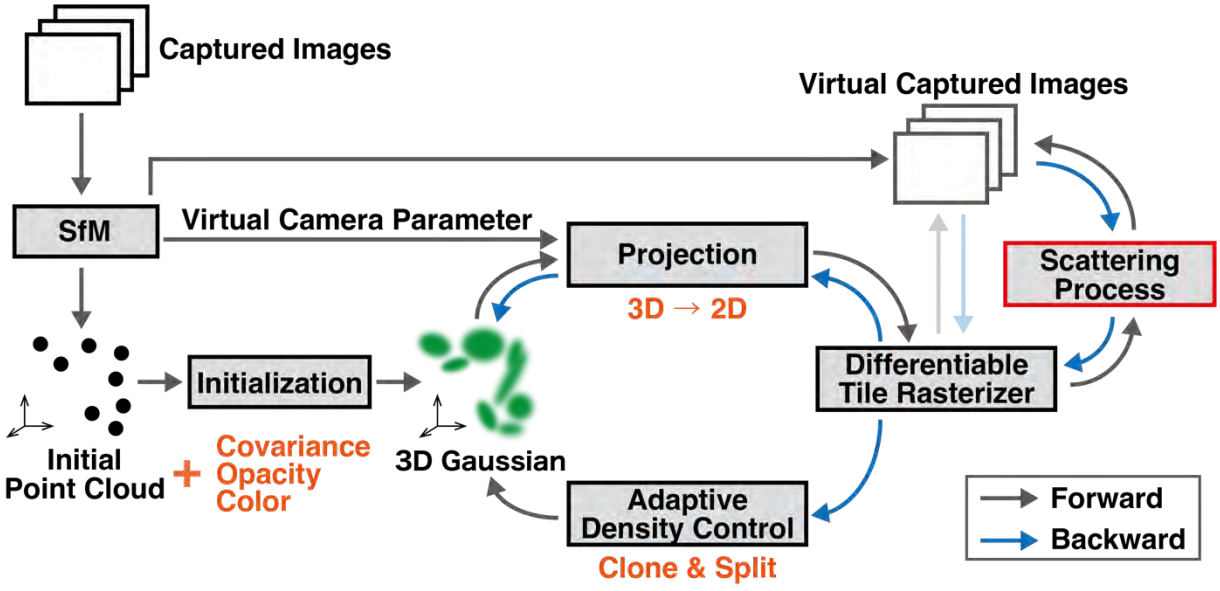


Fig. 1 A procedure of the proposed algorithm with scattering process.

where $*$ denotes the convolution and PSF is a point spread function. Image degradation such as blurring and scattering is modeled by the convolution with a PSF [3]. By introducing this process, the effects of scattering cam be removed. The 3D Gaussian parameters (position, covariance, opacity, color) are optimized by stochastic gradient descent techniques using a loss function based on the L1 norm and the D-SSIM term with the captured images and scattering images. In addition, the number of Gaussians and their density over unit volume is controlled adaptively by cloning and splitting it in two. A de-scattered 3D models can be constructed by iterating this procedure.

## Experiment

To verify the de-scattering capability of the proposed method, a set of blurred images was input to the native and proposed algorithm. As the blurred images, we used a set of images created by convolving a PSF on the images of the target object captured from multiple viewpoints. The PSF was represented by a Gaussian distribution with standard deviation of 5 pixels, and the same PSF was used in equation (1). Figures 2(a)-(c) show the image of the object from a viewpoint, and the reconstructed images by native and proposed algorithm. While native Gaussian Splatting remained a blurred image, the proposed method reconstructed the object without blur. To evaluate the contrast, the width of the white line on the object was measured along the blue horizontal line in the enlarged images. Figure 2(d) shows the widths in each image from all viewpoints. The concordance ratio between the widths of the captured and reconstructed images is 26.3% for the proposed method, compared to 3.95% for the native method. We demonstrated that the proposed method could construct a 3D model with high contrast.

## Conclusion

This study shows that 3D object can be reconstructed from the blurred images by introducing the convolution and deconvolution of the PSF. Future work includes the construction of 3D models for objects behind the actual scattering media.

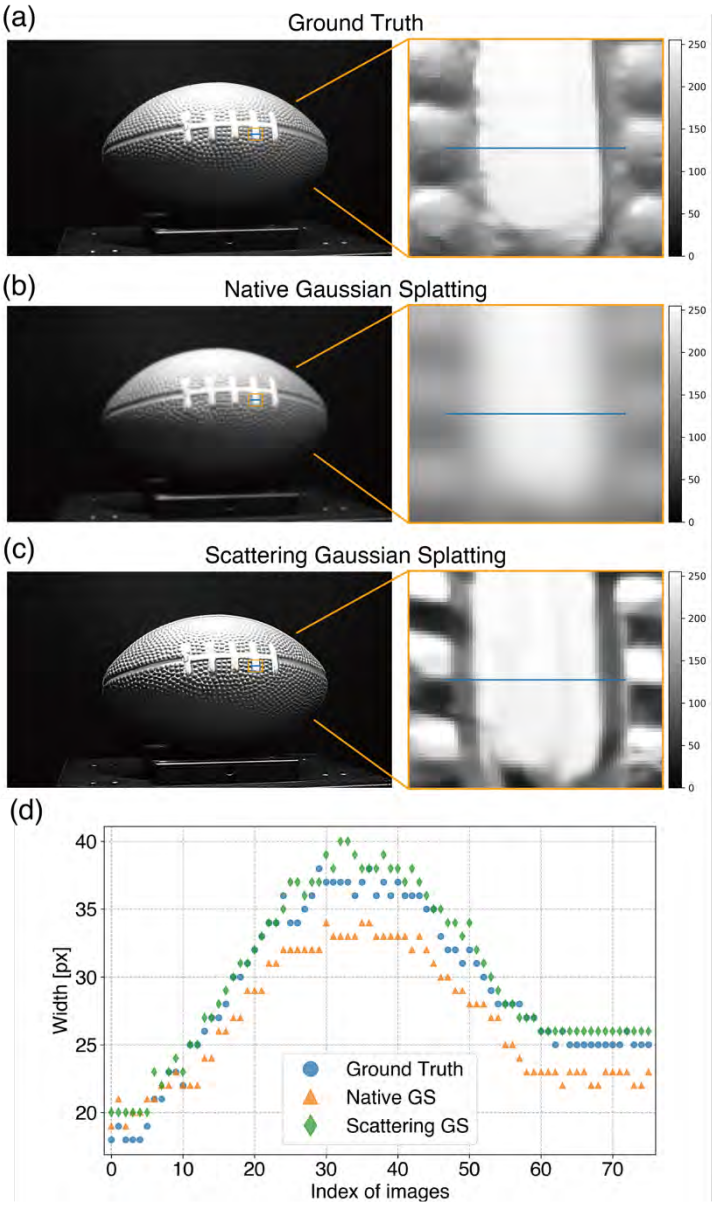


Fig. 2 Reconstruction results. A captured image from a viewpoint (a) and reconstructed images by native (b) and scattering Gaussian Splatting (c), and partial enlarged images of them. (d) The distribution of widths of the white line on the object in the images from all viewpoints.


## Acknowledge

This work was supported by JST KAKENHI Grant Number JP20H05890.


## References


1. B. Kerbl, G. Kopanas, T. Leimkühler, and G. Drettakis, *ACM Transactions on Graphics* **4**(42) (2023).
2. J.L. Schönberger, J.M Frahm, Proceedings of the IEEE conference on computer vision and pattern recognition, 4104-4113 (2016)
3. J.W. Goodman, “Introduction to Fourier Optics” (McGraw-Hill, 1996)

# Spatial and temporal stabilization in holographic beam shaping for industrial use

Yoshio Hayasaki and Satoshi Hasegawa
*Center for Optical Research and Education (CORE), Utsunomiya University*
*Corresponding author: hayasaki@cc.utsunomiya-u.ac.jp*

**Keywords:** Holography, material laser processing, spatial light modulator, feedback control, adaptive optics, Fourier optics, aberration compensation, femtosecond laser

## 1. Introduction

Holographic beam shaping achieved with the reproducible capability of a spatial light modulator (SLM) displaying a computer-generated hologram (CGH) is very useful in a variety of applications, especially for material laser processing [1, 2]. Due to the high throughput and high light use efficiency of holographic reconstruction, it has been used in many kinds of research, such as optical tweezers [3, 4], laser processing [5, 6], micropatterning [7,8], and volumetric display [9]. Although they provide good performance in applications, beam shaping accuracy is reduced by static and dynamic imperfections in optical systems. To compensate for the static imperfections, an in-system optimization method that optimizes the CGH using the Fourier space intensity observation in the optical system, called an in-system optimization, was developed [10]. To compensate for dynamic imperfections, so that the optical system can perform optimization during laser processing, the method called in-process optimization has been demonstrated for the compensation of 2D optical reconstructions [11].

In this paper, we demonstrate the spatial and temporal optimization of optical reconstruction in an optical system using the in-system optimization of the CGH.

## 2. Experimental setup

Figure 1 shows the experimental setup of the holographic laser processing machine. The light source was a second-harmonic wave generated by a laser diode-pumped Yb:KGW femtosecond laser with a maximum power of 10 W, center wavelength of 1030 nm, repetition frequency of 10 kHz, and minimum pulse duration of ~155 fs. The laser pulse was collimated to a diameter of 8 mm by a 2× beam expander. The pulse was diffracted by a CGH displayed on the LCOS-SLM. The resulting spatially shaped optical pattern through a 50× microscope objective with a numerical aperture (NA) of 0.55 mounted on an axially moved piezo stage was made incident on a sample fixed on a linear stage. A cooled CCD imager was used to observe the reconstructed beam. A CMOS imager, a white LED, a lens, a dichroic mirror (DM), and a green cut filter (GCF) were used to monitor laser processing.

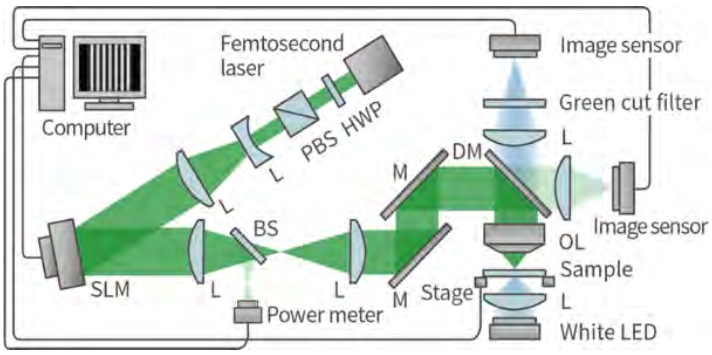


Fig. 1 Holographic femtosecond laser processing machine.

## 3. Experimental results

Figure 2 shows the beam pointing of the focused beam in the lateral direction before and after compensation. The beam diameter on the image sensor position on the Fourier plane was 50 μm. The frame rate of the image sensor was 100 frames per second (fps). The beam-pointing variation of ±2.6 μm standard deviation was improved to that of ±0.3 μm standard deviation using the compensation. It was 0.6% of the beam diameter, and 0.5μrad in terms of angle.

Figure 3 shows an example of holographic laser processing. The 120 parallel beams were optimized to a uniformity of 98%. The sample was a thin glass. The through holes were fabricated by a single shot. The

pulse repetition rate was 10 kHz. The total pulse energy was 5.57μJ. The stage speed was 94 mm/s. The throughput of the drilling reached 1.2 M/s, which was beyond the maximum laser repetition of 1 MHz. This performance overcame laser processing with beam scanning.

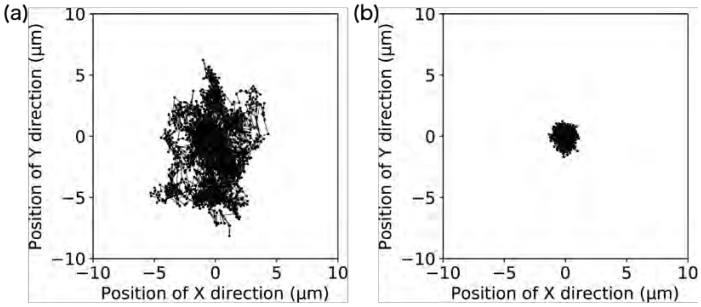


Fig. 2 Beam pointing (a) before and (b) after the compensation.

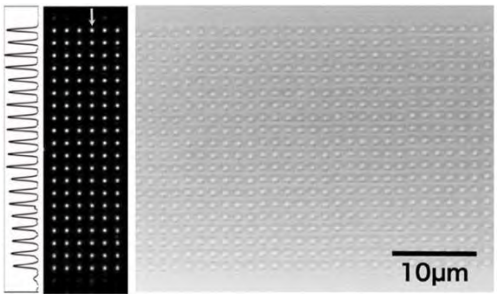


Fig. 3 120 parallel drilling of thin glass.

## 4. Conclusion

We demonstrated the spatial and temporal stabilization of CGH reconstruction in an optical system. The in-system optimization method compensated for the imperfections of the system automatically and performed high-quality beam shaping. The parallel beams enabled the fabrication of high-consistency micro-holes inside the glass at different layers. It is good evidence that high-flexibility, high-quality, and high-efficiency 3D processing can be realized, and this method will have broad application expectations in the future.

**Acknowledgments**

This work was supported by the Council for Science, Technology, and Innovation (CSTI), Cross-ministerial Strategic Innovation Promotion Program (SIP), "Photonics and Quantum Technology for Society 5.0" (Funding agency: QST).

**References**

[1] Y. Hayasaki, T. Sugimoto, A. Takita, and N. Nishida, "Variable holographic femtosecond laser processing by use of a spatial light modulator," Appl. Phys. Lett. **87**, 031101 (2005).
[2] N. Sanner, N. Huot, E. Audouard, C. Larat, J. P. Huignard, and B. Loiseaux, "Programmable focal spot shaping of amplified femtosecond laser pulses," Opt. Lett. **30**, 1479-1481 (2005).
[3] E. R. Dufresne and D. G. Grier, "Optical tweezers arrays and optical substrates created with diffractive optics," Rev. Sci. Instrum. **69**, 1974-1977 (1998).
[4] Y. Hayasaki, M. Itoh, T. Yatagai, and N. Nishida, "Nonmechanical optical manipulation of microparticle using spatial light modulator," Opt. Rev. **6**, 24-27 (1999).
[5] M. Yamaji, H. Kawashima, J. Suzuki, and S. Tanaka, "Three-dimensional micromachining inside a transparent material by single pulse femtosecond laser through a hologram," Appl. Phys. Lett. **93**, 041116 (2008).
[6] M. Sakakura, T. Sawano, Y. Shimotsuma, K. Miura and K. Hirao, "Fabrication of three-dimensional 1 × 4 splitter waveguides inside a glass substrate with spatially phase modulated laser beam," Opt. Express **18**, 12136-12143 (2010).
[7] L. Kelemen, S. Valkai, and P. Ormos, "Parallel photopolymerization with complex light patterns generated by diffractive optical elements," Opt. Express **15**, 14488-14497 (2007).
[8] H. Takahashi, S. Hasegawa, A. Takita, Y. Hayasaki, "Sparse-exposure technique in holographic two-photon polymerization," Opt. Express **16**, 16592-16599 (2008).
[9] K. Kumagai, D. Suzuki, S. Hasegawa, and Y. Hayasaki, "Volumetric display with holographic parallel optical access and multilayer fluorescent screen," Opti. Lett. **40**, 3356-3359 (2015).
[10] S. Hasegawa and Y. Hayasaki, "Adaptive optimization of a hologram in holographic femtosecond laser processing system," Opt. Lett. **34**, 22-24 (2009).
[11] H. Zhang, S. Hasegawa, H. Takahashi, H. Toyoda, and Y. Hayasaki, "In-system optimization of a hologram for high-stability parallel laser processing," Opt. Lett. **45**, 3344-3347 (2020).

## *Session 6: Photonics Applications*

**Wednesday Jan 8, 2025**

13:40-14:00 Yukitoshi Otani: Seasonal sunlight interaction using angularly selective microstructured surfaces

14:00-14:20 Kenji Harada: Phenomenon of coloration of bubbles under thin ice observed in Lake Kussharo during severe winter

14:20-14:40 Shuji Taue: AC Magnetic field imaging with optically pumped magnetometer and digital micromirror device

# Seasonal sunlight interaction using angularly selective microstructured surfaces

Kazutaka Isoda[1], Kohki Nagata[1], Daisuke Ogawa[1], Mizue Ebisawa[1], Nathan Hagen[2], *Yukitoshi Otani[2]

[1] *Tokyo Metropolitan Industrial Research Institute, Japan*
[2] *CORE, Utsunomiya University, Japan*

*Corresponding author: otani@cc.utsunomiya-u.ac.jp*

**Keywords:** Seasonal sunlight interaction using angularly selective microstructured surfaces

The global energy consumption in 2015 has reached to double comparing with 1971. We can estimate 30% of this energy has been used for controlling the environment within buildings [1] and 40-50% of the energy consumed in the USA is for the heating, ventilation and air conditioning (HVAC) of buildings [2]. It has already proposed a "cool roof" for reducing the energy in summer [3] and a high absorption paint in winter [4]. Reducing energy consumption in winter requires a low reflectivity (absorptive) surface. A single surface which can perform both tasks can provide energy benefits in both seasons. Akbari. Proposed a heterogeneous directional reflective materials (DRM) to realize a surface with seasonally varying reflectivity. [5] This DRM surface has a periodic triangular structure such that all faces pointing towards the sun have high reflectivity and faces pointing away from the sun have low reflectivity. This seasonal difference in reflectivity is small; a surface with a larger change can provide improved energy efficiency.

In this paper, we propose angularly selective surfaces that adjust their reflectivity by the sun position allow beneficial effects in both summer solstice 12º and winter solstice 58º at the lat. 38 º N as shown in Fig.1. High-reflectivity exterior surfaces save energy spent on ventilation and cooling during summer., but cost energy on heating in winter. we propose the question of whether a periodic microstructured surface which provide the sharper angular dependence needed to achieve this. We also confirm an ideal angular reflectivity profile and show how to make use of this to quantitatively evaluate the effectiveness of any given surface.

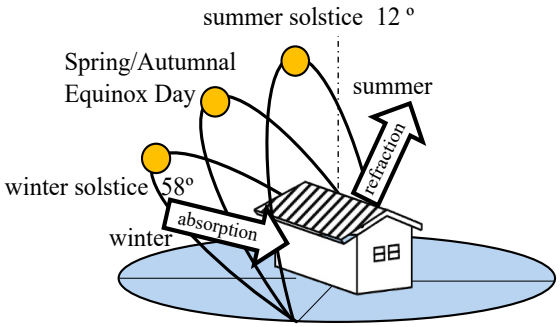


Fig.1 A view of the sun position

Figure 2 shows a designed a periodical structure by numerical simulations. It works for 80% at 10º and 50% at 70º. The minimum reflectivity is found at θ = 50º for the manufactured structure while θ = 70º for the original design. A surface photograph and a SEM picture are shown in Fig.2(a) and (b). It was made by a semiconductor process and its shape shows h = 0.28μm, w = 0.44μm, A = 1.25μm based on h = 0.40μm, w = 0.40μm, A = 1.20μm as design.

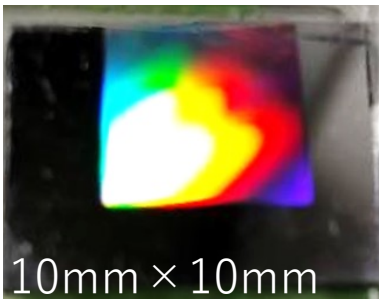


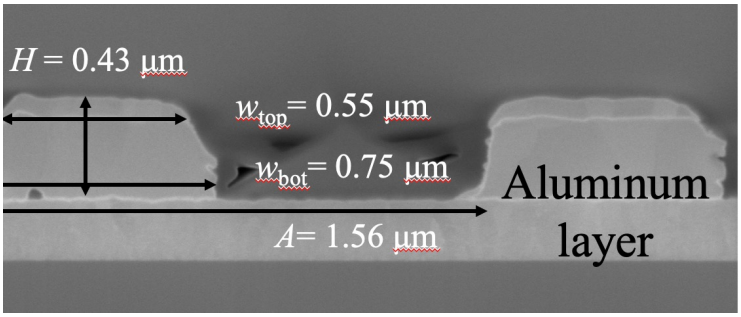


(a) Structured surface (2) Cross section of SEM

Fig.2 Fabricated result of angularly selective microstructured surfaces

Figure 3 shows a reflectivity of a manufactured structure. Numerical simulations for the original design A/λ = 2, h/w = 0.5 are set as 80% at 10, and 50% at 70º. The minimum measured reflectivity is indicated at θ = 50º as comparing with θ = 70º for the original design. The manufactured structure also shows 10% less reflectivity for the lower incident angle below 40º. The red solid line represents a numerical result used by the SEM-based cross-sectional shape, and the blue line shows the original design.

Figure 4 shows experimental result of change of temperature and absorption along the incident angle by the solar simulator which can make parallel beam as same as spectral "AM1.5G"as the Sun. The difference of temperature ΔT indicates 1.2ºC at the maximum at the 40º~50º. According to the result, temperature difference between winter and summer shows 0.3ºC. A planar microstructured surface can produce such an angularly selective behavior and estimate its energy efficiency under direct solar irradiance at 35° N. Results show that such an ideal angularly selective surface has the potential to improve efficiency by up to 43.2% compared to a conventional concrete surface.

In conclusion, we start by modeling the angular reflectivity distribution around the sun position trajectories distributed over the course of a year. We analyzed the structure by the rigorous coupled wave analysis (RCWA) to estimate the amount of reflected and absorbed sunlight experienced by one-dimensional periodic aluminum structure. We confirmed temperature change and power change depending on the incident angle

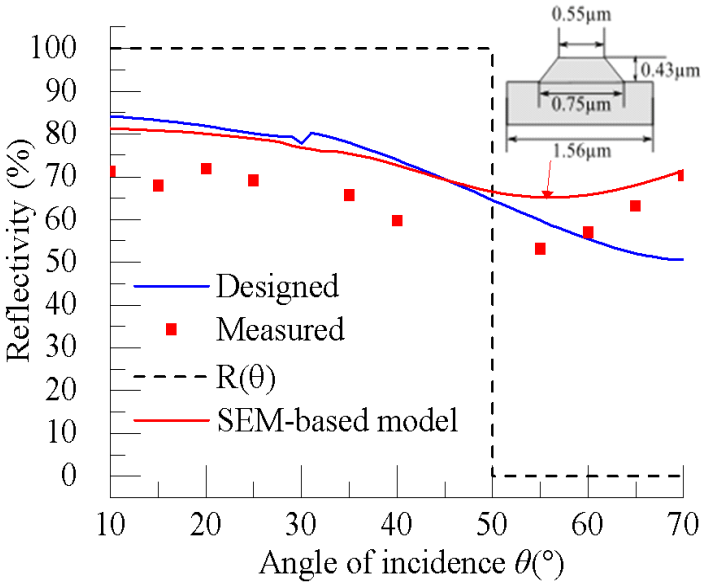


Fig.3 Reflectivity profile of the structure

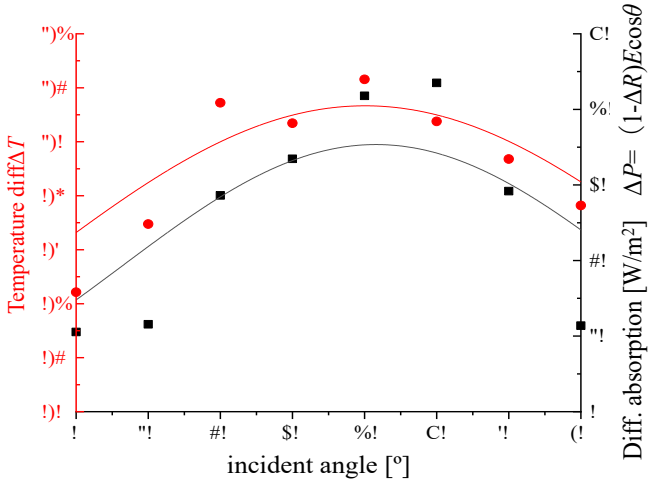


Fig.4 Experimental result of temperature change and change of absorption along the incident angle

**References**


1. S. B. Sadineni, S. Madala, and R. F. Boehm, *Energy Rev*. 15, 3617–3631 (2011).
2. L. Pérez-Lombard, J. Ortiz, and C. Pout, *Energy Build*. 40, 394–398 (2008).
3. M. Santamouris, *Sol. Energy* 103, 682–703 (2014).
4. A. Synnefa, M. Santamouris, and H. Akbari, *Energy Build*. 39, 1167–1174 (2007).
5. H. Akbari and A. G. Touchaei, *Sol. Energy Mater. Sol. Cells* 124, 192–210 (2014).

# Phenomenon of coloration of bubbles under thin ice observed in Lake Kussharo during severe winter

Kenji Harada, Tamaki Miwa, and Daisuke Sakai
*Kitami Institute of Technology,*
*Corresponding author: kharada@mail.kitami-it.ac.jp*

**Keywords:** polarizer, birefringent material, coloring phenomenon

## 1. Introduction

In Hokkaido, Japan, there are natural optical phenomena such as sun pillar, diamond dust, jewelry ice and frost flowers that can only be observed under certain conditions during the severe winter season. Recently, coloration of bubbles under thin ice was reported in Lake Kussharo, Japan, during severe winter. This natural optical phenomenon was named “jewelry bubble”. Temperature and wind speed have a significant effect on the observation of jewelry bubble. This phenomenon can only be observed through a polarizer. It is thought that polarization color is observed due to the birefringence of ice. We present a case study of observations of jewelry bubble. The phenomenon of bubble coloration was calculated using Mueller matrix.

## 2. Polarization color created by nature

At Lake Kussharo during severe winter, coloration of bubbles under thin ice can be observed. Figure 1(a)(b) show photographs of the coloration phenomenon taken in January 2023 with or withoput polarizer. This coloration phenomenon can only be observed through a polarizer as shown in Fig. 1(b). We assume this phenomenon is observed by reflecting off a bubble formed between ice and water. Figure 2 shows a light reflection model. Lake Kussharo is a caldera lake, and gas springs from the bottom of the lake. The hot spring gas collects between ice and water. The thickness of the ice changes partially because some ice melts due to the heat of the hot spring gas. When the polarized reflected light passes through the ice, the polarization state changes due to the birefringence of the ice.

(a) Without polarizer (b) With polarizer

Fig. 1. Jewelry bubble at Lake Kussharo.

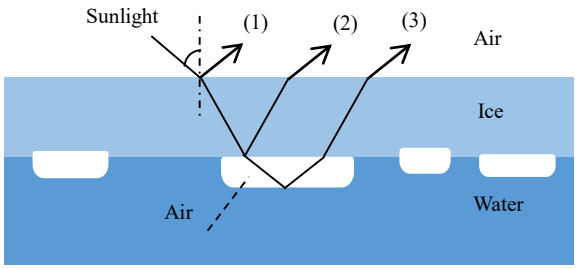


Fig. 2. Model of light reflection.

## 3. Calculation of polarization color

In this section, we discuss the calculation of polarization color using the Mueller matrix. The Jones matrix used in the past could only handle perfectly polarized light. However, since jewelry bubble is a phenomenon observed in the field and the light source is natural light, partial polarization and unpolarized light should also be considered. Therefore, in this section, we performed theoretical calculations using the Muller matrix with natural light as the light source. Equation (1) is an expression for the polarization state of the light (3) shown in Fig.2, when the incident light is natural light using the Muller matrix, where $R_s$ and $R_p$ represent the reflectance of the s- polarization and p-polarization components, respectively. Here, $\theta$ represents the rotation angle, and $\varphi$ represents the phase change in the ice. Mueller matrix at transmission is omitted in this equation.

$$E(\lambda) = \begin{bmatrix} 1 & 1 & 0 & 0 \\ 1 & 1 & 0 & 0 \\ 0 & 0 & 0 & 0 \\ 0 & 0 & 0 & 0 \end{bmatrix} \begin{bmatrix} 1 & 0 & 0 & 0 \\ 0 & \cos(-2\theta) & \sin(-2\theta) & 0 \\ 0 & -\sin(-2\theta) & \cos(-2\theta) & 0 \\ 0 & 0 & 0 & 1 \end{bmatrix} \begin{bmatrix} 1 & 0 & 0 & 0 \\ 0 & 1 & 0 & 0 \\ 0 & 0 & \cos\varphi & -\sin\varphi \\ 0 & 0 & \sin\varphi & \cos\varphi \end{bmatrix} \begin{bmatrix} 1 & 0 & 0 & 0 \\ 0 & \cos 2\theta & \sin 2\theta & 0 \\ 0 & -\sin 2\theta & \cos 2\theta & 0 \\ 0 & 0 & 0 & 1 \end{bmatrix}$$
$$\begin{bmatrix} 1 & 0 & 0 & 0 \\ 0 & 1 & 0 & 0 \\ 0 & 0 & \cos\pi & \sin\pi \\ 0 & 0 & -\sin\pi & \cos\pi \end{bmatrix} \begin{bmatrix} \frac{(R_s+R_p)}{2} & \frac{(R_s-R_p)}{2} & 0 & 0 \\ \frac{(R_s-R_p)}{2} & \frac{(R_s+R_p)}{2} & 0 & 0 \\ 0 & 0 & \sqrt{R_sR_p} & 0 \\ 0 & 0 & 0 & \sqrt{R_sR_p} \end{bmatrix}$$
$$\begin{bmatrix} 1 & 0 & 0 & 0 \\ 0 & \cos(-2\theta) & \sin(-2\theta) & 0 \\ 0 & -\sin(-2\theta) & \cos(-2\theta) & 0 \\ 0 & 0 & 0 & 1 \end{bmatrix} \begin{bmatrix} 1 & 0 & 0 & 0 \\ 0 & 1 & 0 & 0 \\ 0 & 0 & \cos\varphi & -\sin\varphi \\ 0 & 0 & \sin\varphi & \cos\varphi \end{bmatrix} \begin{bmatrix} 1 & 0 & 0 & 0 \\ 0 & \cos 2\theta & \sin 2\theta & 0 \\ 0 & -\sin 2\theta & \cos 2\theta & 0 \\ 0 & 0 & 0 & 1 \end{bmatrix} \begin{bmatrix} 1 \\ 0 \\ 0 \\ 0 \end{bmatrix} \quad (1)$$

Figure 3 is the result of a theoretical calculation using equation (1) for the polarization color observed when the light source is the CIE standard light source D65 at Brewster's angle. In this simulation, the ice crystal axis was calculated as parallel to the lake surface. The horizontal axis represents the angle of polarizer. The polarization color varies depending on the thickness of the ice and the orientation of the crystal axis.

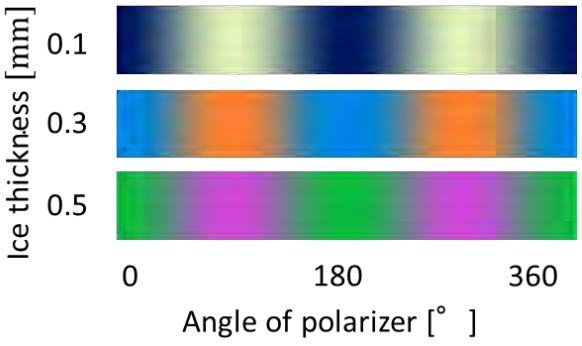


Fig. 3. Simulation results of jewelry bubble coloration.

## 4. Conclusions

The coloration mechanism of jewelry bubbles observed in Lake Kussharo was investigated. Using the Mueller matrix, we calculated the coloration of the ice. The use of Muller matrices enables calculations with partial polarization, and simulations of polarization color in reflected and natural light can be computed. Temperature and wind speed have a significant effect on the observation of jewelry bubble. In the future, we hope to be able to predict when jewelry bubbles can be observed based on weather conditions as a tourism resource.

# AC Magnetic field imaging with optically pumped magnetometer and digital micromirror device

Shuji Taue
*Kochi University of Technology, Kami city, Kochi, Japan*
*Corresponding author: taue.shuji@kochi-tech.ac.jp*

**Keywords:** optically pumped magnetometer, magnetic field imaging, digital micromirror device

We have developed an AC magnetic field imaging system that uses an optically pumped magnetometer (OPM) and a digital micromirror device (DMD). The system is capable of capturing magnetic field distributions with sub-millimeter spatial resolution without the need for mechanical scanning, allowing for an accurate estimation of the position of the signal source.[1] In addition, we have demonstrated improved noise robustness and high spatial resolution by using single pixel imaging. As an application of this imaging system, we investigated its use for Magnetic particle imaging (MPI). MPI is a minimally invasive technique to track the accumulation of magnetic nanoparticles (MNPs) in tumor and cancerous tissue.[2] An external alternating magnetic field induces a magnetic signal from MNPs injected into the body. Sensors detect the signal field as it exits the body. Analysis of the magnetic signal distribution provides an estimate of the position, size, and concentration of the accumulated MNPs. Detecting MNPs' small signal field is challenging because it is much weaker than the excitation field. Conventional methods use coil probes and take advantage of the nonlinear response of magnetic particles to separate the signal field from the excitation field. Although highly sensitive sensors and strong excitation fields (several milli Tesla) can improve the signal-noise ratio [3], the field strength must meet human exposure guidelines [4]. In this study, we propose and demonstrate a method for separation of excitation and signal magnetic fields for MNPs solutions in compliance with human exposure guidelines as a study towards MPI using OPM.

The signal field from the MNPs induced by the excitation field is produced as a magnetization response in which the magnetic moment in the particle is aligned in the direction of the excitation field. Figure 1 shows an image of the magnetization response from a particle induced by an excitation field, where the alignment of the magnetic moments of the MNPs is caused by two types of magnetic relaxation: Brownian rotation due to the rotation of the particle and Néel rotation due to the rotation of the magnetic moments within the particle.

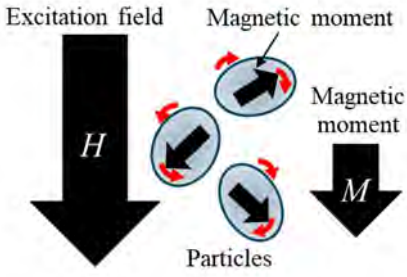


Fig. 1. Magnetization of particles

The magnetization delay caused by the magnetic relaxation of these MNPs can be detected as a phase delay of the signal field relative to the excitation field. The phase-sensitive detection function of the lock-in amplifier (LIA) is used for detection, and the phase shift is adjusted in the LIA so that the detected signal of the excitation field is in phase with the reference signal. By using this function of the LIA and adjusting the phase shift of the detected signal of the excitation magnetic field in the lock-in amplifier so that it is in phase with the reference signal, the signal field with a phase delay can be detected as an out-of-phase signal component which is orthogonal to the phase of the reference signal. This makes it possible to separate the excitation magnetic field from the signal magnetic field.

As shown in Fig. 2, a 5 mm inner diameter plastic container was placed directly over the area on the sensor head. The container contained 150 µl of an aqueous solution of MNPs. The excitation field, set at 200 kHz and 640 nT, was applied from a coil positioned 150 mm above the sensor head (not shown in Fig. 2). The amplitude of the light passing through the sensor head is modulated by the excitation field and the signal response of the MNPs. The response exhibits a phase delay caused by magnetic relaxation of the MNPs.

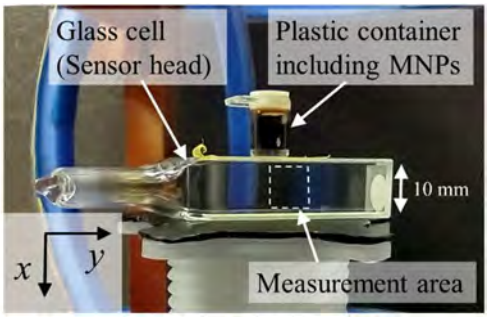


Fig. 2. Sensor head and the plastic container

Figure 3(a) depicts the magnetic field distribution obtained as the in-phase component by scanning the mirrors of the DMD. The circular distribution with a pronounced center is attributed to the influence of the irradiated light's intensity. Figure 3(b) depicts the signal field distribution from MNPs acquired as the out-of-phase component. A reduction in signal intensity is evident in the upper center region where MNPs are present, accompanied by the emergence of a local magnetic field distribution. This is attributed to the signal field generated by the MNPs.

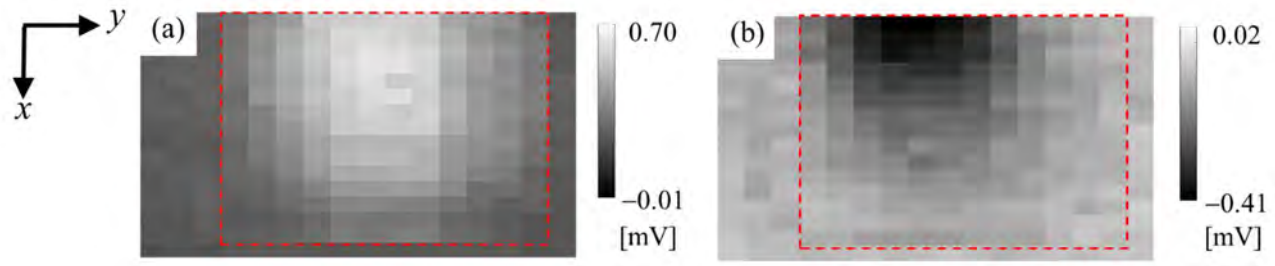


Fig. 3. Obtained image of (a) in-phase and (b) out-of-phase components with 16 × 16 pixels including the measurement area of 10 ×10 mm indicated with red dashed line.

In utilizing this distribution image to estimate the position of the signal source, the attenuation of the magnetic field signal in the x-axis direction represents a particularly crucial element for enhancing the precision of the estimation. Consequently, the acquisition of distribution images with enhanced resolution and reduced noise is a significant challenge. However, the current imaging method based on mirror scanning presents challenges, including an increase in measurement time and a deterioration of the signal-to-noise ratio due to a decrease in the light-receiving intensity. To address these limitations, single-pixel measurement using pattern display instead of mirror scanning has the potential to offer a solution. Additionally, we are exploring the possibility of reducing the measurement time by developing a display pattern and investigating real-time magnetic field distribution measurement and signal source estimation.

**Acknowledgement**

This work is supported by JSPS KAKENHI 23K20939, 24H00837.

**References**

1. S. Taue and Y. Toyota, *Optical Review* **27**, 258–263(2020).
2. B. Gleich and J. Weizenecker, *Nature* **435**, 1214–1217 (2005).
3. T. Knopp and T.M. Buzug, *Magnetic Particle Imaging: an introduction to imaging principles and scanner instrumentation*, (Springer-Verlag, Berlin Heidelberg, 2012).
4. International Commission on Non-Ionizing Radiation Protection (ICNIRP), *Health Physics* **118**, 483–524(2020).

## *Poster presentations*

Ilpo Niskanen: Complex refractive index shift from liquid to solid in the drying process
Kai-Erik Peiponen: Ultra-high-definition imaging in the detection of microplastics in water flow
Soma Tobinaga: Computational considerations of adaptive single-pixel imaging for magnetic particle imaging with optically pumped magnetometer

# Complex refractive index shift from liquid to solid in the drying process

Ilpo Niskanen[1*], Janne Lauri[2], Satu Ojala[3], Tanja Kolli[1], Masayuki Yokota[4], Rauno Heikkilä[1],Tapio Fabritius[2]

[1] *Faculty of Technology, Civil Engineering Research, University of Oulu, FI-90014 Oulu, Finland*

[2] *Faculty of Information Technology and Electrical Engineering, Optoelectronics and Measurement Techniques Research Unit, University of Oulu, P.O. Box 4300, FI-90014, Oulu, Finland*

[3] *Faculty of Technology, Environmental and Chemical Engineering, University of Oulu, P.O. Box 7300, FI-90014 Oulu, Finland*

[4] *Department of Mechanical, Electrical and Electronic Eng., Faculty of Science and Engineering, Shimane University, 1060 Nishikawatsu-cho, Matsue-shi, Shimane 690-8504, Japan*

**Corresponding author: ilpo.niskanen@oulu.fi*

**Keywords:** Complex refractive index; drying process; varnishes; adhesives

Coating surfaces in industrial products serves multiple purposes, including corrosion protection, waterproofing enhancement, visual improvement, and modification of mechanical properties. The drying process, transitioning from a liquid to a solid state, is a complex phenomenon influenced by various factors such as airflow, temperature, chemical composition, physical dimensions, and humidity [1]. Effective control of drying time is economically significant, impacting overall production efficiency.

The refractive index is a critical material property, as it governs the interaction between photons and matter. A higher refractive index results in greater light bending within the material, leading to a smoother and more flawless surface appearance. Conversely, a lower refractive index is advantageous in applications like glass coatings, where it reduces reflection and enhances light transmission. Beyond light interaction, the refractive index also provides insights into a material's structural and electronic properties, making it essential for understanding material behavior across a wide range of applications [2].

In this study, we used Unica Akva lacquer (Tikkurila), Unica Super 90 lacquer (Tikkurila), Color C46 Clear varnish (GSI Creos), Loctite 60 Sec glue (Loctite), and Loctite Super glue (Loctite). The Unica Akva varnish is composed of a modified acrylate, while Unica Super 90 is a urethane alkyd lacquer. The Color C46 Clear varnish contains methyl isobutyl ketone (30-40%), ethyl acetate (5-10%), butyl acetate (5-10%), ethanol (1-5%), methyl ethyl ketone (1-5%), n-butyl alcohol (1-5%), and diacetone alcohol (1-5%). The Loctite 60 Sec glue is composed of ethyl-2-cyanoacrylate (60-100%) and glyceryl ester (10-30%), while Loctite Super glue consists of ethyl 2-cyanoacrylate and methyl methacrylate.

The refractive indices of the films were measured at a controlled environment (21°C and 30% relative humidity) at the beginning (0 hours) and end (26 hours) of the test using the Krüss DR6100-T refractometer at 589 nm, with an uncertainty of ±0.0001 refractive index units. Transmittance intensity of the samples was assessed using a standard 10 mm plastic cuvette for transmission spectra (350-700 nm) of both liquids and solids, at a consistent room temperature of 21°C and 14% relative humidity, using a spectrophotometer. Deionized water was used as the baseline.

The refractive index of Unica Akva lacquer, Unica Super 90 lacquer, Color C46 Clear varnish, Loctite 60 Sec glue, and Loctite Super glue increased from 1.382 to 1.484, 1.473 to 1.519, 1.438 to 1.482, 1.443 to 1.452, and 1.444 to 1.446, respectively. This increase in refractive index positively affects the material's reflective properties. The refractive index is intrinsically linked to a material's chemical composition, with different functional groups and bonding types—whether ionic or covalent—significantly influencing it [3]. Even a 0.1 unit change in refractive index can alter a material's light-refracting capability, impacting its transparency, reflectivity, and light transmission efficiency. Such changes underscore the importance of precise refractive index adjustments to optimize material performance and achieve desired outcomes in specific applications.

In conclusion, utilizing refractive index data significantly aids in optimizing the drying process and provides valuable insights into the optical properties of materials. This understanding is essential for predicting material

behavior during drying and for its impact on the final product's performance, ensuring both functional efficacy and aesthetic quality.

**References**


1. I. Lourenço, G.R.C. Possetti, M. Muller, J.L. Fabris, *Sensors* **10** 4761-4776 (2010).
2. I. Niskanen, J. Lauri, J. Räty, R. Heikkilä, H. Liimatainen, T. Hashimoto, T. Fabritius, M. Yokota, *Prog. Org. Coat.* **135** 105299 (2019).
3. H.W. Jaffe, Crystal Chemistry and Refractivity, second ed., Dover Publications, Mineola, New York, 1996

# Ultra-high-definition imaging in the detection of microplastics in water flow

Kai-Erik Peiponen,Benjamin Asamoah, Ana Gebejes and Matthieu Roussey
*Department of Physics and Mathematics, University of Eastern Finland (Joensuu Campus)*
*Corresponding author: kai.peiponen@uef.fi*

**Keywords:** ultra-high-definition imaging, microplastics, water

There is a common consensus that microplastics (MP) are ubiquitous and constitute a toxic threat both to flora and fauna as MPs are present in the atmosphere, natural water bodies, wastewater, and soils. Hence, nowadays there is the term "plastisphere", describing the ecosystem depending on plastic debris. Due to this emerging problem and the need for standardization, in 2023, the international standard ISO24187: Principles for microplastic analysis was published. This standard is based on sample collection, pre-treatment processes, and typically time-consuming measurements, such as micro-FTIR and micro-Raman, in laboratory conditions. However, there is a demand to detect MPs in field conditions directly from natural water bodies, wastewater etc. Unfortunately, the protocols provided by the international standard are not applicable in their present form for such purposes.

We propose the exploitation of an ultra-high-definition (UHD) imaging method to monitor both the physical and optical properties of MPs in tap water [1] and also in wastewater samples [2]. Here, we deal with the UHD-aided detection of the morphology of MPs and their motion in water flowing through a cuvette using a commercial Valmet FS5 device.

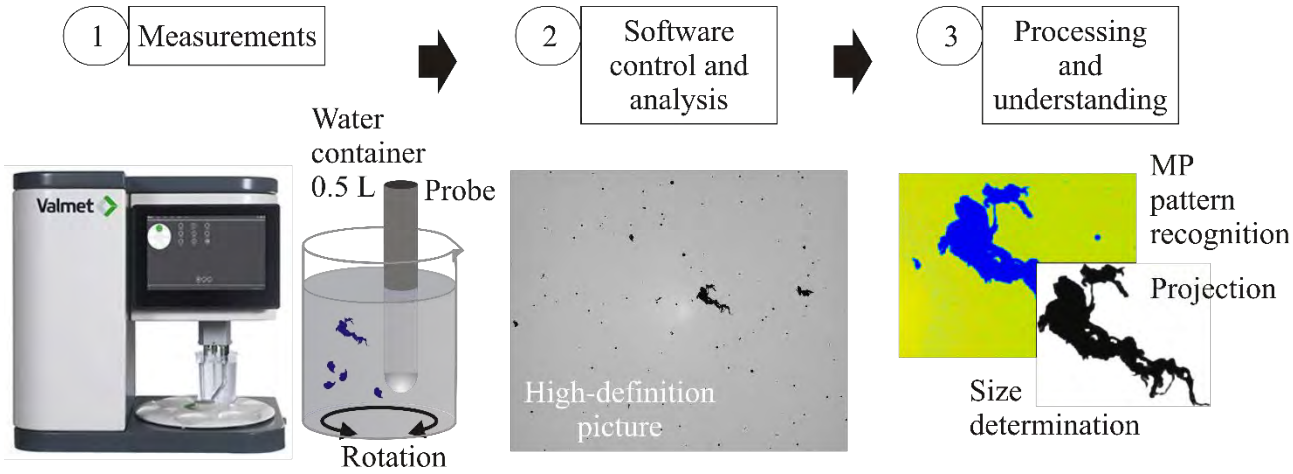


Fig. 1: Detection of MPs in laminar water flow in a cuvette. Imaged irregular-shaped LDPE MPs and circular-shaped air bubbles in the middle image (2).

Fig. 1 illustrates the process of UHD imaging of MPs in a water sample. One obtains information on the presence of MPs, their sizes, shapes, velocity and multibody interactions between organic-, inorganic particles, and air bubbles in water samples from the UHD image.
Fig. 2 shows an example of a semi-transparent unplasticized PVC MP. This UPVC MP is rotating in the laminar water flow. The rotation reveals different “faces” of the irregular-shaped particle.

The obtained results suggest that UHD imaging is a plausible method for the detection of MPs in aquatic environments, requiring no sample preparation. Identification of the presence of plastics among other inorganic or organic particles is based on light-intensity bitmap information obtained from the device. While this method provides a rapid detection of single-type MPs flowing in water, the sensor certainly requires further development and modifications for practical use in field

measurement conditions of MP detection, which is the goal of future studies. Modifications may include identification of MPs using hyperspectral imaging of MPs in water [3]

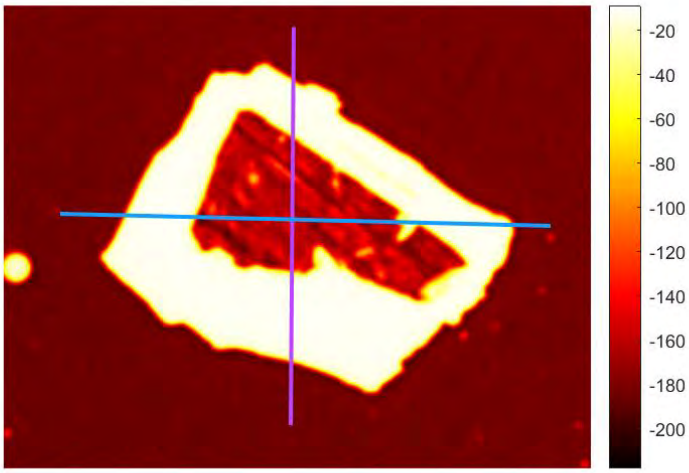


Fig. 2. Irregular-shaped UPVC MP. Surface texture due to the finishing process of the plastic appears as parallel finishing marks. The colors present light-intensity map-related parameters. On the left side, the bright circular object is an air bubble.

**References**

1. K.-E. Peiponen, B. Kanyathare, B. Hrovat, N. Papamatthaiakis, J. Hattuniemi, B. Asamoah, A. Haapala, A. Koistinen, M. Roussey, J. Eur. Opt. Society-Rapid Publ., 19, 14, 2023.
2. B. Hrovat, E. Uurasjärvi, M. Viitala, A. Franco del Pino, M. Mänttäri, N. Papamatthaiakis, A. Haapala, K.-E. Peiponen, M. Roussey, A. Koistinen, Sci. Tot. Env., 925, 171821, 2024.
3. A. Gebejes, B. Hrovat, D. Semenov, B. Kanyathare, T. Itkonen, M. Keinänen, A. Koistinen, K.-E. Peiponen, M. Roussey, Sci. Tot. Env., 944, 173811.

# Computational considerations of adaptive single-pixel imaging for magnetic particle imaging with optically pumped magnetometer

Soma Tobinaga and Shuji Taue
*Kochi University of Technology, Kami city*
*Corresponding author: taue.shuji@kochi-tech.ac.jp*

**Keywords:** magnetic particle imaging, optically pumped magnetometer, single-pixel imaging

In recent years, medical research has been conducted using magnetic nanoparticles (MNPs) to help diagnose cancer and other diseases. MNPs attract cancer cells by modifying functional molecules on the surface of the particles. Magnetic particle imaging (MPI) is a method of detecting the location of target tissues based on the magnetic field distribution of the magnetic particles.[1] In this method, magnetic signals are generated directly from the magnetic particles by applying an external excitation magnetic field. The position of the particles is detected by solving an inverse problem from the magnetic field distribution images obtained at multiple measurement points. The location detection in depth direction is of importance because the attenuation of the magnetic field with distance must be measured for analysis.

To obtain the magnetic field distributions, we have constructed magnetic field imaging system using an optically pumped magnetometer and a digital mirror array device (DMD).[2] The image acquisition is based on single-pixel imaging (SPI) technique, and sub-mm resolution is possible in exchange for longer measurement time. Previous studies have used compressed sensing (CS) with sparsity to produce images. However, CS works to increase the contrast of the image, and thus has limitations for imaging where gradation is important, such as in magnetic field distribution. In this study, a computational consideration is conducted on SPI technique, which reduces the spatial resolution except for the area close to the skin. We use a two-step pattern with two levels of resolution, which is specialized for magnetic field distribution, for imaging and position estimation, with the aim of speeding up the process by reducing the number of measurements.

Figure 1 shows a numerically computed field distribution from MNPs, which is used as the target image for the reconstruction. Figure 2(a) and (b) show examples of a random pattern (32 × 32 pixels) as the conventional method and a two-step pattern (32 × 16 + 16 × 8 pixels) as the two-step random pattern, respectively. Comparison with the numerically computed magnetic field distribution was performed using the root mean square error (RMSE) for position estimation.

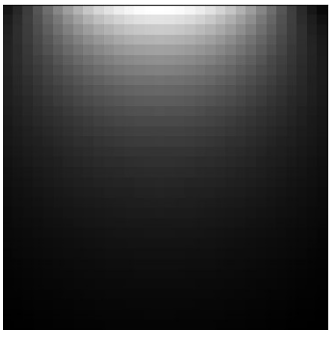

Fig. 1. Target image


Fig. 2 (a) A random pattern and (b) a two-step random pattern

As an example of the results, Figure 3(a) and (b) show the reconstructed images with 62% of the data acquired by the conventional and the two-step pattern, respectively. As shown in Fig. 3(a), noise remains due to the data reduction, whereas in Fig. 3(b), noise is reduced.

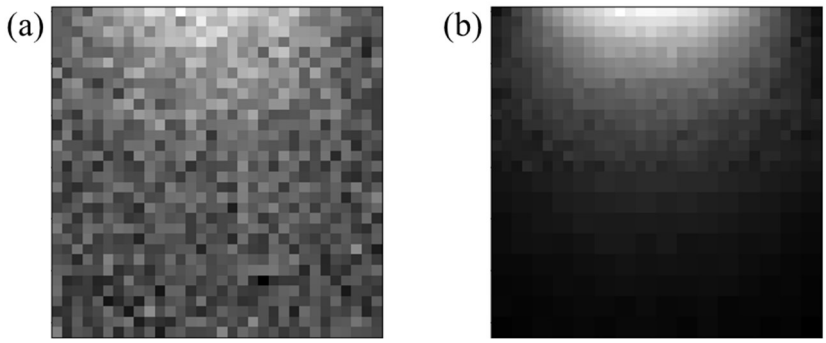


Fig. 3 Reconstructed images with 62% of the data acquired by (a) A random pattern and (b) two-step pattern

Figure 4 shows the results of the position estimation: the RMSE with 62% of the data in the depth direction is significantly different when a two-step pattern is used compared to the conventional method. The RMSE of the two-step pattern (62% of the data) was close to that of the random pattern (100% of the data), indicating that the two-step random pattern reduced the number of measurements and maintained the accuracy of the position estimation.

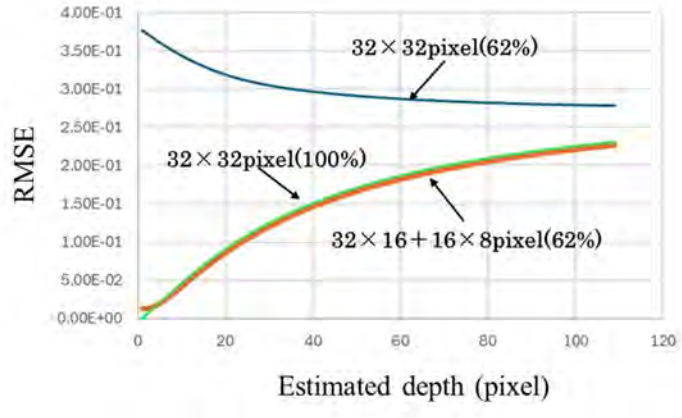


Fig. 4. Position estimation results

In the future, we will consider patterns that can reduce the number of data while maintaining location estimation accuracy.

**Acknowledgement**

This work is supported by JSPS KAKENHI 23K20939, 24H00837.

**References**

1. B. Gleich and J. Weizenecker, *Nature* **435**, 1214–1217 (2005).
2. S. Taue and Y. Toyota, *Optical Review*, **27**, 258–263(2020).